Development and Implementation of Capability Enhancements for Focused Laser Differential Interferometry

A Dissertation Presented for the
Doctor of Philosophy
Degree
The University of Tennessee, Knoxville

Seth Richard Holladay

December 2024

Dedication

To my parents and sister, thank you for your love and support!

Acknowledgements

The support and guidance of a long list of people got me to this point, and I could probably write another whole thesis thanking them. However, to spare any future readers, I will keep it to the barest minimum. Thank you to Dr. Kivanc Ekici, Dr. Jeffrey Reinbolt, and Julie Knoefel for always being there to answer my questions about graduate school and helping me navigate the process. They made the daunting seem possible for me. I would also especially like to thank the members of my committee, Dr. Damiano Bacarella, Dr. David Donovan, and Dr. Trevor Moeller for their knowledge, advice, and patience. Their expertise and passion in their own work are constant sources of inspiration. I am equally appreciative of the many peers and lab alumni that I have had the privilege to get to know and work alongside in the course of my research. Their friendliness, enthusiasm for learning, unique perspectives, and eagerness to help others made it a wonderful environment and enriching experience. I will always remember our fun gatherings for dinner and pumpkin carving, which made everyone feel at home. Of course, none of this would have been possible without my advisor and mentor, Dr. Zhili Zhang, who has always encouraged me to strive to reach my full potential. I have benefitted from his wisdom and support along every step of the path: from undergraduate seminar, to professional topics, senior lab, my time as a master's student, and my time working in his lab group. Finally, I once again thank my family for always being there for me through this long journey.

Abstract

Enhancements to the capabilities of focused laser differential interferometry (FLDI) are developed and validated. These enhancements address shortcomings in existing FLDI systems to allow researchers greater flexibility in applying the technique and analyzing flows with complex features or geometries, like plasma and hypersonic flow. The primary shortcomings that are addressed regard the acquisition of FLDI measurements from large beam arrays, the creation of arrays of arbitrary shape and size, the limited use of FLDI in small-scale applications, and the integration of absorption spectroscopy methods with FLDI. First, a high-speed camera was shown to be a suitable alternative to photodiode arrays for data acquisition from a 2D array of FLDI beams in Mach 1 flow. The power spectral densities (PSD) of each beam were measured and compare favorably with values obtained from a photodiode for the same jet flow. Next, a spatial light modulator (SLM) was integrated into a 1-point FLDI to create a novel spatial light modulated FLDI (SLM-FLDI), and PSD measurements recorded for both an SLM-FLDI and a 1-point FLDI in the same region of a Mach 1.5 jet revealed strong agreement between the detected dominant frequencies. Then, small-scale designs of both 1-point and 2-point FLDI were developed. Each used an infrared laser to measure FLDI signals in stagnant, room temperature air for wavelengths from 1391.98 to 1392.95 nm. The resulting H_2O-induced absorbance was estimated via a standard tunable diode laser absorption spectroscopy (TDLAS) curve fitting approach. Electrical hygrometer and TDLAS measurements of molecular density agreed closely with the estimates. An up-scaled 1-point FLDI was used to record measurements of a small diameter jet using low

humidity air and of the combustion products of a paraffin candle. Further measurements of the Mach 1.5 jet and a Hencken burner flame with equivalence ratios between 1-2 were recorded. These were used to develop a mathematical model incorporating aspects of FLDI and LAS. Comparison of the measurements and model indicates that the absorbing-FLDI (A-FLDI) signal effectively captures and encodes the local absorbance changes in the probe volume, which can then be accessed via the phase shift and individual beam absorbances.

Table of Contents

List of Figures

Section 1: Introduction to FLDI

For over a century, scientists and engineers have sought to understand supersonic flows by optically investigating, measuring, and modeling characteristics like flow velocity and turbulence [1]. Several of the present day's primary engineering applications for these studies include the internal and external flows of high-speed aircraft and rockets [2-5], reactant mixing, ignition processes, and combustion instabilities within supersonic air-breathing combustors [6-8]. Measurement techniques for understanding flow regimes are commonly divided into two categories, intrusive and nonintrusive, based on whether the technique effectively disturbs the flow conditions and thus the resulting measurements. Some of the most reliable and widespread techniques are Hot Wire Anemometry (HWA), Particle Imaging Velocimetry (PIV), Tunable Diode Laser Absorption Spectroscopy (TDLAS) [9-12], and Molecular Tagging Velocimetry [13-15]. HWA measures the heat transfer from a physical sensing element, typically a highly conductive wire connecting two probes, to infer the velocity, temperature, and concentration of the flow. The physical element necessarily disturbs the flow, especially at high speed, thereby altering the original conditions the researcher desired to measure. PIV must employ the use of tracer particles or droplets, which can negatively impact the flow by introducing new flow features and altering flow chemistry [9, 11, 16, 17]. TDLAS suffers from being limited to a measurement that is path integrated and relies upon small variations in a relatively large original signal [18-20]. The MTV technique, as the name implies, either requires additional molecular species for tagging or requires advanced picosecond or femtosecond lasers to deliver enough energy to excite a molecule already in the flow.

Recent developments in Focused Laser Differential Interferometry (FLDI) have provided another tool for high-speed flow diagnostics. Over the 1960s and 1970s, Laser Differential Interferometry (LDI) and its focused version were developed at the French-German Institute of Saint-Louis for analyzing various flow fields and associated phenomena with descriptions of suitable optical arrangements for different conditions. FLDI was found capable of achieving significant attenuation of turbulent disturbances in the boundary layers of supersonic and hypersonic wind tunnels and shock tubes, thereby providing localized measurements of small turbulent structures in the core flow [21]. This ability to achieve localized measurements of various flow characteristics in highly turbulent flows from the supersonic to hypersonic regimes is a primary advantage of FLDI [22]. Later in the 1980s, FLDI received some attention as a technique for measuring shock wave propagation velocity, density distributions, and the impact of shock-boundary layer interactions [23]. However, significant interest in applying FLDI was not renewed until the 21st century upon advances in data acquisition technology.

Throughout the 2000s and 2010s, FLDI was developed to measure minute boundary layer disturbances, flow transition, freestream turbulent disturbances, and compare boundary layer instabilities with stability calculations [22, 24-26]. More recently, Benitez et al. have developed simulations of FLDI to conduct analysis of the sensitivity of the technique to various system parameters [27, 28] and thereby build upon observations from the early development of FLDI [21]. Additionally, various investigations of spectral content have focused on index of refraction fluctuations in nonequilibrium, hypersonic flow [29], freestream turbulence fluctuations in hypersonic flow [30], and developing a robust, quantitative approach to determining density

disturbance spectra from FLDI signals [31, 32]. A combination of FLDI with schlieren imaging and pressure sensors has even allowed for the development of an algorithm to rapidly identify distinct features of hypersonic flow called “wisps” [33].

A substantial improvement of FLDI in recent years emerged through the addition of a diffractive beam splitter, enabling arbitrary linear arrays of laser beam pairs with which to conduct measurements [34]. Around the same time, a similar innovation for easily and greatly increasing the number of measurement locations emerged by employing cylindrical focusing lenses in FLDI [35, 36]. This was later applied in a novel spectral characterization of a plasma jet [37]. These efforts have significantly increased the number of measurement locations in flow fields for an individual test, and this newly created linear array FLDI (LA-FLDI) has seen rapid adoption.

LA-FLDI was utilized to analyze screech phenomena in an underexpanded, Mach 1 jet [38], simultaneously measure the velocity profile and frequency content in a Mach 2 turbulent boundary layer at six positions normal to the wall, 12 FLDI point pairs total, in a Mach 2 blowdown tunnel [39], and to correlate disturbances both within and outside the boundary layer over a blunted cone positioned in the high-enthalpy, hypersonic flow of a reflected shock tunnel [40]. Other applications of LA-FLDI to a blunted cone’s boundary layer explored transitional, high-enthalpy flow through higher-order spectral analysis of the harmonics of second-order instabilities [41] and comparisons with 1 MHz NO planar laser-induced fluorescence imaging [42]. In these experiments, the LA-FLDI signals were collected using arrays of photodiodes, which possess the advantage of being able to reach sampling rates on the order of 100+ MHz. However, commercial availability of suitable photodiode arrays is limited. These LA-FLDI setups tend to require either the creation of

fiber optic arrays connected to equivalent numbers of individual photodiodes or the design and construction of custom photodiode arrays in-house [36, 43]. Efforts to simplify the construction of these custom photodiode arrays have emerged in the form of disassembling individual, commercial photodiodes and recombining their components to create the necessary photodiode arrays [44]. As the size of the FLDI linear array increases, these fiber optic and photodiode arrays become increasingly complex and cumbersome to construct. This complicates their application in both laboratory settings and in modern flight vehicles.

It is evident that in recent decades research into the characteristics of hypersonic flight vehicles has garnered significant interest due to the potential for world-changing advances in both the civilian and military aerospace sectors. If problems like fuselage overheating and excessively strong sonic booms could be effectively mitigated, a hypersonic passenger jet could far exceed the specifications of the well-known but ill-fated Concorde jet and revolutionize air travel as we know it. Commercial spacecraft companies naturally require the ability to experiment with their designs for vehicles needing to withstand the hypersonic flight regime and its associated thermal complications. Of course, the defense industry shares the need for adequate ground testing facilities and the need for effective measurement tools to gather necessary data for refining their designs. Such measurement tools further allow the development of more effective computational techniques for simulating hypersonic flows.

The relentless pace of hypersonic flow research has necessitated the use of a large variety of diagnostic techniques and has resulted in the rapid renewal of interest in certain techniques that are more suitable for the inhospitable testing environments present in

hypersonic ground testing facilities. Despite wider applicability, this has driven focused laser differential interferometry (FLDI) research to hone in on four general areas of measuring turbulence [23, 45-46], density distributions [23, 25-26, 45-49], bulk flow velocity [26, 46, 48-50], and spectral content [22, 31-32, 45-47, 50-54]. As a technique, it measures the phase differences between one or more pairs of closely spaced, focused laser beams generated from the same source and directed through a flow. The phase differences generated near the beam foci translate to peaks and troughs in the intensity signal of the final laser beam after the original beams are brought to interfere and recombined. Its nonintrusive nature allows researchers to conduct measurements with negligible influence on the flow dynamics and chemistry and to avoid destruction of the instrument due to any debris or intense heat transfer that may be present in the test environment.

Since its inception, continued research has shown that FLDI, due to its optical design, notably attenuates the signal effect from turbulent disturbances in the boundary layers of ground test facilities. Additionally, the extent of this attenuation can be modified by adjusting the optics used, which provides flexibility for the technique to be applied to any flow regime [22, 27-28]. However, FLDI is not without its limitations, and its flexibility may allow for additional measurement capabilities, which have yet to be explored or developed.

1.1 FLDI Areas of Improvement

For example, the number of measurement beam pairs in FLDI systems has been increasing significantly in the last several years, which complicates data collection. As before, it is typical for data collection to be achieved using photodiodes [44, 55].

However, a promising avenue for easing the alignment process of FLDI and avoiding the need for complex photodiode arrays is to utilize high-speed camera imaging in their place. To date, this has been little explored and represents a glaring gap in FLDI-related literature [55-56]. A related limitation of FLDI lies in the current methods by which the number of measurement beam pairs are produced. Typically, additional beam pairs are produced in matrix arrangements by diffractive optical elements (DOE) incorporated into traditional FLDI systems, which gives rise to the common moniker linear array-FLDI (LA-FLDI) [55].

Such linear arrays constrict researchers' abilities to make measurements in flows or around models with complex geometries. Furthermore, to produce different beam arrays, different DOEs are required, which notably increases costs over the course of many experiments. A potential solution for this limitation of FLDI is to implement spatial light modulation, which allows the fine control of phase, amplitude, and steering angle of light. To the best of this author's knowledge, spatial light modulation has never been used in an FLDI system and could enable programmatic generation and active manipulation of nonlinear arrays to fit arbitrary shapes, such as the perimeter of a vehicle test model.

Further relating to vehicle design, an overview of FLDI literature indicates that FLDI research has largely been confined to ground test facilities or benchtop experiments with FLDI systems mounted to optical tables or cumbersome rails. To the best of this author's knowledge, there has been no concerted effort to test small-scale FLDI systems under 2 feet. To support future development of FLDI as a sensor embedded into all manner of flight vehicles, it is necessary to work toward filling this gap in the literature by designing, constructing, and testing small-scale FLDI systems.

In addition to these limitations, it is also likely that FLDI's potential applications are not fully fleshed out. In the foundational literature for FLDI, Smeets and George briefly discuss problems that may arise in FLDI measurements as a result of significant absorption of laser energy by certain gas species in the test environment due to the laser wavelength [21]. Although essential to laser absorption spectroscopy techniques, it was seen at the time as a negative factor for FLDI due to its complication of the phase difference measurement. However, recently, a group of researchers studied the use of an infrared laser of an absorbing wavelength in FLDI's predecessor technique LDI to conduct co-linear interferometry and absorption measurements [57]. Absorption techniques are widely known to allow measurements of molecular concentrations of gas species, as well as pressure and temperature. Naturally, this provides inspiration for FLDI. By employing an infrared laser with tunable wavelength in an FLDI system, it may be possible to develop a mathematical model combining characteristics of both absorption spectroscopy and FLDI theory, which can then be used to measure flow properties like gas species concentration, temperature, and pressure in addition to more typical FLDI measurements. Furthermore, FLDI's particular advantage of reducing path-integration effects may translate to these additional measurements.

The different experiments hereafter discussed provide a foundational investigation of those potential solutions by: (1) considering whether a high-speed camera is suitable to replace photodiode arrays for acquiring measurements from FLDI beam arrays via a series of measurements of a moderately underexpanded supersonic free jet from a conical, Mach 1 nozzle, (2) implementing and validating the use of a spatial light modulator (SLM) in FLDI via analysis of a moderately underexpanded supersonic free jet

from a conical, Mach 1.5 nozzle, (3) designing, building, and testing small-scale FLDI systems with tunable diode infrared laser for absorption and FLDI measurements in stagnant air, (4) developing and validating a numerical absorbing-FLDI model via a series of tests with FLDI utilizing a tunable diode infrared laser in different environments.

In the first of these experiments, a high-speed camera, specifically with a maximum sampling rate greater than 0.5 MHz, is used to record images of a 2D, linear array of FLDI laser beams which are produced by a commercially sourced diffractive optic element (DOE) and focused through a well characterized supersonic flow. The signals and resulting power spectral densities of each beam are measured and compared with values obtained from a photodiode for the same jet flow. This is used to assess the advantages and disadvantages of high-speed cameras for acquiring data from arbitrarily sized FLDI arrays in the future.

In the second set of experiments, a commercially sourced spatial light modulator (SLM) is integrated into a traditional 1-point FLDI system to create a spatial light modulated FLDI (SLM-FLDI). This is achieved primarily through replacing the previously utilized DOE with the SLM and implementing additional polarizers and lenses as needed to produce the FLDI beam array with the desired shape, size, and focal region. To test the feasibility of the SLM for use in FLDI, measurements are recorded for both the SLM-FLDI and a traditional 1-point FLDI system at approximately the same region in a well characterized supersonic flow, specifically a free, underexpanded jet produced by a Mach 1.5, conical nozzle. A comparison of the power spectral densities as a function

of frequency is conducted between the two data sets, and this provides the basis for ascertaining the usefulness of SLM-FLDI.

In the third set of experiments, small-scale designs of both 1-point and 2-point FLDI, developed in CAD via Autodesk Fusion 360, are discussed. Commercially sourced components were acquired, and the designs were constructed. The designs will were operated with a tunable diode infrared laser to obtain measurements of FLDI signals in stagnant, room temperature air as the laser wavelength was tuned over a narrow range. The center wavelength of the infrared laser was selected such that significant absorption of laser energy due to the presence of water molecules occured at certain wavelengths within the tunable range. A commercially sourced, electrical hygrometer is also used to obtain comparison measurements of room relative humidity and temperature.

In the final set of experiments, an analysis is conducted of the initial FLDI measurements containing absorption features from room air's water content recorded using the small-scale FLDI designs by applying an existing mathematical model for analyzing absorbance curves from the TDLAS technique. The infrared laser is further utilized with an up-scaled 1-point FLDI design to record measurements of an underexpanded, small diameter jet using low humidity air. Additional measurements are recorded using the same FLDI system on the gas emitted from the flame of a common, paraffin candle. Then, the mathematical model of the traditional FLDI signal is shown to be integrated with the mathematical models utilized in TDLAS data analysis to form the foundation for future analysis work. Further measurements of both the aforementioned jet produced by the Mach 1.5, conical nozzle and the flame generated by a Hencken burner

operated with an equivalence ratio near unity are demonstrated. These measurements are employed to further refine the absorbing-FLDI (A-FLDI) model.

1.2 Technical Impact of this Work

This work adds significantly to the versatility of FLDI by expanding the ways in which FLDI systems can be designed to meet the needs of researchers. It assists in filling, to the best of this author's knowledge, significant gaps in FLDI literature regarding the use of high-speed imaging, spatial light modulation, small-scale implementation, and integration of absorption spectroscopy. Furthermore, it represents the first known use of spatial light modulation in FLDI, which promises the potential to one day create beam arrays that can replicate the perimeter of an entire test model for single-shot measurements. By reducing the scale of FLDI and enabling it to capture information about quantities like number density, pressure, and temperature through combining FLDI and absorption spectroscopy techniques, this work establishes the necessary foundation for FLDI to be used in a wider variety of settings and provide new means by which to analyze flow chemistry.

Due to the attenuation effect of FLDI, its absorbance measurements are less path-integrated and may even provide a desirable alternative to TDLAS. For the field of hypersonic research, the ability to obtain additional measurements with FLDI for the same tests has the potential to save time and money. Ultimately, one can envision FLDI systems developing in time to one day commonly include SLMs, paired with lasers suited for probing transitions relevant to important flow species. One of these SLM-FLDI systems might be able to generate a beam array closely matching the shape of a ground testing model for a hypersonic craft. Instead of photodiodes, a high-speed camera could

be used to capture the entire beam array at a sampling rate suitable for measuring both turbulence spectra and potentially eddy velocity. With the right laser, the absorption of a species like NO could be probed simultaneously, and even further information might be gleaned. Beyond ground testing, small-scale FLDI could become a replacement for hot wire anemometers in weather balloons performing atmospheric turbulence measurements.

At its core though, FLDI is one of many tools at researchers' disposal, and this work is simply about improving that tool. Many examples can be found in history of better tools leading to remarkable things. With any luck, this will become a small part of that long list. With that in mind, it is prudent to begin with some background theory on the topics.

Section 2: Theoretical Background

2.1 Focused Laser Differential Interferometry Model

FLDI is a type of laterally shearing, non-imaging interferometer that splits the wavefront of a continuous wavelength laser beam into two orthogonally polarized beams separated by a small angle. These beams are focused to probe a region of interest, and the beams share very similar, though not identical paths, throughout the test region. The greatest optical path difference occurs at the focal plane, and the system is generally symmetrically arranged. An early depiction of FLDI used by Smeets and George is shown in **Fig. 2.1** [21].

Generally, the beam from a continuous wavelength laser is directed through a waveplate or polarizer. This prepares the polarization vector of the light to properly interact with a beamsplitting optic downstream. The light is then expanded via one or more lenses to some diameter, *D*, through a specialty beamsplitting optic of birefringent material, such as a Wollaston prism. This prism takes the 45-degree linearly polarized light and splits it into an ordinary and extraordinary ray, orthogonally polarized to each other with a constant phase shift governed by the location where the incident laser beam hits the prism. The beams are separated by a small angle, ε, governed by the prism design. As these beams expand, they meet a lens at its focal length from the prism, which focuses the beams into a region of interest. The beams acquire a divergence angle, v, as they are focused to a minimum diameter, $\hat{d}$, at the focal plane. The orthogonally polarized beams are separated by a small distance, Δx, given by Eq. (2.1.1) [21].

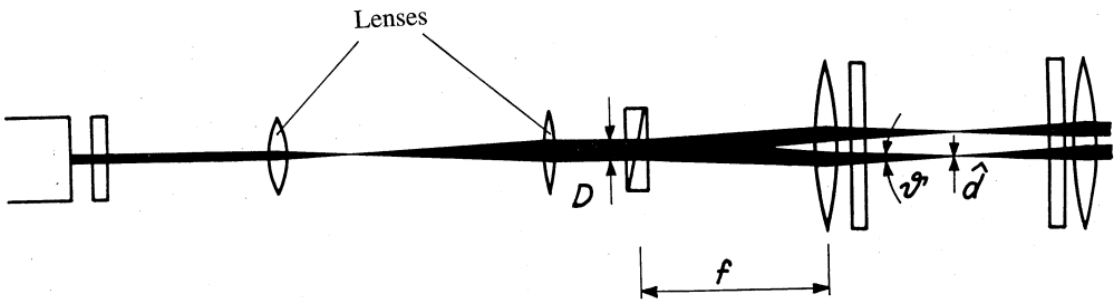

Figure 2.1. Laser-side of focused laser differential interferometer.

$$\Delta x = 2f \tan\frac{\varepsilon}{2} \tag{2.1.1}$$

Clearly, for small angles, Δx is approximately equal to the product of the separation angle and the focal length, *f*, of the lens immediately following the Wollaston prism. Due to the symmetrical arrangement of most FLDI systems, the beams diverge back into an identical lens, which focuses both beams into another Wollaston prism. This recombines the two beams into one, and a subsequent polarizer is generally employed to impart a 45-degree linear polarization to the recombined beam. As a result, coherence is partially restored, and interference fringes appear in the far field. A photodiode is then placed to capture the recombined beam before it diverges too significantly. An additional lens is often placed before the photodiode to improve light collection and provide better imaging. Ultimately, the interference fringes are related to the phase of the recombined beam and the optical path difference of the orthogonally polarized beams. The optical path difference of the orthogonally polarized beams contains two terms, shown in Eq. (2.1.2) [21].

$$\Delta OPL = \Delta OPL_0 + \delta OPL \tag{2.1.2}$$

These terms are the constant, phase shift set by the relative positions of the two Wollaston prisms and a variable phase shift due to a refractive, phase object in the measurement volume. The optical path difference, along with the wavelength of the laser, directly influences the phase shift of the recombined beam, as shown in Eq. (2.1.3) [55].

$$\Delta\varphi = \frac{2\pi}{\lambda}(\Delta OPL) \tag{2.1.3}$$

For the FLDI system to be functional, the “infinite fringe” condition must be achieved. This is done by adjusting the position of the second Wollaston prism and

polarizer pair along the beam axis and making minor rotational adjustments of the pair until the number of visible interference fringes decreases to the infinite fringe case. In this case, a single fringe fills the image plane, and translation of the second prism-polarizer pair causes uniform brightening then darkening to occur in a periodic fashion. Examples of different fringe appearances as one approaches the infinite fringe condition are shown in **Fig. 2.2** [58].

Once the infinite fringe condition is set, it is possible to remove the presence of phase ambiguity in the system. Phase ambiguity adversely affects the signal output of the photodiode by limiting the voltage values that are output. A prime example of this is illustrated in **Fig. 2.3** [59-60].

By translating the second prism-polarizer pair perpendicular to the beam axis or using a Berek compensator, the initial phase shift of the FLDI system can be adjusted. Setting the phase shift to approximately $\pi/2$ radians renders the voltage output of the system without a phase object present to be approximately half the maximum output voltage. Therefore, perturbations in the FLDI measurement volume can produce the maximum variation in the signal output [60]. Mathematically, this is determined by linking the optical path difference in the system's focal region to its signal output. The key to this lies in the refractive indices and densities of the orthogonally polarized beams.

$$\Delta OPL = \int_{s_1} n_1 ds - \int_{s_2} n_2 ds \tag{2.1.4}$$

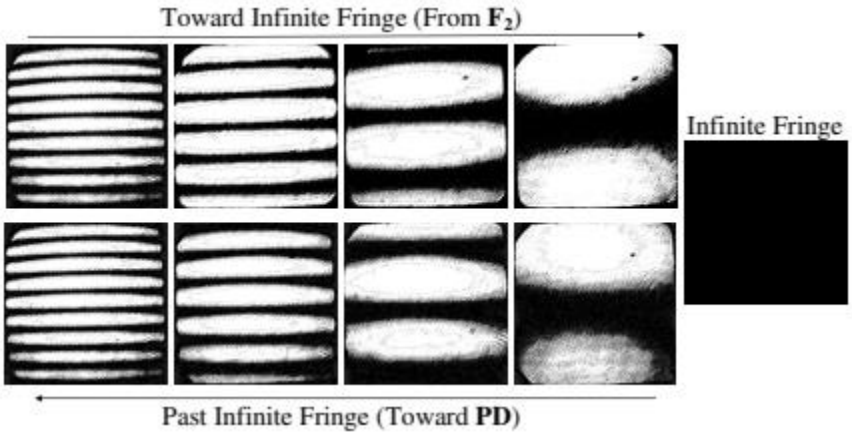

Figure 2.2. Example images of number of interference fringes as one approaches and then passes the infinite fringe state.

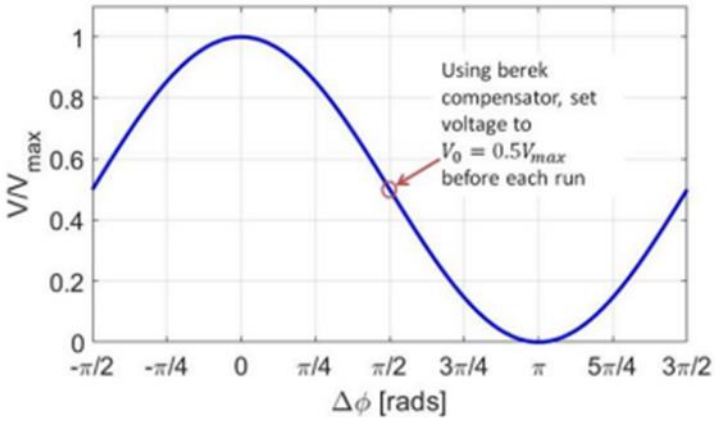

Figure 2.3. Maximum-normalized signal output as a function of FLDI system phase shift.

The relationship between optical path difference and refractive index is expressed in Eq. (2.1.4). It shows that the optical path difference stems from the difference in the refractive indices of the two orthogonally polarized beams of the system along the beam paths, defined by s_1 and s_2. It is generally considered that refractive index, n, is related to density, ρ, through Eq. (2.1.5), known as the Gladstone-Dale Law [55].

$$n = K\rho + 1 \tag{2.1.5}$$

The proportionality value or Gladstone-Dale constant, K, is different for each species and is often experimentally determined. Substituting Eq. (2.1.4) and Eq. (2.1.5) into Eq. (2.1.3) yields Eq. (2.1.6), which links the difference in the densities along the beam paths to the system's phase shift [55].

$$\Delta\varphi = \frac{2\pi K}{\lambda}\left(\int_{s_1} \rho_1 ds - \int_{s_2} \rho_2 ds\right) \tag{2.1.6}$$

Since the early days of FLDI, experiments have shown that the extent of overlap and similarity between the optical paths of the orthogonally polarized beams cause the signal effect of local disturbances away from the focal plane of the system to be attenuated significantly. Therefore, it is generally considered that an FLDI system is sensitive to disturbances occurring within a region defined by a characteristic or sensitive length, L, which is centered around the focal plane and much smaller than the total beam paths. This gives rise to the more common, linearized relationship given in Eq. (2.1.7) [21, 55].

$$\Delta\varphi = \frac{2\pi KL}{\lambda}(\rho_1 - \rho_2) \tag{2.1.7}$$

There is a dependency of the value of L upon the length-scale of disturbances in a flow, which complicates determining L for a given FLDI system. It is possible to estimate using a turbulent, free jet by translating the jet along the beam axis and measuring the average signal magnitude. Eventually, the average signal magnitude plunges as the attenuation takes effect, and the location relative to the focal plane can be recorded [22]. To reach an expression for the voltage output in terms of phase shift, it is important to consider the equation for FLDI system intensity, given by Smeets and George and shown in Eq. (2.1.8) [21].

$$I_T = I_1 + I_2 + 2\sqrt{I_1 I_2}\cos\Delta\varphi \tag{2.1.8}$$

Smeets and George developed Eq. (2.1.8) by summing the electric fields of the two orthogonally polarized beams and accounting for the proportionality between local intensity, I, and the square of the electric field strength, E^2. Thus, the total intensity, I_T, is shown to be the sum of the intensities of the two orthogonally polarized beams, which is then modified by a term where the beam intensities are coupled with the phase shift. As a clear result, disturbances in the sensitive region of the FLDI system significantly influence the signal output. The phase shift can be further related to the output voltage by considering Eq. (2.1.9), which describes the output of a photodiode under typical, linear response [55].

$$V = I A_{PD} \mathcal{R} R_L \tag{2.1.9}$$

By taking the ratio of the total intensity with a phase object to a reference total intensity without a phase object, it is possible to remove the dependency on the detector area, A_{PD}, the resistivity, $\mathcal{R}$, and the load resistance of the photodiode, R_L. It is assumed

that the orthogonally polarized beams each receive approximately the same amount of energy, which yields the ratio given in Eq. (2.1.10) [55].

$$\frac{I_T}{I_{ref}} = \frac{V_T}{V_{ref}} = \frac{I_1 + I_2 + 2\sqrt{I_1 I_2}\, cos(\Delta\varphi)}{I_1 + I_2 + 2\sqrt{I_1 I_2}\, cos(\Delta\varphi_{ref})} = \frac{2I_1 + 2I_1\, cos(\Delta\varphi)}{2I_1 + 2I_1\, cos(\Delta\varphi_{ref})} \qquad (2.1.10)$$

Furthermore, the process of setting the initial phase shift due to the Wollaston prisms to $\pi/2$ radians has the additional advantage of shifting the cosine terms to sine terms via a trigonometric identity. The lack of a phase object for the reference case further implies that the reference phase shift is zero. Taken together, it is possible to greatly simplify Eq. (2.1.10) and obtain Eq. (2.1.11), which very simply expresses the influence of phase changes due to refraction in the measurement volume on the final output.

$$\frac{V_T}{V_{ref}} = \frac{2I_1 - 2I_1 \sin(\Delta\varphi)}{2I_1 - 2I_1\, sin(\Delta\varphi_{ref})} = \frac{2I_1 - 2I_1 \sin(\Delta\varphi)}{2I_1} = 1 - sin(\Delta\varphi) \qquad (2.1.11)$$

Depending on the application, FLDI is also sometimes described using Jones matrix calculus or transfer functions that simulate the response [22, 27]. However, the previously discussed equations represent an accessible entry point for those who may be unfamiliar with FLDI.

To assess the power spectra of the FLDI signals requires determining the normalized power spectral density profile resulting from each signal, which usually involves the application of Welch's method [61]. The approach described by Holladay and Zhang was utilized to obtain the normalized power spectral density profiles in this work [37]. First, the mean signal is calculated and subtracted from each element of the original signal. For triangle wave modulated beams, this can be more accurately achieved

by fitting a triangle wave function and then performing the mean subtraction. Next, the signal is divided into a multitude of segments of some arbitrary length, overlapping by an arbitrary number of points. For simplicity, the number of points is set as half of the segment length for 50% overlap. In this work, the segments are then windowed with Hanning windows of 50 elements each, which can reasonably smooth the spectral profiles without eliminating the peaks at dominant frequencies. The periodogram of each segment is computed by taking the square of the discrete Fourier transform, and all the periodograms are averaged for the result. To enable comparison of the spectra, the resulting power spectral density is then normalized by multiplication with the quotient of the frequency spacing divided by the variance of the mean-subtracted signal.

The next subsection covers the topic of spatial light modulation in a more qualitative sense, as its specific purpose for FLDI will be to produce the additional beams that will feed into an FLDI system similar to a beam splitter. As a result, the fundamental physics of FLDI are not expected to be impacted.

2.2 Spatial Light Modulation

Spatial light modulators (SLMs) are typically composed of liquid crystals (LCs) organized into grids and enclosed in small displays. They can be either reflective or transmissive. Among the different types of LCs, twisted nematic-LC (TN-LC) cells are particularly useful for spatial light modulation. In a typical nematic LC, the molecular centers are randomly distributed, but the molecules are ordered or aligned linearly. In a TN-LC cell, the LC molecules are held within a small cell, and the molecules at the top and bottom are aligned to those surfaces in a perpendicular manner. The interstitial molecules then align themselves to form a helix pattern as depicted in **Fig. 2.4** [62-63].

The valuable characteristic of these TN-LC cells lies in their behavior when a voltage is applied to the constituent molecules. Under an external voltage, the interstitial molecules can be reversibly made to tilt and twist until they align parallel to the applied electric field. Organizing thousands of these tiny cells, each on the order of hundreds of square microns in area, into a grid display and running microscopic circuitry to convey voltage to each cell allows for individual operation of each cell to change the polarization, amplitude, and path of incident light. This gives rise to a programmable optic that exhibits voltage-dependent, birefringent properties, which makes it somewhat akin to a prism whose refractive index is spatially variable and controlled electrically. With the right "map" of how to apply voltage to the different cells, any shape can theoretically be generated from the incident light, especially if additional polarizers are used to finely adjust the input and output polarization [62-63].

Hopefully this serves as a helpful overview of how an SLM can be expected to operate. Its appropriate placement is before the first Wollaston prism, which aligns with the contemporary optical positioning for DOEs in FLDI [55]. Further details will follow in the relevant section. Finally, it is time to present an overview of how laser absorption spectroscopy works, specifically TDLAS.

2.3 Absorption Spectroscopy Model

Laser absorption spectroscopy is a branch of optical diagnostic techniques, which rely on a fundamentally simple concept. At their core, these techniques typically involve utilizing lasers with wavelengths that specifically induce either electronic, vibrational, or rotational transitions of electrons in certain molecules, such as water or carbon dioxide.

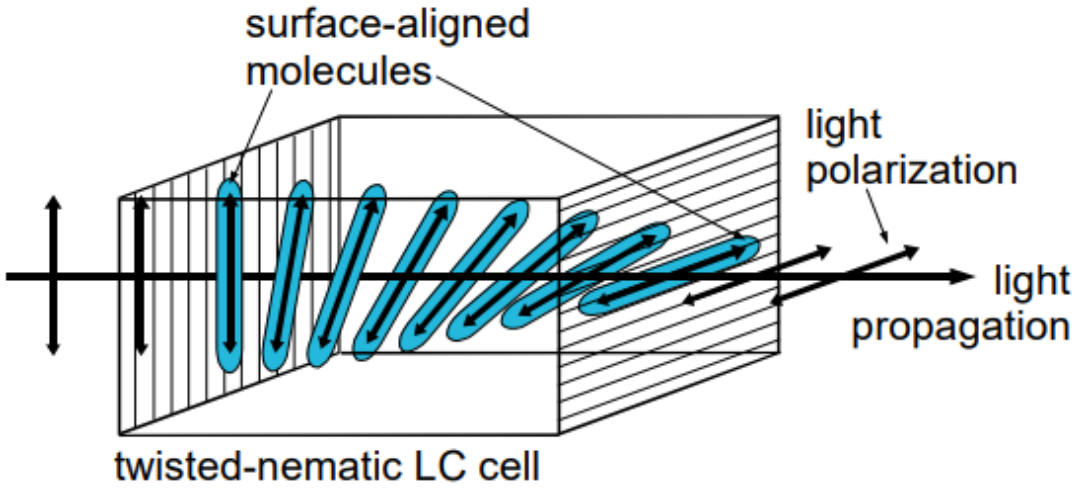

Figure 2.4. Example of TN-LC cell.

The energy of the photons of these particular wavelengths corresponds to the necessary energy for promoting the electrons of the various gas species. These transitions are made possible by absorbing some of the energy from the incident laser, and it is possible to measure the resulting loss of laser intensity using a photodiode for example. This enables species-specific measurements of absorption of energy. The value of these measurements emerges through the application of the Beer-Lambert law, given in Eq. (2.3.1) [64-66].

$$I = I^0 e^{-L\sum_i \sigma^i N^i} \tag{2.3.1}$$

This equation models the transmitted intensity of coherent light, *I*, through an absorbing medium consisting of some number of atomic or molecular species, *i*, which experience non-negligible absorption at the coherent light's wavelength. It represents this transmitted intensity as the product of a non-absorbing, reference intensity, I^0, and an exponential decay term incorporating the optical path length of the light, *L*, the absorption cross-section of a given species, σ^i, and the molecular number density of a given species, N^i. The exponent of the decay term is generally defined as the absorbance, *A*, shown in Eq. (2.3.2) [64-66].

$$A = -\ln {}^{I}/_{I_0} = L\sum_i \sigma^i N^i \tag{2.3.2}$$

From this equation, clearly absorbance can be experimentally measured by measuring the transmitted intensity in the presence of an absorbing species, as well as a reference intensity without the absorbing species. An example setup for direct absorption spectroscopy and TDLAS is depicted in **Fig. 2.5**.

For a single wavelength case, independently measuring the reference intensity is necessary. However, if the current of a tunable diode laser is instead modulated to periodically increase and decrease over a range, the laser's output wavelength can be made to vary over a range of values. For a wide enough range, this results in the laser cycling through both non-absorbing and absorbing wavelengths. Recording the transmitted intensity with a photodiode then reveals a mostly linear trend for the intensity, punctuated by troughs due to absorption at certain wavelengths. This is exhibited in **Fig. 2.6** [65].

Examining Eq. (2.3.2) further reveals that there exists a linear combination of L, σ^i, and N^i that should fit the experimentally measured absorbance data. Generally, L is simple to estimate as the total length from laser output to photodetector. This leaves two unknowns. N^i is held to be approximately constant over the course of a single measurement, so it is the absorption cross-section that varies by wavelength and governs the shape of the curve. The absorption cross-section is influenced by an enormous variety of factors, but the following simplified model has been found to be a close approximation. The absorption cross-section is often represented through Eq. (2.3.3) as the product of the absorption line strength at a wavelength, $S(T)$, with a line shape profile, g_V, in this case one of the many forms of the Voigt lineshape convolution function [67].

$$\sigma = S(T)g_V \tag{2.3.3}$$

The absorption line strength at a given λ or wavenumber, ν, is then represented solely as a function of temperature through Eq. (2.3.4).

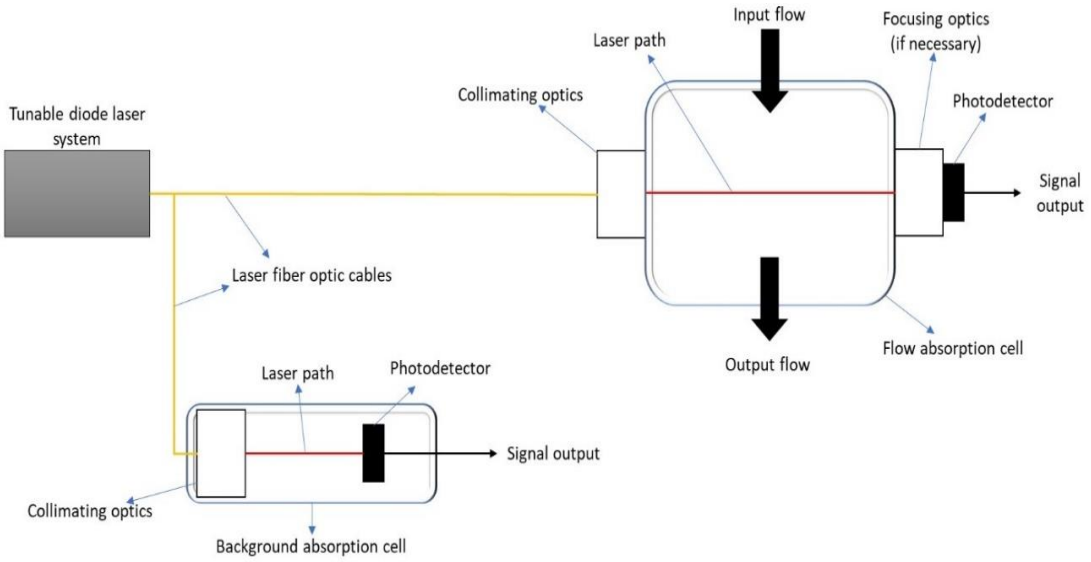

Figure 2.5. Example of laser absorption spectroscopy experimental setup.

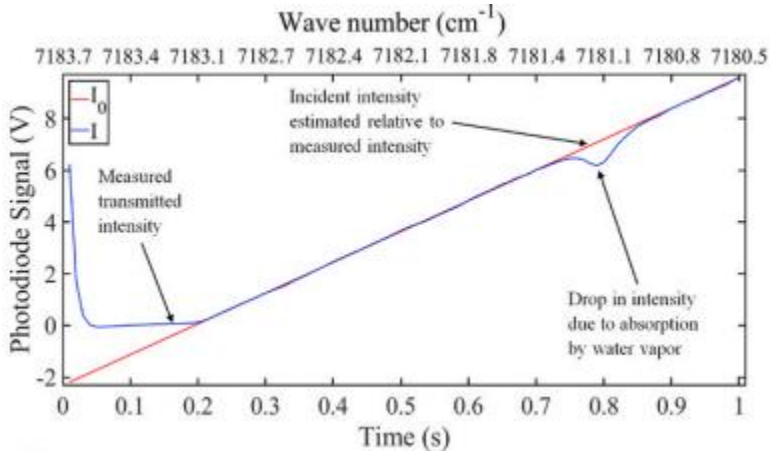

Figure 2.6. Estimation of baseline or non-absorbing intensity from measured intensity.

If the test environment temperature is known and a reference temperature, T_0, is selected, the values of the reference line strength, $S(T_0)$, the partition functions, $Q(T)$ and $Q(T_0)$, the second radiation constant, c_2, and the lower-state transition energy, E'', can all be determined from public databases like HITRAN and HITEMP [68].

$$S(T) = S(T_0)\frac{Q(T)}{Q(T_0)}e^{-c_2E''\left(\frac{1}{T}-\frac{1}{T_0}\right)}\frac{1-e^{-\frac{c_2\nu}{T}}}{1-e^{-\frac{c_2\nu}{T_0}}} \tag{2.3.4}$$

Of course, test environment temperature is not always known, but there does exist a reliable method for obtaining local temperature from the ratio of the line strengths of two different transition lines. This ratio is expressed in Eq. (2.3.5). Rearranging the equation and solving for the temperature yields Eq. (2.3.6) [68].

$$\frac{A_1}{A_2} = \left(\frac{S_1}{S_2}\right)_T = \left(\frac{S_1}{S_2}\right)_{T_0}\exp\left[-\left(\frac{hc}{k_B}\right)\left(E_1'' - E_2''\right)\left(\frac{1}{T}-\frac{1}{T_0}\right)\right] \tag{2.3.5}$$

$$T = \frac{\frac{hc}{k_B}\left(E_2'' - E_1''\right)}{\ln\frac{A_1}{A_2} + \ln\left(\frac{S_2}{S_1}\right)_{T_0} + \frac{hc}{k_B}\frac{\left(E_2'' - E_1''\right)}{T_0}} \tag{2.3.6}$$

In these equations, *h*, *c*, and k_B represent Planck's constant, the speed of light in a vacuum, and Boltzmann's constant. Once line strength for the test conditions is calculated, the extensive task of determining the value of the line shape profile begins. Fortunately, the Voight lineshape convolution function seeks to account for many of the main sources of lineshape broadening, such as Doppler and lifetime broadening, by utilizing aspects of Gaussian and Lorentzian lineshape profiles. Simply put, they attempt to model the effects of physical phenomena on the width of the peaks of the absorbance curve. The value of the lineshape profile can be defined through Eq. (2.3.7) [67].

$$g_V = f_V \frac{v}{v_0} \frac{\tanh \frac{c_2 v}{2T}}{\tanh \frac{c_2 v_0}{2T_0}} \tag{2.3.7}$$

In this equation, v_0 represents the center or transition wavenumber, and c_2 represents the second radiation constant from Planck's Law. The Voight function, f_V, can be represented using an empirically obtained expression given in Eq. (2.3.8) [69].

$$f_V = c_L \frac{\alpha_V}{\pi[(v - v_0)^2 + \alpha_V^2]} + c_G \sqrt{\frac{\ln 2}{\pi}} \frac{e^{-\frac{\ln 2 (v - v_0)^2}{\alpha_V^2}}}{\alpha_V} \tag{2.3.8}$$

In addition to wavenumber, Eq. (2.3.8) is also a function of the half-width of the Voigt line, α_V, and two weighting coefficients for Lorentzian and Gaussian profiles, which are c_L and c_G, respectively. These are defined using an additional dimensionless parameter, *d*, which represents a function of the Lorentzian half-width, α_L, and Doppler half-width, α_D. The functions for c_L and c_G are given by Eq. (2.3.9) and Eq. (2.3.10). The value of *d* is defined by Eq. (2.3.11) [69-70].

$$c_L = 0.6818817 + 0.6129331d - 0.1838439d^2 - 0.1156844d^3 \tag{2.3.9}$$

$$c_G = 0.3246017 - 0.6182531d + 0.1768139d^2 + 0.1210944d^3 \tag{2.3.10}$$

$$d = \frac{\alpha_L - \alpha_D}{\alpha_L + \alpha_D} \tag{2.3.11}$$

A general, empirical expression for the Voigt half-width is given by Eq. (2.3.12) [70].

$$\alpha_V = 0.5346\alpha_L + \sqrt{0.2166\alpha_L^2 + \alpha_D^2} \tag{2.3.12}$$

The Lorentzian and Doppler half-widths are determined using Eq. (2.3.13) and Eq. (2.3.14) [71].

$$\alpha_L = P\left[(1 - \chi)\gamma_{air} + \chi\gamma_{self}\right] \frac{T_0}{T}^{n_{air}} + \frac{1}{2\pi} \frac{A_E}{c} \tag{2.3.13}$$

$$\alpha_D = \sqrt{\left(\Delta f \frac{1}{c - \Delta f \lambda}\right)^2 + (7.1623 \times 10^{-7}) \frac{v_0}{2} \sqrt{\frac{T}{M_W}}^2} \qquad (2.3.14)$$

For these equations, P is the total pressure of the system in atm, χ is the molar fraction (concentration) of the species (unitless, ranging from 0 to 1), γ_x is the Lorentzian HWHM of species x in cm^{-1}, n_{air} is the temperature exponent, A_E is the Einstein A-coefficient in s^{-1} , c is the speed of light in cm/s, M_W is the molecular weight of the absorbing species in g/mol, λ is the nominal wavelength of the laser in cm, and Δf is the optical linewidth of the laser in Hz. Typically, the total pressure for an experiment is a controlled quantity, barring significant losses to total pressure. Most of the remaining quantities can be determined from HITRAN or are already known. The molar fraction is key. As shown in Eq. (2.3.15), the molar fraction is a function of the only remaining unknown, N, the Boltzmann constant and the total temperature and pressure conditions.

$$\chi = {P_{species}}\Big/{P_T} = {N_{species}}\Big/{N_T} = \frac{N_{species} k_B T_T}{P_T} \qquad (2.3.15)$$

Through the use of a least-squares nonlinear curve fitting algorithm with the experimental absorbance data, all of these equations can be iterated over to estimate temperature, partial pressure, and number density of a species. This concludes a brief overview of absorption spectroscopy theory, which will become relevant in later sections. The following section will introduce the experiments conducted to assess the feasibility of high-speed imaging for FLDI.

Section 3: Linear and 2D FLDI Beam Array Measurements with a High-speed Camera for Spectral Characterization of a Free, Underexpanded Jet Flow from a Mach 1, Conical Nozzle

A version of this section was originally published by Seth Holladay and Zhili Zhang and can be found at the following:

Holladay, S.[1], and Zhang, Z.[1] "Linear and 2D arrays for Focused Laser Differential Interferometry using a high-speed camera," Optics Communications Vol. 546, 2023, p. 129754.

Author Affiliations: [1]Department of Mechncial, Aerospace, and Biomedical Engineering, University of Tennessee, Knoxville, TN 37996 USA

Redundant introductory information has been removed for the sake of brevity.

3.1 Experimental Setup

The FLDI system utilized in this work is presented in **Fig. 3.1**, and it constitutes an LA-FLDI with a camera for detecting the full grid and a photodiode for comparing the signal at the grid center. To determine that the camera approach should provide similar results to the photodiode approach, a beam splitter was added after the catch-side polarizer and before the camera to create a second beam grid in a path perpendicular to the original. A high frequency bandwidth photodiode was then placed such that the center point of this new beam grid was incident on the detector surface. With proper photodiode placement, the detector surface is large enough for the center point of the grid alone, but an iris can be used to reduce stray light. Bandpass filters were used to reduce ambient light effects, and a neutral density filter with optical density of 2 was used, out of an abundance of caution, to mitigate the chances of damage to the camera sensor.

The diffractive optical element utilized in this setup generates a 5x5 grid of beam pairs at the focal region of the FLDI system by splitting the incident beam into 25 identical beams, for which a separation angle of 0.5 degrees exists between adjacent beams. The setup was designed to have the beam array's middle row centered on the underexpanded Mach 1 jet, which issued from the nozzle assembly mounted perpendicular to the beam paths. The nozzle was moved via translation stage until it entered the live view of the camera with the grid, and the camera software was used to measure the known nozzle exit diameter and set the image scale.

The geometry of the nozzle utilized is presented in recent work by Price et al. [38]. The separation distance between the orthogonally polarized beams in each pair, depicted by the blue and yellow beam paths, is approximately 0.234 mm, which is a value estimated from the focal length of the focusing lens and the separation angle of 0.067 degrees for the Wollaston prism. This was also measured with the camera at full resolution in the test section via the known pixel pitch and estimated beam centers. The separation distance between each beam pair is approximately 1.7 mm as determined from camera images.

The components of the FLDI setup that were utilized in this work, such as the 12-bit monochrome Photron FASTCAM Mini AX200 camera and the Thorlabs PDA10A2 photodiode, are outlined in more detail in Table A-1, and the setup itself is depicted in **Fig. A-1** through **A-4**. Furthermore, the positions of the optics are detailed. It is hoped this will allow for others to replicate the setup for their own experiments and assess the validity of these results for themselves if desired.

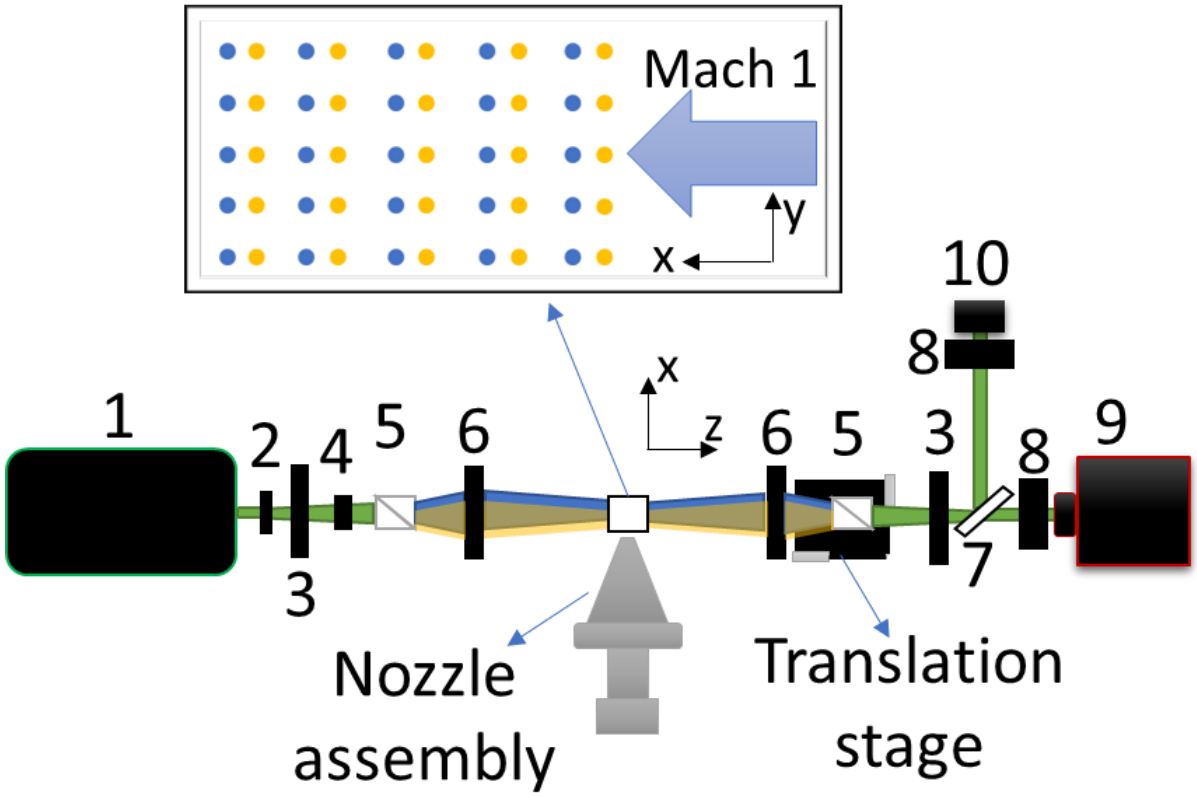

Figure 3.1. Optical setup for FLDI experiment with both high-speed camera and photodiode. The numbered items are (1) Laser, (2) Diverging Lens, (3) Polarizer(s), (4) Diffractive Optical Element, (5) Wollaston Prism(s), (6) Spherical Lens(es), (7) Beam Splitter Plate, (8) Bandpass Filter(s), (9) Camera w/ neutral density filter to protect sensor, (10) Photodiode.

The maximum sampling rates of the camera and photodiode are 900 kHz and 150 MHz, respectively. The size of a camera pixel and the size of the photodiode active area are 0.0004 mm^2 and 0.8 mm^2, respectively. Therefore, a single pixel considers a region of the beam 2000 times smaller than the photodiode.

Measurements of the Mach 1 jet were recorded using the full 5x5 grid, a reduced 3x3 grid about the center point of the full grid, a 1x5 grid formed from the center row of the full grid, and the grid center point at sampling rates of 6.4 kHz, 37.5 kHz, 200 kHz, and 900 kHz, respectively. This provided a frequency range of interest of approximately 0-450 kHz for the camera, and exposure times of 154.54 µs, 24.95 µs, 3.29 µs, and 0.45 µs, respectively, for the different sampling rates. These measurements were conducted at underexpanded conditions, e.g., a nozzle pressure ratio (NPR) of approximately 3 with the test air exiting to ambient room conditions.

The photodiode was used to record the signal from the grid center point in each of the 1x5 and grid center point cases as well at the same sampling frequency or as close as possible. The oscilloscope used in the tests would not allow a 900 kHz sampling rate for the photodiode measurements, so a sampling rate of 1 MHz was used instead in those tests. Due to problems with the available signal delay generator, the photodiode and camera measurements could not be conducted simultaneously by trigger signal but were instead performed manually. Therefore, flow conditions were almost certainly different to some degree. Fortunately, the results still show a surprising level of agreement. The laser was operated at approximately 1 W for the 5x5 and 3x3 tests and 2 W for the 1x5 and grid center point tests to provide high intensity without saturation of the camera.

However, there still exists a degree of separation between the beams as they focus down to the catch-side Wollaston prism. It is conceivable that this causes some differences in the phase shift for the various points of the array in the detector plane of the system, such that some points may deviate from the center of the linear response regime produced by setting the initial phase shift of the system to approximately $\frac{\pi}{2}$. This may partially account for some of the differences in spectra shown in the results. This may potentially be addressed with a half-wave plate or Berek compensator in future exploration of this topic.

3.2 Results and Discussion

An example of the background image, meaning an image recorded without active jet flow, for the FLDI grid center point is portrayed in **Fig. 3.2**. It illustrates the beam formed by the recombination of the orthogonally polarized beams. Images of the center point were obtained at five positions downstream of the nozzle exit, and the image signal was obtained by evaluating the mean intensity of the center point in each image.

To assess if the camera detects spectral content from the FLDI grid similarly to the photodiode that would traditionally be used, the power spectral density was obtained from the recorded signals at each position, and these spectra are illustrated in **Fig. 3.3**. The results reveal that the camera spectra agree reasonably with the photodiode spectra in terms of the dominant frequencies detected and qualitatively in terms of the general profiles' shapes. There are notable differences in the observed magnitude of the power spectral density, which may be a result of inherent differences in the size of the detecting areas and deviations in the amount of intensity absorbed by the filters.

To further assess the usage of the camera as a substitute for photodiode arrays and explore the creation of arbitrary arrays from the images, twelve pixels were selected along the same line within the grid center point images, and the intensity of each pixel was recorded in each image to construct the time-varying signals. The power spectral density was computed for each signal for an additional set of grid center point images recorded at the 1.7 mm position and 900 kHz, where the nozzle was oriented with the flow parallel to the FLDI beam pair separation direction. Images and spectra were obtained for both active flow and a stagnant air background, and the background spectra are illustrated in **Fig. 3.4**.

The background spectra in this case show an even more stark contrast in the observed power spectral density for the camera pixels and the photodiode, and the photodiode results display more fluctuations than the pixel results. The power spectral density disparity is most likely attributable in part to the fact that the photodiode area is significantly larger than that of a single pixel and therefore is subject to more light. Furthermore, the neutral density filter in front of the camera reduces the intensity it receives. Given that the fluctuations in the photodiode spectrum do not appear in the pixel spectra, it is unclear from these results alone that individual pixels are sufficient to capture similar spectral content to the photodiode.

The active flow spectra in **Fig. 3.5** reveal that the results from the pixels and the photodiode agree in two significant aspects. Similar dominant frequencies were detected, and the shapes of the spectra are qualitatively similar.

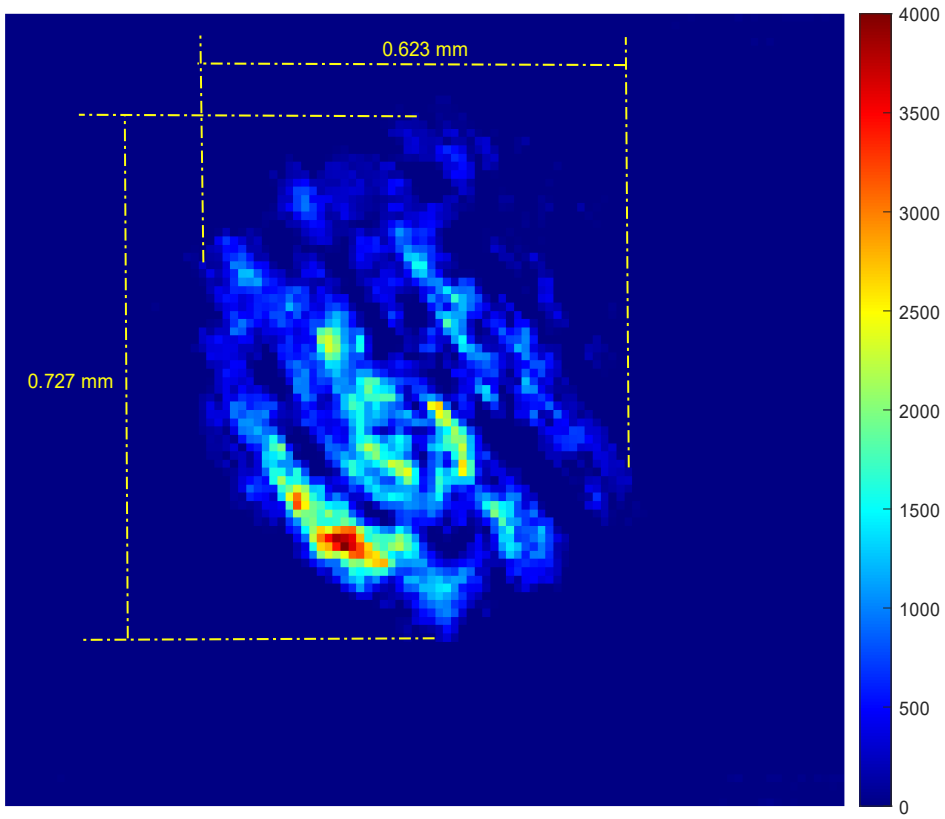

Figure 3.2. Center point of 5x5 grid with nozzle perpendicular to FLDI beam pair separation direction recorded with 12-bit monochrome camera.

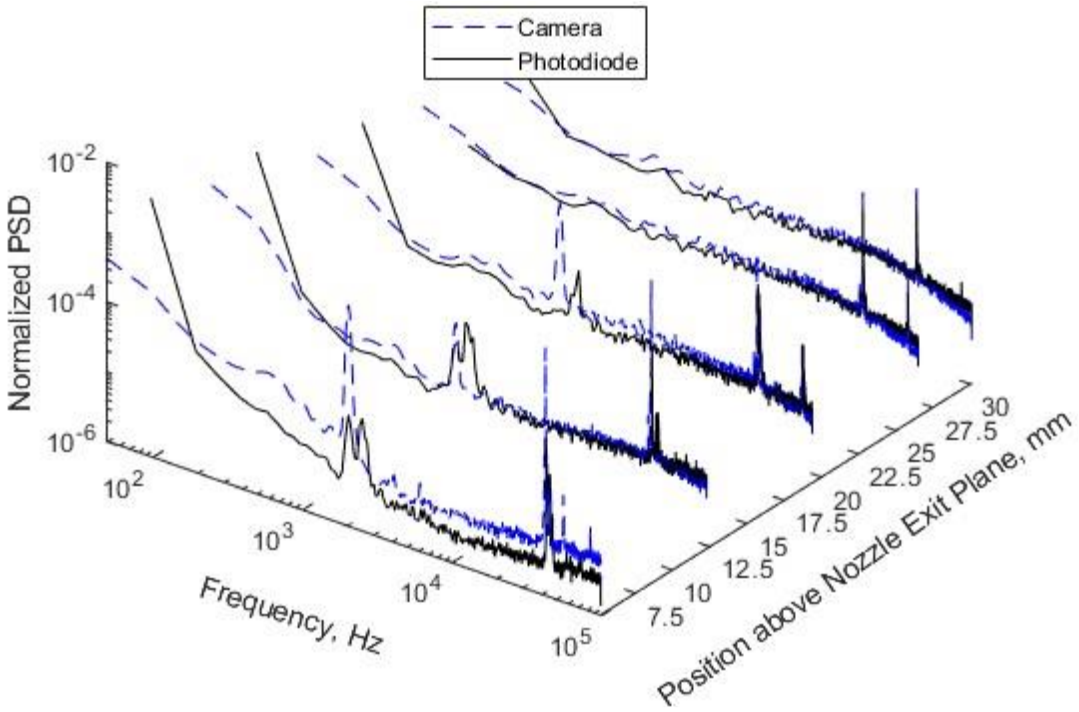

Figure 3.3. Comparison of power spectral density as a function of frequency at center grid point located at different positions above nozzle exit.

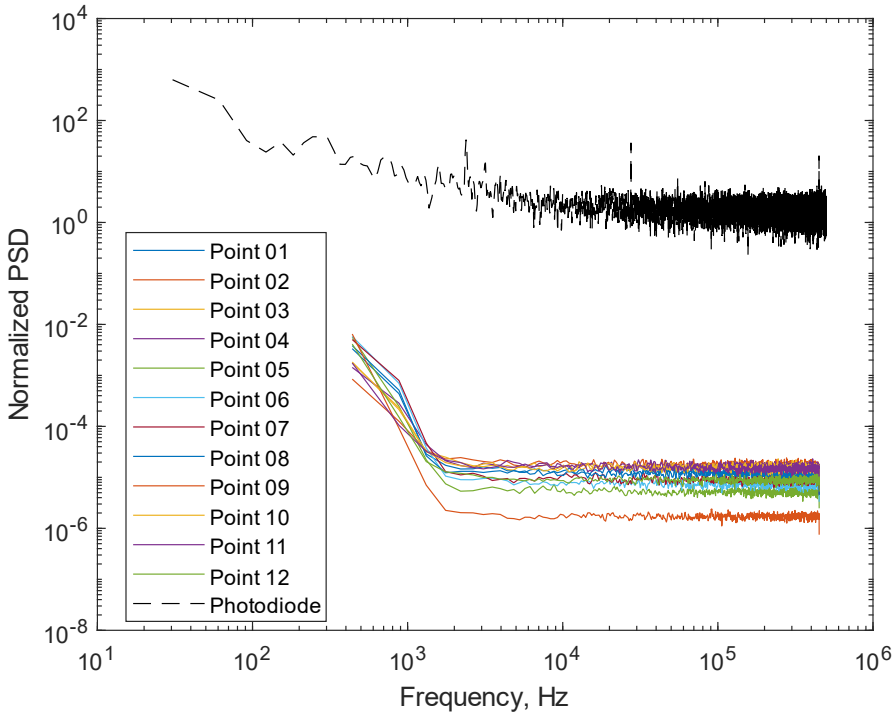

Figure 3.4. Comparison of grid center point power spectral density as a function of frequency without active air flow for individual pixels and photodiode.

However, the photodiode profile maintains a higher power spectral density than the pixel profiles, which stands to reason due to the relative size of the detector areas and the presence of a neutral density filter before the camera sensor. The dominant high frequencies range between approximately 37 and 46 kHz, with the most significant peak at 42 kHz. This range of tones agrees well with the results that were obtained by Price et al. for the screech phenomena at NPRs from 3 to 3.4 in a Mach 1 jet generated from this nozzle design [38]. Although, the dominant tone for an NPR of 3 determined by Price et al. is at 38.9 kHz with a secondary tone at 43.7 kHz, which clearly differs by almost 2 kHz from the results in **Fig. 3.5** and subsequent figures.

However, analog pressure gauges were used in both sets of experiments, and this may have created some ambiguity in the measured NPR. Price et al. show that differences of 0.1 in NPR can produce changes in frequency of approximately 2 kHz in the dominant and subdominant tones [38]. Bearing in mind that the nozzles may have slight differences that affect the flow turbulence, the results in **Fig. 3.5** seem to indicate that the FLDI system in this work demonstrates reasonable estimates of the signal and spectral content for the camera and photodiode from this Mach 1 jet flow. To check the repeatability of this phenomenon, it is important to assess the results for the 1x5 grid of the recombined beams illustrated in **Fig. 3.6**, which were recorded on a different day.

To achieve a sampling rate of 200 kHz while still including the five points, the camera resolution was reduced to 768x16, which slightly truncated the points on the top and bottom. However, the results from the center grid point revealed that even individual pixels can detect similar spectral content, so this is not expected to compromise the results.

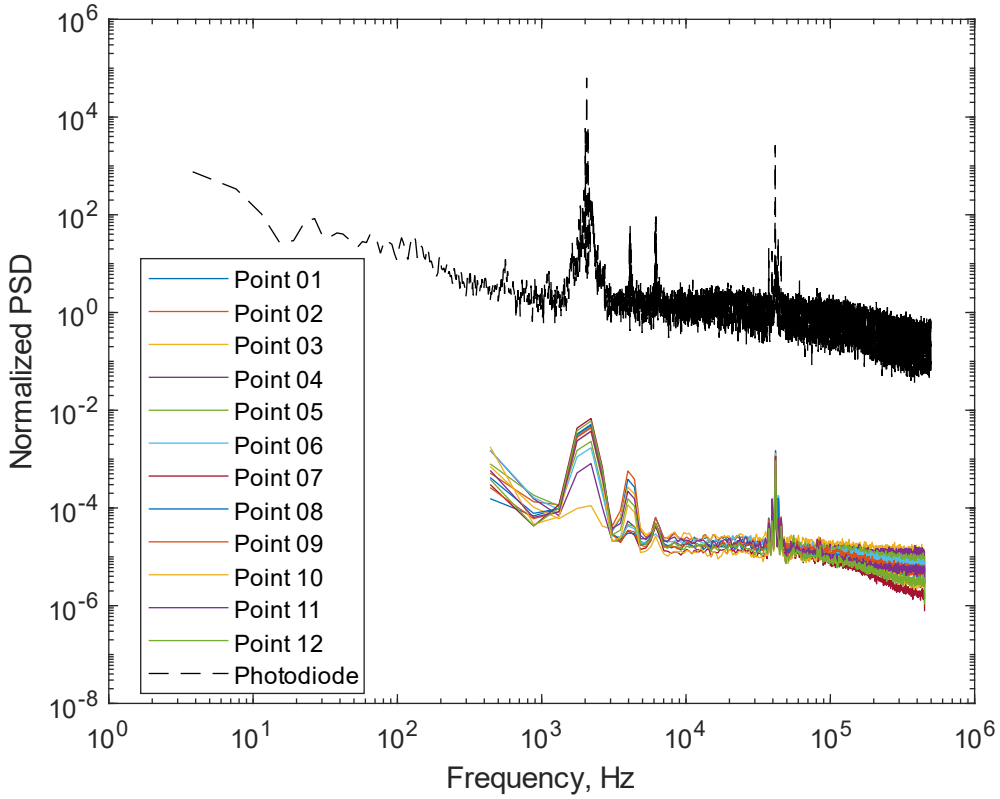

Figure 3.5. Comparison of grid center point power spectral density as a function of frequency with active air flow for individual pixels and photodiode.

Three test runs were conducted with the grid at two different positions relative to the nozzle exit, and the power spectral density was obtained in each case. The profiles in **Fig. 3.7** illustrate the different spectra for each point in the 1x5 array from closest to the nozzle exit to the farthest away, which allows for a representation of the changing spectral content along the flow direction to compare with the earlier results.

The spectra in **Fig. 3.7** reveal consistent detection of the same set of dominant frequencies at each position, but there are some additional frequencies, namely the subdominant 55 kHz and 83 kHz tones, that do not appear in the grid center point results in **Fig. 3.5** but are present for the position-varying results that **Fig. 3.7** portrays. This seems to suggest that the jet conditions may have been slightly different for the second set of grid center point results, either due to differences in the stagnation conditions or nozzle position.

The results in **Fig. 3.8** exhibit continued precision of the measurements and detection of similar dominant and subdominant tones. However, it is clear that the profiles of the spectra for points 3, 4, and 5 changed when the grid points were shifted downstream. Points 3 and 5 began exhibiting a trend of declining power spectral density with increasing frequency, but Point 4 no longer exhibits a steep decline in power spectral density after approximately 55 kHz.

To understand the spatial dependence of the spectra and further examine the efficacy of creating arbitrary arrays from the images' beam matrix, two pixels, spaced 13 pixels apart, were selected from each point in the 1x5 array to generate a 1x10 array for analysis.

Figure 3.6. Strip of 1x5 grid points subject to nozzle flow parallel to FLDI beam pair separation direction recorded with 12-bit monochrome camera.

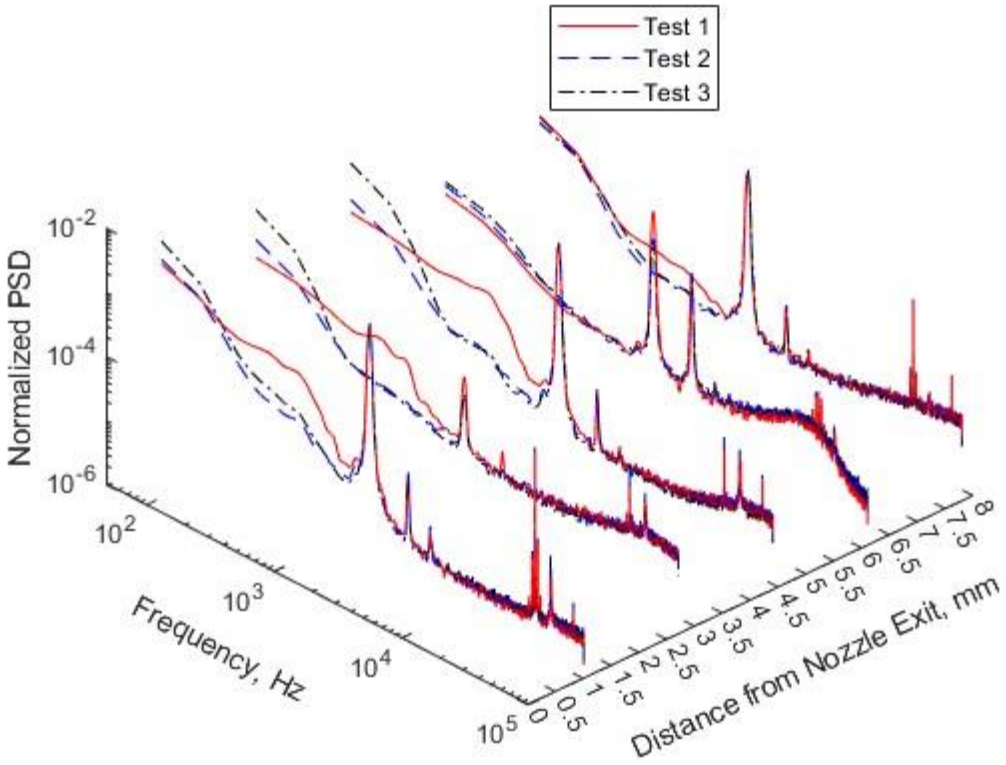

Figure 3.7. Power spectral density as a function of frequency for each point of 1x5 setup at initial position.

This idea is illustrated in **Fig. 3.9**, which should hopefully alleviate any confusion regarding the 1x12 array mentioned previously. As before, the intensity of each pixel was recorded for each image to construct the time-varying signals.

Background signals were recorded for each pixel/point in conjunction with the photodiode, which once again measured the signal on the center point of the 1x5 array. The background signals of the two pixels within the center of the array and that of the photodiode are presented in **Fig. 3.10**. They illustrate that the two pixels appear to be approximately 90° out of phase and fluctuate in intensity to a far greater extent than the photodiode, which is likely due to the photodiode outputting a signal based on all the incident light from the beam point rather than what is received by a single pixel.

However, examining the power spectral density obtained for each of these points and the photodiode over three separate test runs and two different grid positions relative to the nozzle exit once more reveal notable similarity between the camera and photodiode data in detecting the dominant frequencies of the flow. The spectra in **Fig. 3.11** keep the trend demonstrated by the 1x12 array data in which the photodiode spectrum possesses a higher power spectral density generally, but the camera data still picks up the same dominant frequencies.

Upon shifting the grid downstream, a deviation from the trend appears, which is depicted in **Fig. 3.12**. While frequency detection and the profiles remain similar between the data, the photodiode data no longer possesses generally higher power spectral density and instead sits between the spectra from the camera data. Despite this change, the spectra further reinforce the idea that the camera can be employed as a substitute for photodiode arrays.

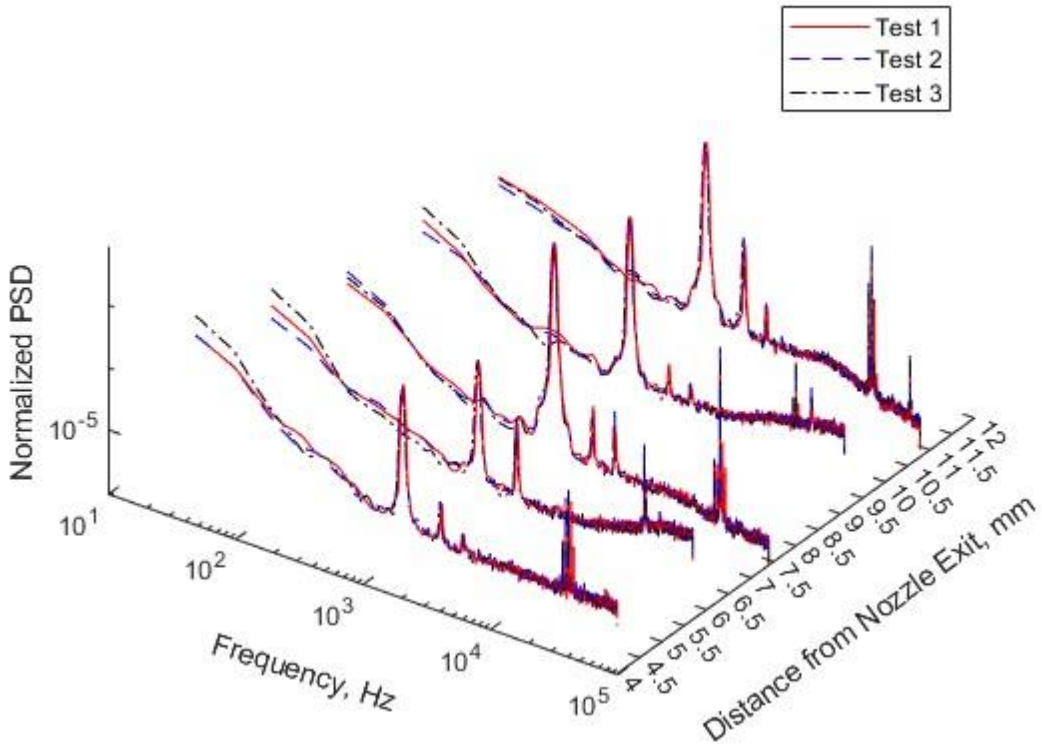

Figure 3.8. Power spectral density as a function of frequency for each point of 1x5 setup shifted 2.97 mm downstream.

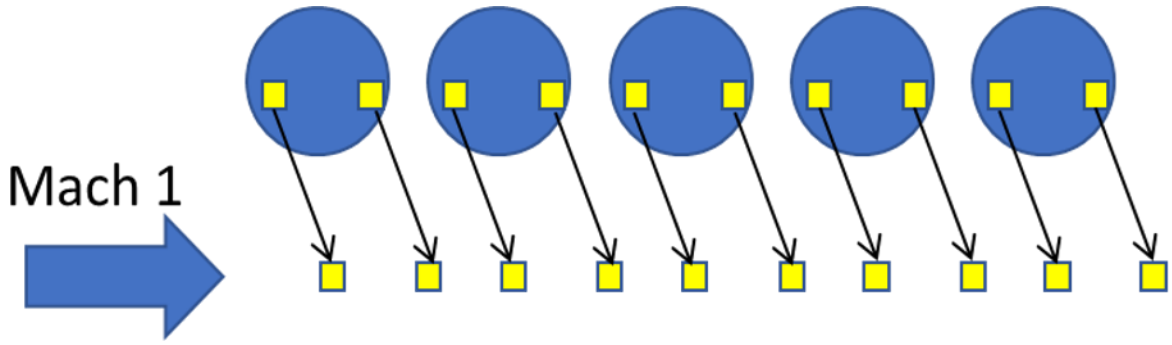

Figure 3.9. Example illustration of 1x10 array extracted from original 1x5 array.

For the sake of providing additional data on the evolution of the spectra of the turbulent Mach 1 jet, **Fig. 3.13** illustrates the changing profile of the flow spectrum throughout the flow. Although there is notable variation between each of the test runs, they still closely track one another. **Fig. 3.13** reveals a significant rolling off of the power spectral density at points 7 and 8. Additionally, other notable changes in spectral profile occur in **Fig. 3.14** at points 9 and 10. They appear to show a general decline in the power spectral density in that region of the flow with increasing frequency. Further tests using cameras with higher max sampling rates may enable successively larger FLDI arrays to be used for measurement of spectral content. Otherwise, frequency detection will be limited as shown in the supplementary material via **Figs. A-5** through **A-8**.

3.3 Concluding Remarks

Taking the full 5x5 array as an example, it is conceivable in the near future that custom diffractive optics may be created to generate FLDI arrays with significantly more laser points, well into the hundreds. Coupling such optics with high-speed cameras may be a beneficial means by which to effectively increase researchers' measurement capabilities to account for the expansion in available measurement locations until more modular photodiode arrays are commercialized. Until high-speed cameras catch up to photodiodes in terms of their sampling rate capabilities, the tradeoff for using camera FLDI seems likely to be lower sampling rate for higher number of simultaneous measurements and greater spatial resolution. Overall, the comparisons of the detection capability of a high-speed camera and photodiode reveal reasonable agreement with regards to dominant frequencies and spectra shape but inconclusive agreement in the spectral magnitude. As a means to pursue more flexibility in beam array generation, the

next section discusses the implementation of a programmable approach for diffractive beamsplitting.

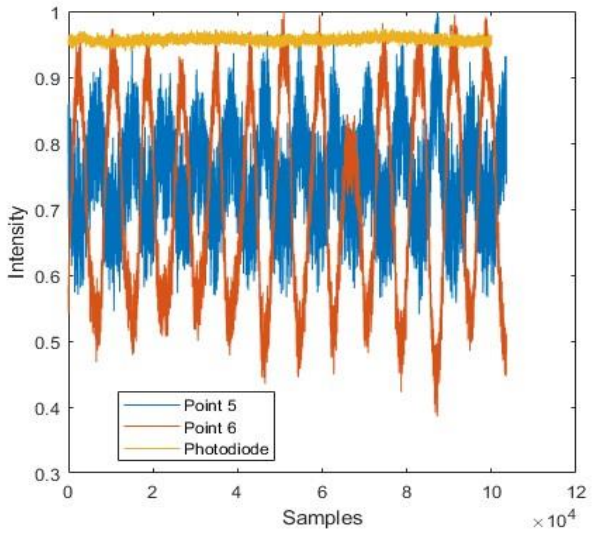

Figure 3.10. Comparison of normalized background signals at grid center point for both individual pixels and photodiode.

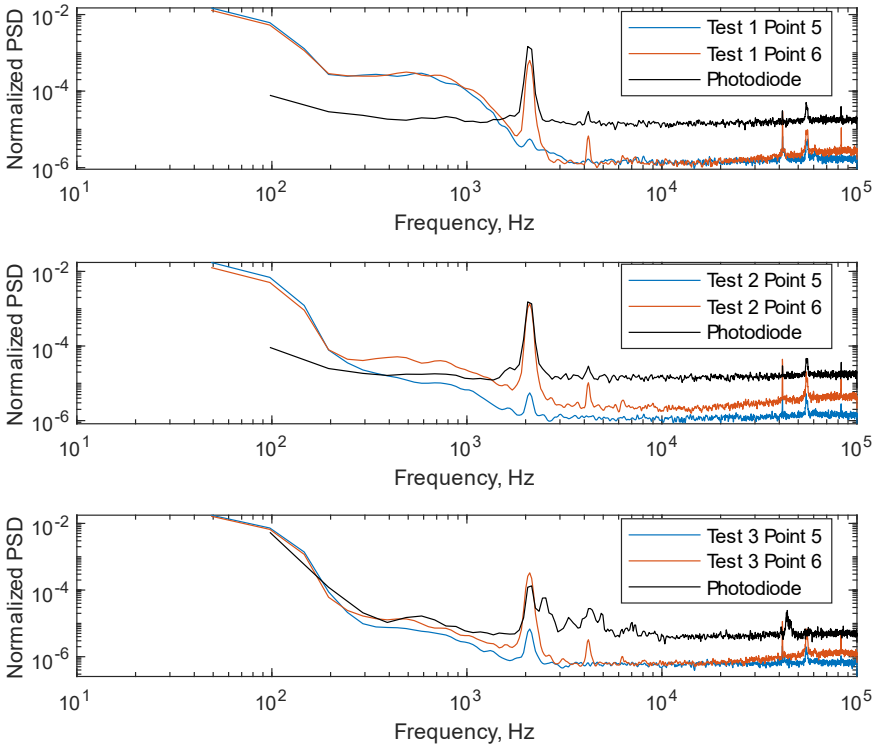

Figure 3.11. Comparison of power spectral density as a function of frequency for photodiode and middle points in 1x10 array at initial position.

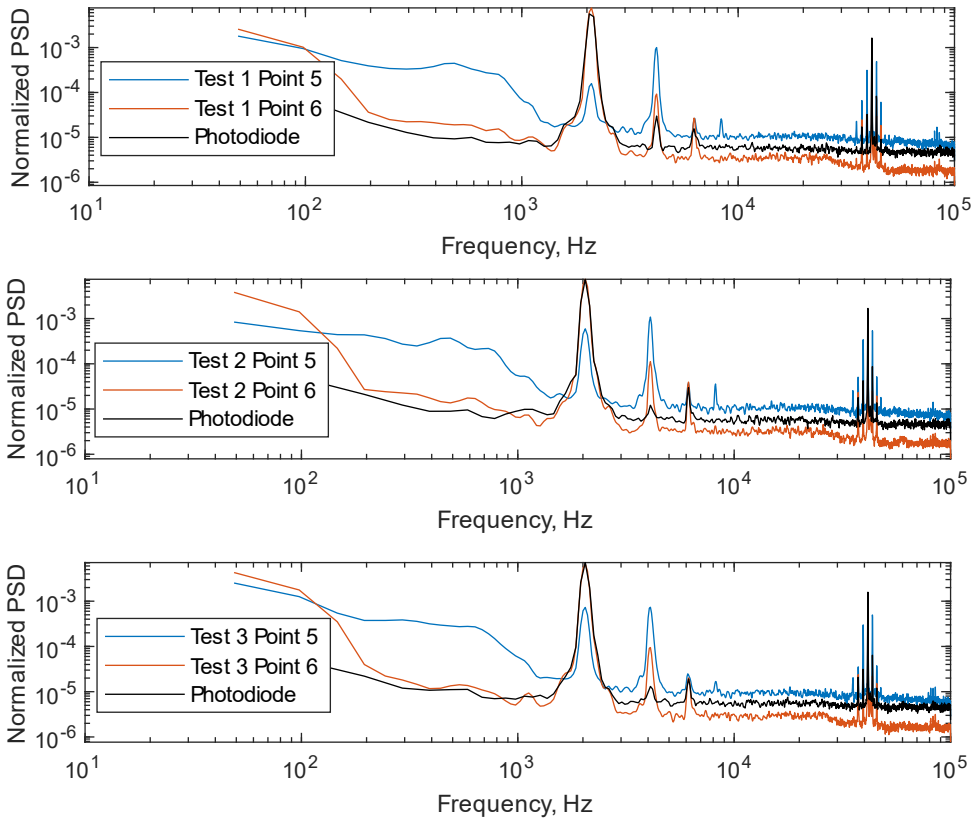

Figure 3.12. Comparison of power spectral density as a function of frequency for photodiode and middle points in 1x10 array shifted 2.97 mm downstream.

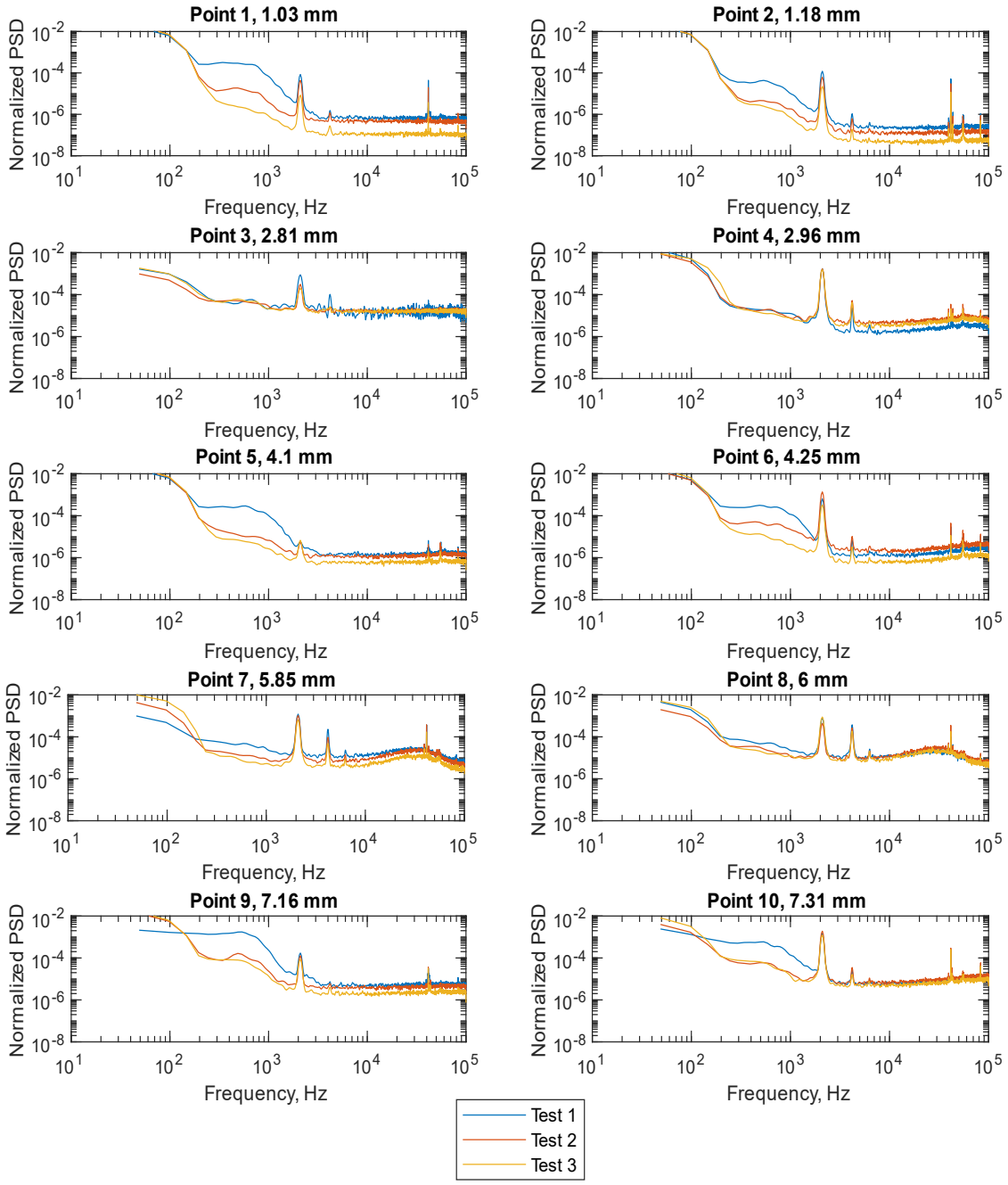

Figure 3.13. Power spectral density as a function of frequency for 1x10 array near the nozzle exit plane.

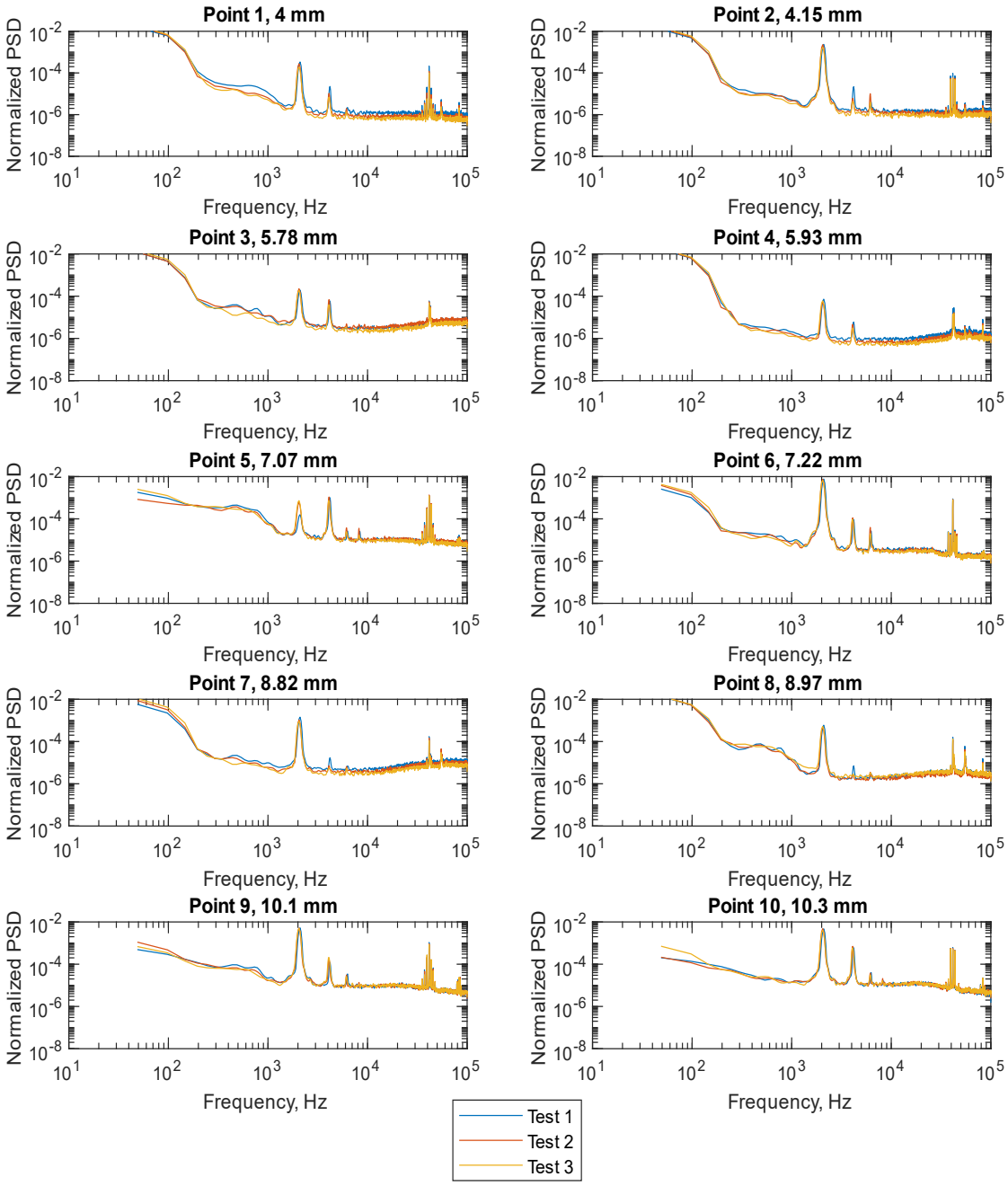

Figure 3.14. Power spectral density as a function of frequency for 1x10 array shifted 2.97 mm downstream from nozzle exit.

Section 4: Programmable FLDI with an SLM as a Dynamic DOE for Spectral Characterization of a Free, Underexpanded Jet Flow from a Mach 1.5, Conical Nozzle

A version of this section was originally published by Seth Holladay and Zhili Zhang and can be found at the following:

Seth Holladay[1] and Zhili Zhang[1], "Programmable focused laser differential interferometer with a spatial light modulator as a dynamic diffractive optical element," Opt. Lett. 48, 5001-5004 (2023).

Author Affiliations: [1]Department of Mechncial, Aerospace, and Biomedical Engineering, University of Tennessee, Knoxville, TN 37996 USA

Redundant introductory information has been removed for the sake of brevity.

4.1 Experimental Setup

After establishing imaging as a useful means by which to record the measurements from large FLDI beam arrays, the use of a spatial light modulator within a traditional FLDI setup is demonstrated to serve as a programmable and dynamic beam splitter for producing beam pair arrays of arbitrary size and shape. SLMs have been widely used in other optical research areas for a variety of measurements, such as other forms of interferometry [72-74], aberration correction [75-76], digital holography [77-78], microscopy [79-80], and pulse shaping [81]. For the experiment hereafter described, a transmissive SLM, specifically a HOLOEYE LC 2012, was integrated into a typical 1-point FLDI setup.

With an appropriate phase function, which influences the voltage addressed at each individual cell or pixel of the SLM, the coherent light transmitted through the SLM can take on any shape. However, the two-dimensional boundary regions of the cells, which contain the wiring, also act as gratings and produce a base diffraction effect for coherent light transmitted through the SLM. This represents one of the key challenges in implementing the SLM into FLDI. Fortunately, producing useful phase functions does not add to the challenges. The accompanying software for this SLM allows for the creation of phase functions for any binary image by solving for the image state using an iterative Fourier transformation algorithm (IFTA) [62, 82-85].

Figure 4.1 shows the integration of the SLM with FLDI. It illustrates the original 532 nm beam in green as it is first split into the array pattern and then further divided into the array of orthogonally polarized beam pairs denoted in blue and yellow by the Wollaston prism. The creation of the beam array is achieved by first expanding and collimating the laser to the approximate size of the active SLM area. This collimated beam passes through a polarizer before entering the SLM. The SLM splits the beam, and the subsequent lens focuses the diffuse beam spot through a polarizer to form a 45° linearly polarized base diffraction effect coupled with the desired beam array. The beams then diverge into another lens that focuses the light into the first Wollaston prism, thereby splitting the beams parallel to the flow into orthogonally polarized beam bundle pairs. The center point of the base diffraction effect and the point ring pattern are then isolated using an iris diaphragm and passed through a focusing lens to the test section, as in 1-point FLDI.

A 1-point FLDI system was constructed and used to measure spectral content of the Mach 1.5 jet at the same pressure conditions and with the same laser as in the SLM-FLDI. This was done to provide reference data for comparison. For the sake of brevity and due to the extensive documentation of 1-point FLDI in the literature, that setup will not be presented here. The Wollaston prisms employed in both setups are specified to possess separation angles of 0.067 degrees. Further details of the underexpanded, free jet of compressed air at Mach 1.5 and the nozzle's design are provided by Price et al [52].

The pattern addressed to the SLM using the software forms around each point in the base diffraction effect caused by the two-dimensional boundaries of the cells. Thus, there is an uneven distribution of the laser energy, where the zeroth diffraction order receives the majority. The pattern itself forms in the Fourier plane of a focusing lens placed immediately after the SLM or becomes visible after diverging for several meters. To reiterate, the SLM TN-LC display that we used naturally diffracts coherent light even without a pattern being addressed.

To illustrate the ability to create nonlinear arrays of arbitrary size, an image of a desired, circular pattern composed of points in a ring was passed into the SLM software, and a corresponding phase function was generated. This phase function was addressed to the SLM to form the pattern shown in **Fig. 4.2** to the left of the blue dotted line. For comparison, the beam pair from the 1-point FLDI setup is shown to the right of the blue dotted line. The separation distance between the beams in each pair and the beam diameters were estimated from the pixel distance in these images and the known pixel pitch of the camera. The beam diameters of the point ring array average approximately 78 μm versus the 61 μm of the 1-point FLDI.

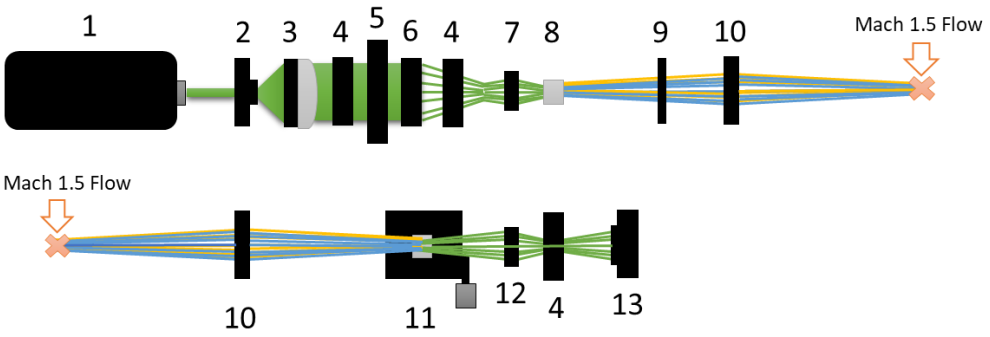

Figure 4.1. Top-down layout of the FLDI setup with incorporated SLM. Components are (1) Verdi V-2 laser, (2) *fl* = 11 mm aspheric lens, (3) *fl* = 50 mm aspheric lens, (4) linear polarizer, (5) SLM, (6) *fl* = 100 mm plano-convex lens, (7) *fl* = 25 mm aspheric lens, (8) Wollaston prism, (9) Iris diaphragm, (10) *fl* = 200 mm plano-convex lens, (11) Wollaston prism on translation stage, (12) *fl* = 50 mm plano-convex lens, (13) Thorlabs PDA10A2 detector.

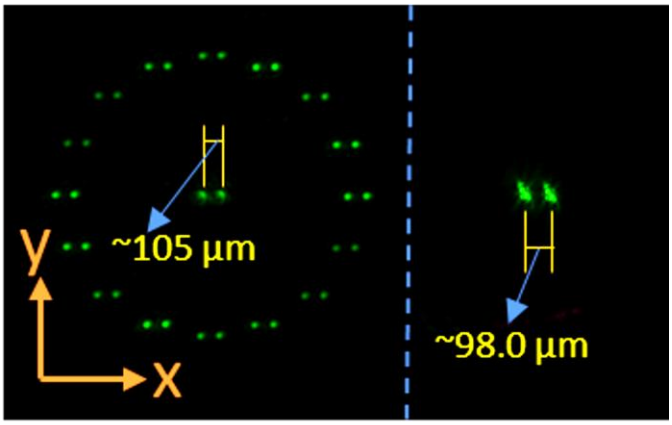

Figure 4.2. Magnified image of the point ring FLDI beam array and the 1-point FLDI in the focal region taken using Nikon D5100 camera.

The Mach 1.5 jet was operated with a nozzle pressure ratio (NPR) of approximately 3 and was centered on the SLM-FLDI array. In this position, the beam array passes between the nozzle exit and the point where the first pair of expansion fans cross. The resulting intensity fluctuations for the zeroth order beam and beams within the point ring were measured using a photodiode across separate tests, and signal fluctuations without flow were also recorded before each test. The sampling rate was 2 MHz, and 1 million entries were recorded for each test.

The measured signals were output as voltage time-series. To process the measured signals and allow them to be compared easily between different tests and FLDI configurations, these signals were used to compute the PSD of the flow as a function of the detectable frequencies in the flow.

4.2 Results and Discussion

The initial results from using the 1-point FLDI on the Mach 1.5 jet are illustrated in **Fig. 4.3**. The laser power was set to 0.01 W, which gave a mean photodiode signal output before tests of approximately 233 mV. In total, 5 background measurements without flow were recorded, and 5 measurements with flow were recorded. The mean value of each set was computed and compared. The results in **Fig. 4.3** are within expectations for this turbulent jet based on my past work at this NPR. A comparison of the tests reveals a rise in PSD, followed by a rolling off of the PSD in the higher frequency region. This coincides with general understanding of the energy cascade in turbulent flows. There is close agreement among the separate tests that result in the mean values. Features of note were identified as certain peaks in PSD at dominant frequencies of the flow, which do not appear in the background.

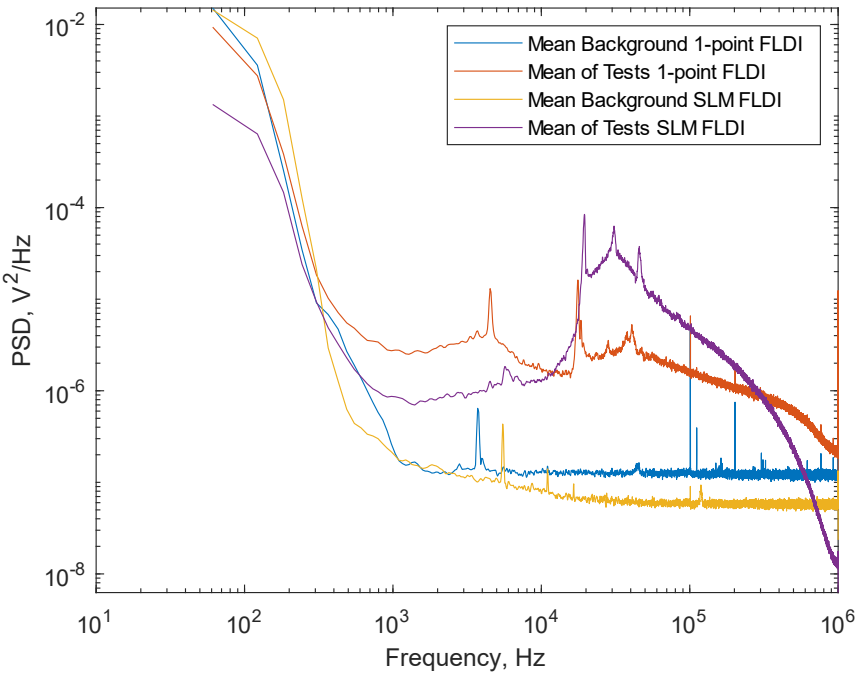

Figure 4.3. Power spectral density as a function of frequency measured by 1-point FLDI and from zeroth order light at center of the point ring array approximately 2.5 mm in x-axis from nozzle exit center.

These occur at several places approximately between 4-5 kHz, 17-18 kHz, 28-29 kHz, and 40-41 kHz. In theory, if the beams in SLM-FLDI detect very similar spectra or at least these PSD peaks at dominant frequencies, there should be reason to believe that SLMs are compatible with FLDI. For the zeroth order light of the point ring array, the majority of the laser energy in the array is concentrated, and it theoretically receives the least modulation [62, 82-85]. Therefore, it was expected to be most like 1-point FLDI.

The SLM-FLDI center point results in **Fig. 4.3** were measured with a higher laser power of 1.50 W, due to greater energy absorption from the additional optics in the SLM-FLDI setup. Anecdotally, increasing laser power past this point resulted in negligible signal output increases. The mean photodiode output was approximately 579 mV. These results show a greater extent of the rolling off of the PSD than in the 1-point FLDI with higher PSD magnitude from around 12 kHz onward. Comparatively, the SLM-FLDI measured the dominant peaks to be approximately between 4-5 kHz, 19-20 kHz, 30-31 kHz, and 45-46 kHz. The faster roll-off may indicate a lack of sensitivity at higher frequencies due to aspects of the SLM-FLDI setup like the beam pair separation distance being larger or perhaps differences in the flow conditions resulting from uncertainty in the pressure conditions. Indeed, the seeming shift in the dominant peaks detected by the SLM could be a result of a slightly different NPR, which may emerge due to the analog nature of the pressure regulator used for this work. Even small variations of 0.1 in the NPR can result in frequency shifts of several kHz in similar underexpanded, turbulent jets [38].

The results in **Fig. 4.4** illustrate spectra recorded at the rightmost point of the array from the center. As a higher spatial order diffraction point, the rightmost point

possesses much less of the total beam energy, which is reflected in the low mean photodiode signal of approximately 8 mV. However, some researchers have devised a way to focus the zeroth order light in a different plane and more evenly distribute the beam energy to the higher diffraction orders in a different focusing plane, which could eventually be applied here [86]. Several of the PSD peaks are detected, including the prominent three around 4-5 kHz, 19-22 kHz, 29-31 kHz, and 43-45 kHz. However, the PSD rolls off much more quickly, which may be attributable to the significantly reduced signal.

4.3 Concluding Remarks

These exterior point spectra suggest that the SLM-generated array provides similar detection of dominant acoustic frequencies to that of 1-point FLDI, at least in this Mach 1.5 jet, but it is achieved at the cost of reduced PSD and greater difficulty detecting higher frequency disturbances. At this early stage, SLM-FLDI is clearly limited in part by uneven distribution of laser energy across the diffraction orders of the modulated array, the seemingly inevitable base diffraction pattern, and the absorption of beam energy by the additional polarizer and SLM in the setup. However, with higher transmission polarizers, higher reflectance or transmission SLMs, and clever combination of lenses and SLM phase modulation, these flaws could realistically be mitigated or overcome entirely. Given the ability to dynamically adjust the steering angles of light transmitted by the SLM, generated arrays could even be shifted in space to an extent without needing to adjust other optics. SLM-FLDI represents a promising avenue for taking advantage of imaging FLDI further due to this potential for creating and rapidly adjusting arbitrarily sized arrays.

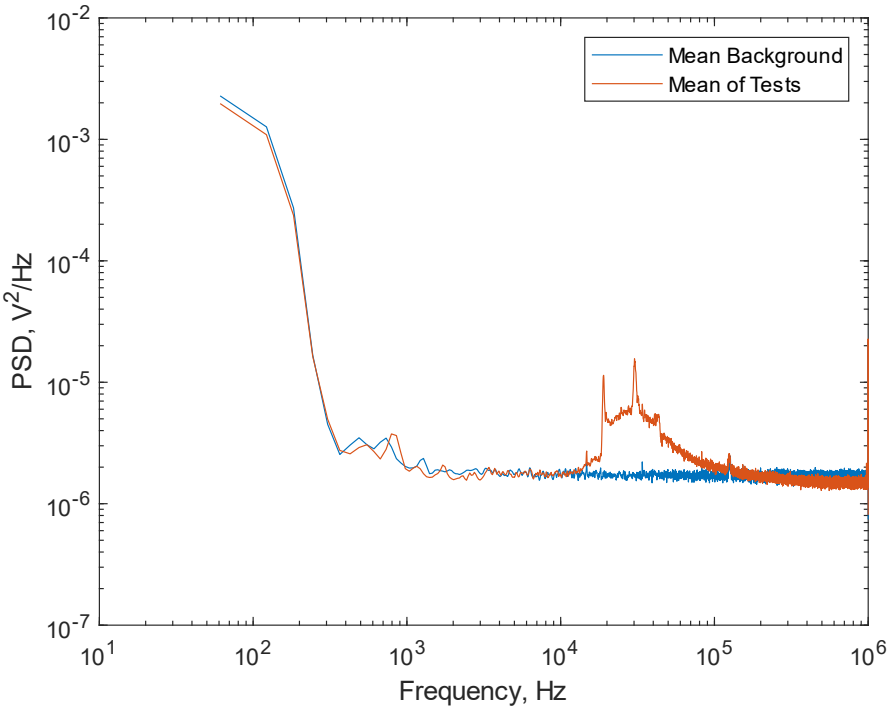

Figure 4.4. Power spectral density as a function of frequency measured at rightmost point of the array, approximately 4 mm in x-axis from nozzle exit center.

To eventually implement FLDI as an easily portable sensor and achieve the ability to measure additional characteristics of flows, some different approaches are needed. The following section will discuss details of the design and testing of small-scale FLDI designs with absorption spectroscopy capabilities.

Section 5: Design, Development, and Use of Small-scale 1-point and 2-point FLDI Systems with Tunable Diode Infrared Laser to Measure Room Temperature Air Water Concentration

For initial testing of an absorbing FLDI (A-FLDI) and implementation of a small-scale design, 2 methods of measuring H2O concentration were used in conjunction with an FLDI setup, which incorporated a tunable diode infrared laser. The first of these methods was H2O TDLAS, which was designed to approximate the optical path length of the A-FLDI system and provide a comparison measurement of concentration. The second method involved the use of an electronic hygrometer, specifically a Protmex HT607, to measure room air relative humidity and temperature. These were then to be used to obtain absolute humidity and, therefore, concentration.

5.1 H_2O TDLAS

An open path TDLAS system was constructed from an EP1392-DM-B diode laser connected by fiber optic to a collimating mount and a Thorlabs PDA10CF photodiode. The path length traversed by the laser beam is approximately 53.4 cm. A Thorlabs ITC4001 is used to introduce a triangle waveform modulation to the laser diode current at 1 kHz with a center current of 0.08 A. This allows for modulation of the laser diode output wavelength around a wavelength of 1392.5 nm where pronounced absorption occurs due to H_2O molecules. The TDLAS system is used to measure a modulated waveform in ambient, laboratory air at 100 MHz. The resulting signal is pictured in **Fig. 5.1**. The TDLAS signal shown in **Fig. 5.1** illustrates 5 main troughs along each “ramp” of the triangle waveform.

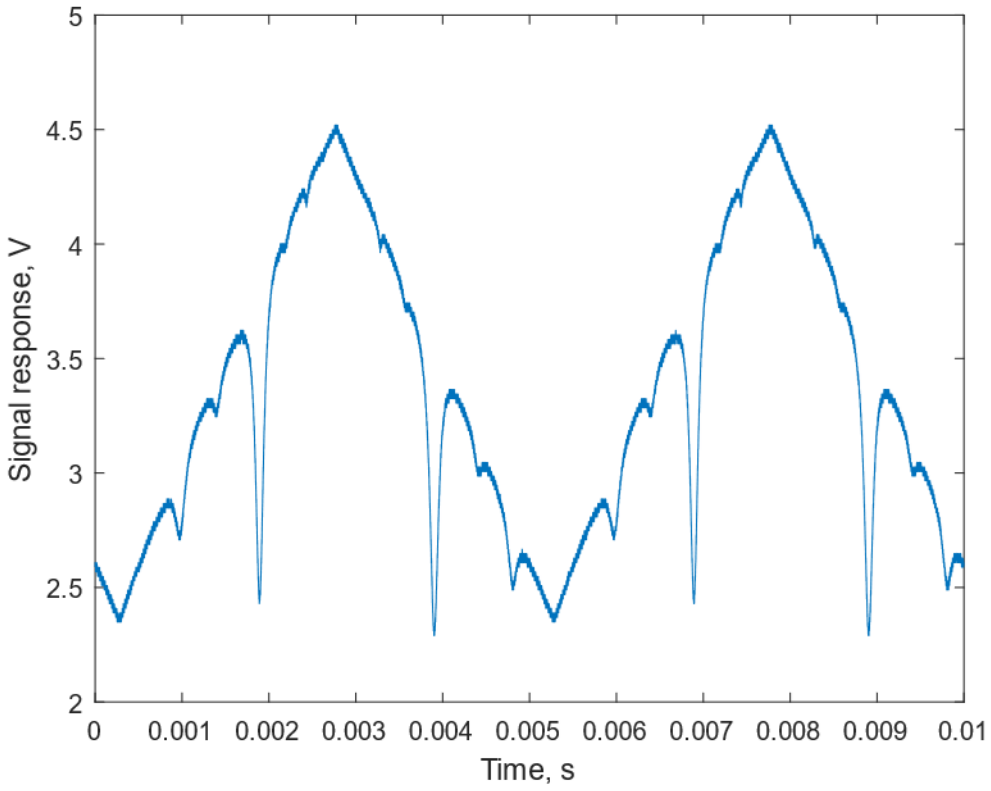

Figure 5.1. TDLAS signal for H2O in room temperature, stagnant air.

These troughs correspond to 5 laser wavelengths that induce the most prominent energy state transitions in H2O at the test conditions. As described in the theory subsection, obtaining the absorbance curve from this signal first requires isolating a segment of the triangle waveform and fitting the baseline. The result of this process is portrayed in **Fig. 5.2**.

The baseline is fit using a 9th order polynomial along the unabsorbing portions of the signal. Since the maximum wavelength range of the laser diode is known to be 1385-1400 nm, the linear relationship between the wavelength and the laser's bias current can be found. It is then relatively straightforward to spline fit the time series of the selected "ramp" from the TDLAS signal to obtain the voltage as a function of wavelength or wavenumber. The measured absorbance curve can then be obtained through Eq. (2.3.2). As described in the theory subsection, an iterative nonlinear curve fitting process can then be executed to obtain a molecular density for which the Beer-Lambert law approximates the measured absorbance. The result of this process is shown in **Fig. 5.3**.

Examining **Fig. 5.3**, it is evident that the estimated molecular density of 3.60E+17 cm^{-3} brings the simulated curve into close agreement with regards to the peaks near 7179.7, 7181.1, and 7182.9 cm^{-1} but is less effective at approximating the two peaks near 7180.4 and 7182.2 cm^{-1}. The exact causes are unknown, but the differences could be a result of one or more factors, such as a pressure shift in the absorbance spectrum, unaccounted for broadening, potential noise in the measured signal, local inaccuracy in the baseline, etc. Despite these deviations from the measured data, comparison with the results for the electrical hygrometer are encouraging.

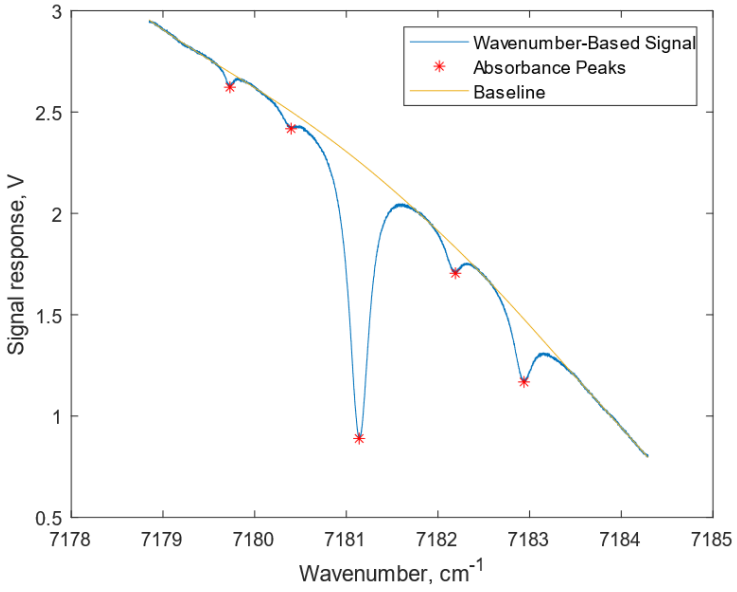

Figure 5.2. TDLAS signal and baseline for H2O in air as a function of wavenumber.

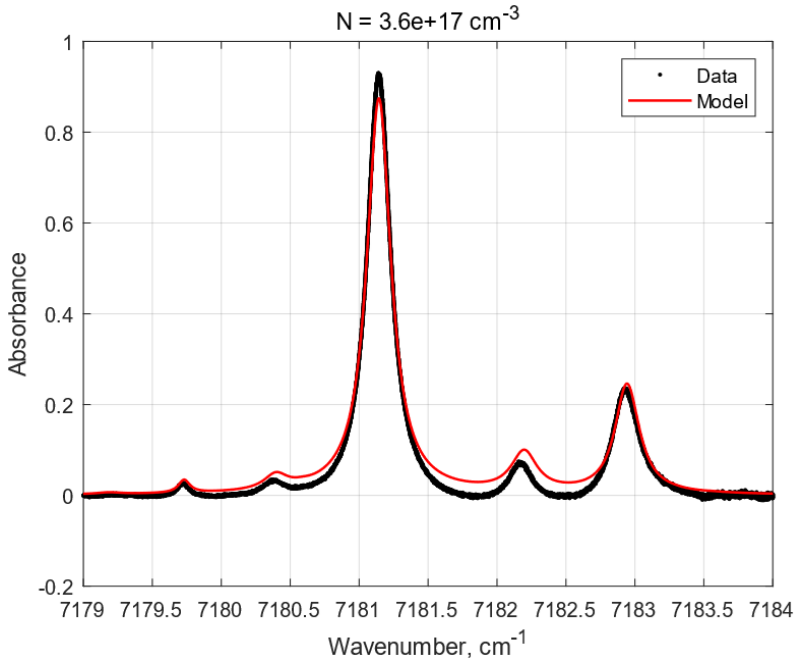

Figure 5.3. Measured and simulated absorbance as a function of wavenumber for H2O in air.

The electrical hygrometer provided a stable reading of 55.5 ± 3% relative humidity and an air temperature of approximately 73.4 ± 2°F. Using Eqs. (5.1.1), (5.1.2), and (2.3.15) to compute saturation vapor pressure, P_s, relative humidity, *RH*, and molecular concentration, allows one to then solve for molecular density. In Eq. (5.1.1), the values of P_c and T_c are the critical pressure and temperature of water, and the values of a_n are empirical constants derived by Wagner and Pruss [87].

$$P_s = P_c e^{\frac{T}{T_c}(a_1\tau + a_2\tau^{1.5} + a_3\tau^3 + a_4\tau^{3.5} + a_5\tau^4 + a_6\tau^{7.5})}, where\ \tau = 1 - \frac{T}{T_c} \tag{5.1.1}$$

$$RH = 100 \times \frac{P_{vapor}}{P_s} \tag{5.1.2}$$

The hygrometer reading provides a range between approximately 3.39E+17 and 4.28E+17 cm^{-3} for the test environment. Since the TDLAS result falls into this range, it was deemed to be functioning suitably for comparison with the A-FLDI result. Furthermore, the electrical hygrometer readings for the room were stable at the same values throughout the A-FLDI tests.

5.2 Experimental Setup for Small-scale 1-point A-FLDI

Due to the early nature of the tests, the A-FLDI measurements were analyzed via the same curve fitting approach with the Beer-Lambert law as the TDLAS data. This was done to begin understanding how the approach could potentially be modified to extend to A-FLDI. The A-FLDI system in question was constructed using the same laser diode, collimating mount, and photodiode as with the TDLAS system. The primary optics of the A-FLDI system arrangement were designed to be implemented as a single unit given by the mockup shown in **Fig. 5.4**. The actual optical path was relatively small due to the use

of short focal length optics, specifically two 11 mm focal length aspheric lenses. Proceeding from left to right in **Fig. 5.4**, a polarizer linearly adjusts the laser beam's polarization to 45°, and this beam is then split into two orthogonally polarized beams by a subsequent Wollaston prism with a 1° separation angle. By trigonometry, this yields an approximate beam separation of 192 μm. The subsequent aspheric lenses provide the focusing into the measurement volume and then back out into the second Wollaston prism, which is identical to the first. A second polarizer, also identical to the first, is oriented in a similar fashion to restore the recombined beam's polarization. The second prism-polarizer pair is mounted in a 2D translation stage to provide the range of motion necessary to achieve the necessary infinite fringe condition and $\pi/2$ initial system phase. The overall optical path length from laser diode to photodiode sensor was approximately 29 cm, but, after accounting for the thicknesses of the intervening optics, this reduces to approximately 24.7 cm. A full view of the A-FLDI system is provided in **Fig. 5.5** for scale.

5.3 Results and Discussion for Small-scale 1-point A-FLDI

As with the TDLAS, the A-FLDI system was used to measure a modulated waveform in ambient, laboratory air at 100 MHz. The laser diode settings remained the same. The resulting signal ramp for one approximate traversal of the modulation range is given in **Fig. 5.6**. The signal exhibits significantly more oscillations than the TDLAS system. As a result, only an absorption trough at 7181.1 cm^{-1} is unambiguously identifiable. The abundance of oscillations in the signal may be due to the phase change detection of the A-FLDI system combined with reduced absorption effects from a shorter path length compared to the TDLAS system.

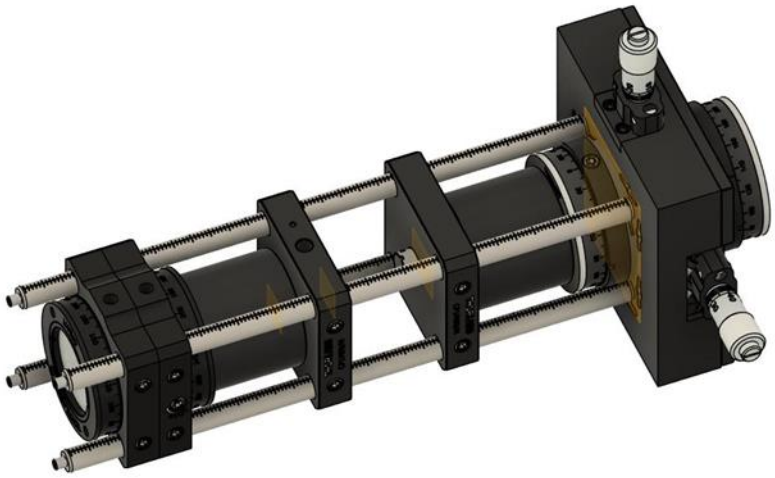

Figure 5.4. Primary optical arrangement of small-scale, 1-point A-FLDI.

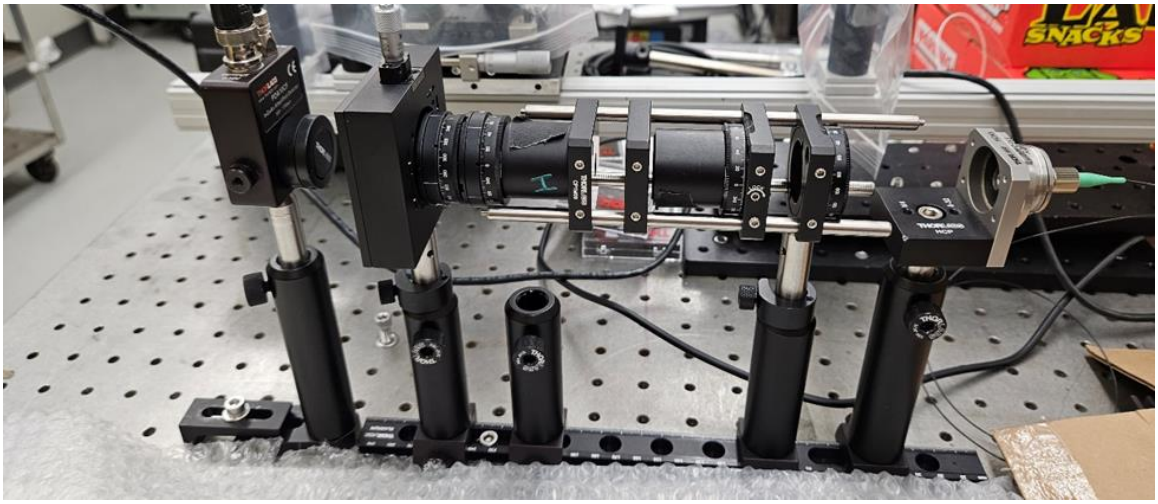

Figure 5.5. Assembled small-scale, 1-point A-FLDI.

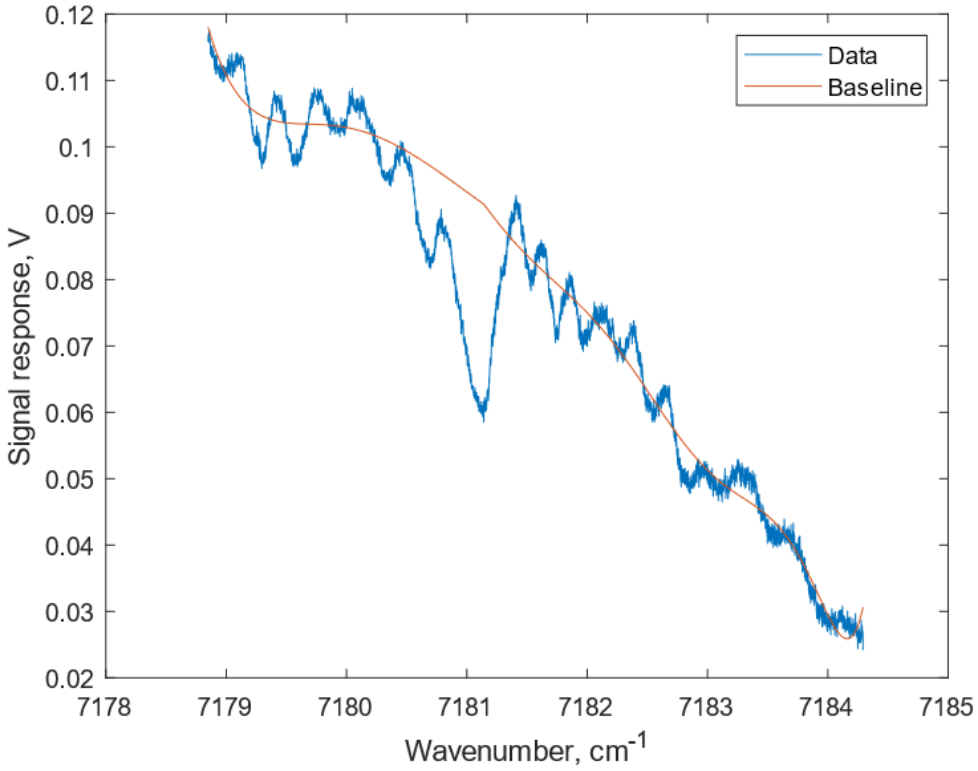

Figure 5.6. A-FLDI open path hygrometry signal in air.

Experimenting with longer path length A-FLDI systems will provide better insight into this phenomenon. Continuing with the calculation of the absorbance from the signal and baseline yields a measured absorbance curve in **Fig. 5.7**.

Due to the ambiguity from the signal oscillations at other wavenumbers, a smaller region of the absorbance curve localized around the 7181.1 cm^{-1} peak was selected to analyze. The red curve in **Fig. 5.7** illustrates the initial estimate of the absorbance before iteratively solving for the molecular density. Clearly the initial estimate overshoots the absorbance peak significantly. After the solver terminates, the resulting model and measured data are shown in **Fig. 5.8**.

The final estimate of the molecular density is approximately 3.82E+17 cm^{-3}, and this does seem to approximate the peak more closely than one might expect. However, as the absorbance falls off from its peak, the estimation becomes increasingly less accurate for this data. Despite this, the molecular density estimation shows surprisingly close agreement with the TDLAS estimate of 3.60E+17 cm^{-3} and the hygrometer estimated range of 3.39E+17 to 4.28E+17 cm^{-3}.

5.4 Experimental Setup for Small-scale 2-point A-FLDI

To further test the implementation of absorption spectroscopy techniques in a scaled down FLDI system, a 2-point FLDI system was designed. The A-FLDI system in question was constructed using the same laser diode, collimating mount, and photodiode as with the TDLAS system. The primary optics of this A-FLDI system arrangement were also designed to be implemented as a single unit given by the mockup shown in **Fig. 5.9**. The actual optical path was necessarily larger than in the 1-point design.

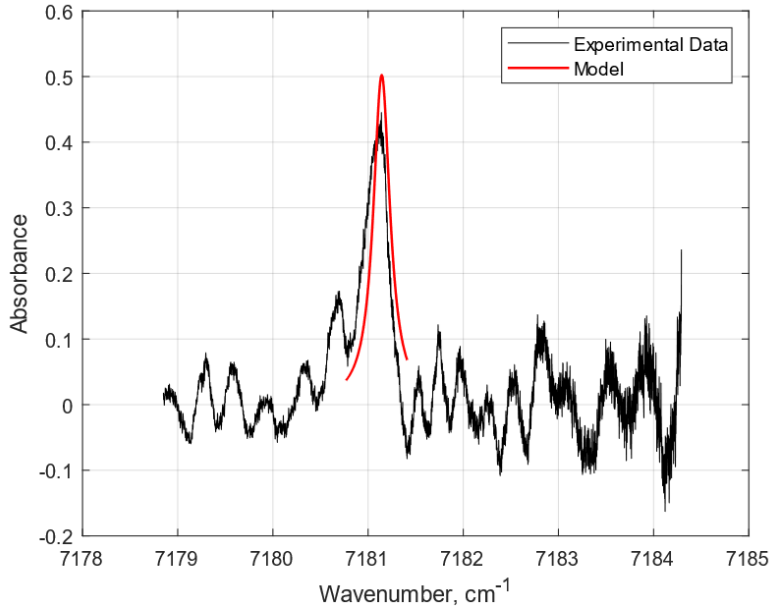

Figure 5.7. A-FLDI measured and initially simulated absorbance as a function of wavenumber for H_2O in air.

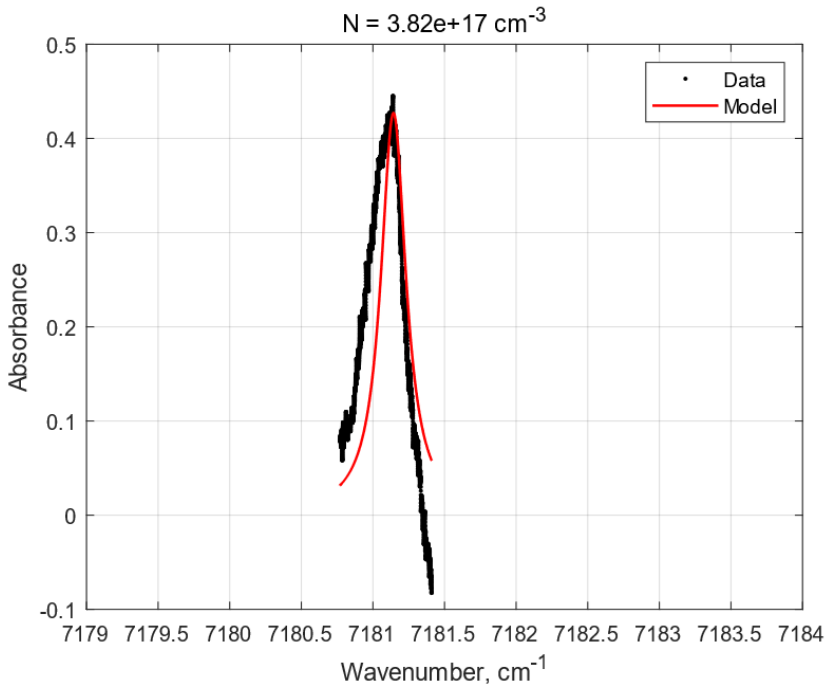

Figure 5.8. A-FLDI measured and simulated absorbance as a function of wavenumber for H_2O in air.

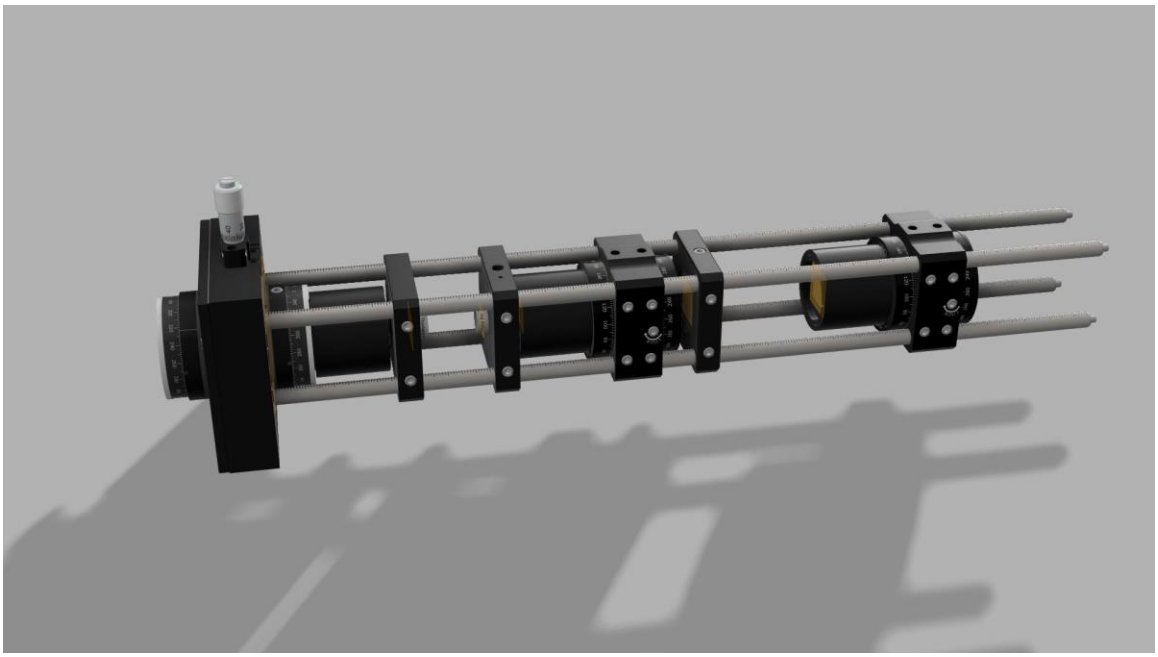

Figure 5.9. Primary optical arrangement of small-scale, 2-point A-FLDI.

In the process of constructing the system, it was found that the aspheric lenses needed to be swapped out for lenses with greater focal lengths in order to focus in the correct planes. As a result, the aspheric lenses for this system had focal lengths of 18.4 mm. Proceeding from left to right in **Fig. 5.9**, a polarizer linearly adjusts the laser beam's polarization to 45°, and then the beam is focused into the center of the first Wollaston prism by a biconvex lens with 50 mm focal length. This beam is then split into two orthogonally polarized beams by that Wollaston prism with a 1° separation angle.

These two beams then diverge into a subsequent polarizer, which again linearly adjust the beams' polarizations to 45°, and on into a 2nd Wollaston prism. This Wollaston prism splits the incident beams into two beam pairs. By trigonometry, this yields an approximate separation between the beam pairs at the focal region of 2.23 mm and a beam separation within a pair of approximately 321 μm.

The subsequent aspheric lenses provide the focusing into the measurement volume and then back out into the 3rd Wollaston prism, which is identical to the previous two. A 3rd polarizer, also identical to the others, is oriented in a similar fashion to restore the recombined beams' polarizations. The 3rd prism-polarizer pair is mounted in a 2D translation stage to provide the range of motion necessary to achieve the necessary infinite fringe condition and $\pi/2$ initial system phase. The overall optical path length from laser diode to photodiode sensor was approximately 54.3 cm, but, after accounting for the thicknesses of the intervening optics, this reduces to approximately 44.3 cm.

For the sake of simplicity, a single photodiode was used to measure each beam signal, but a small high-speed camera or photodiode array could be substituted to record both signals simultaneously. The laser fiber optic can be mounted directly in line with the

other optics for easy alignment. A full view of this A-FLDI system is provided in **Fig. 5.10** for scale. An example of the interference fringes during the alignment process with a red HeNe laser is shown in **Fig. 5.11**. This illustrates that the system behaves as expected prior to full alignment.

5.5 Results and Discussion for Small-scale 2-point A-FLDI

Similarly to the 1-point system, this 2-point A-FLDI system was used to measure a modulated waveform in ambient, laboratory air, but the sampling rate was lowered to a more reasonable 5 MHz. This was done to better resolve individual cycles of the signal, and this was enabled by lowering the laser diode modulation rate to 20 Hz. The resulting signal ramps for one approximate traversal of the modulation range for each beam are given in **Fig. 5.12** and **Fig. 5.13**. Like the 1-point data, both beam signals exhibit significantly more oscillations than the TDLAS system. However, evidence of another prominent absorbance trough near 7182.9 cm^{-1} is apparent in each signal. This improvement in detection may be a result of the adjustments to the sampling and modulation rates, longer path length, or perhaps slightly improved system alignment. Fortunately, the baseline runs very smoothly through the center of the oscillations in the unabsorbing wavenumbers. The oscillations are once again most likely a combination of random noise and phase shift in the signals.

The primary difference between the two signals lies in their respective magnitudes. This is due to the use of an iris diaphragm when isolating each beam for measurement on the photodiode. More of the second beam was occluded than the first, but this has a virtually negligible effect when assessing their absorbance curves, as shown in **Fig. 5.14** and **Fig. 5.15**.

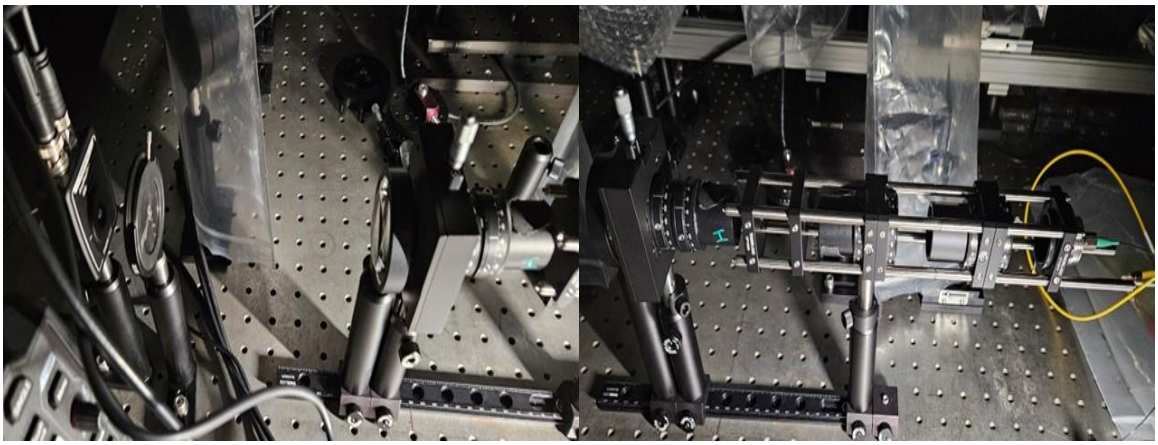

Figure 5.10. Assembled small-scale, 2-point A-FLDI.

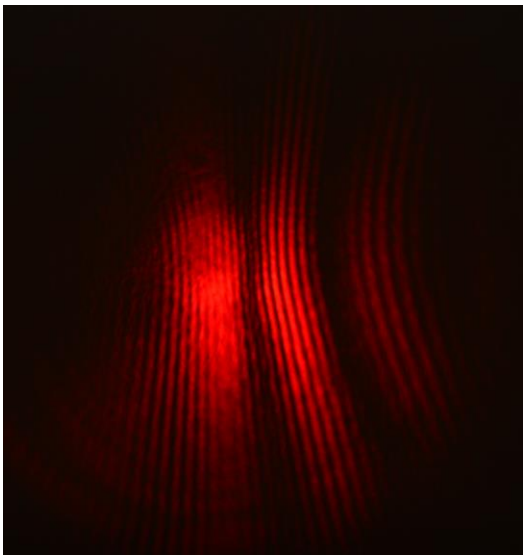

Figure 5.11. Interference fringes from 2-point A-FLDI system.

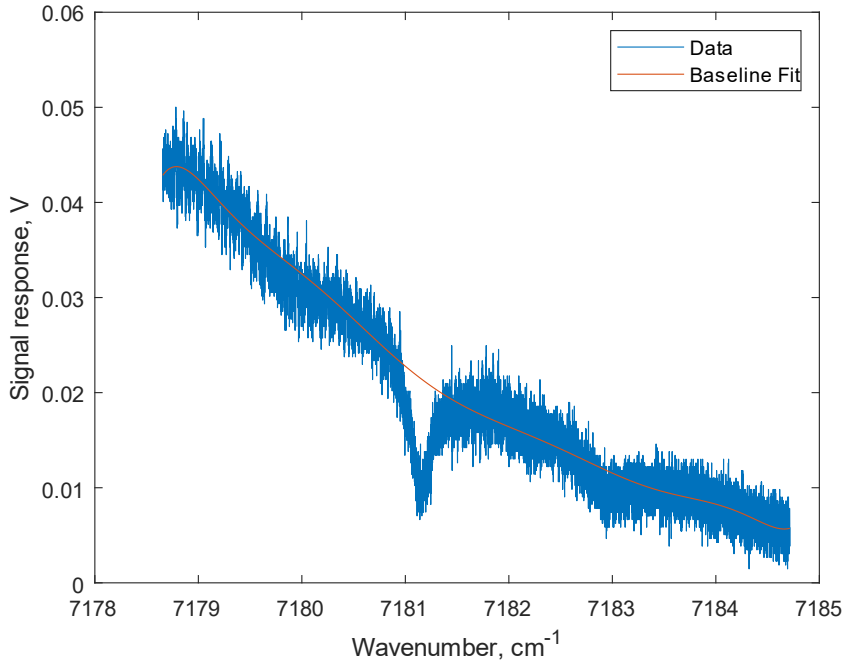

Figure 5.12. Open path hygrometry signal in air of beam 1 of 2-point A-FLDI.

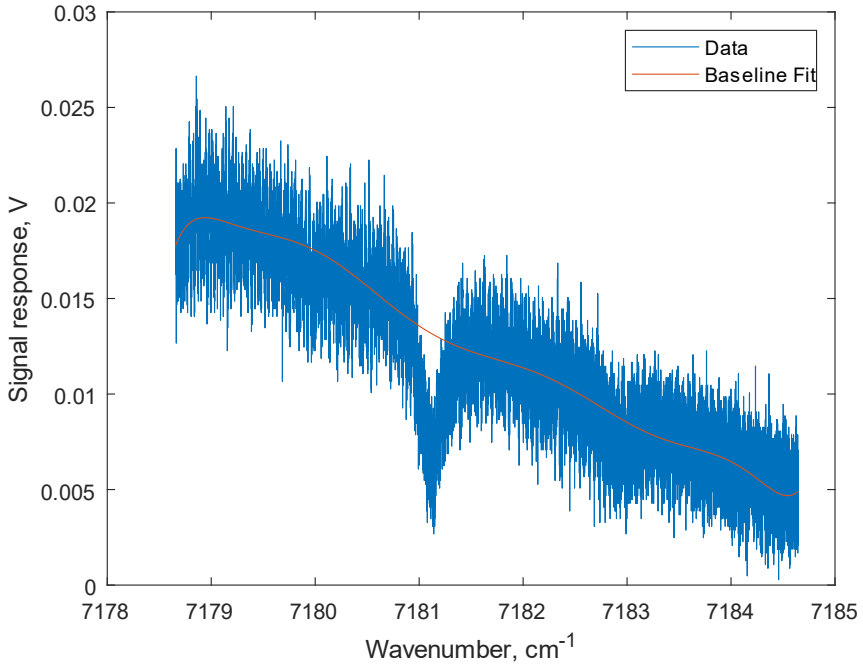

Figure 5.13. Open path hygrometry signal in air of beam 2 of 2-point A-FLDI.

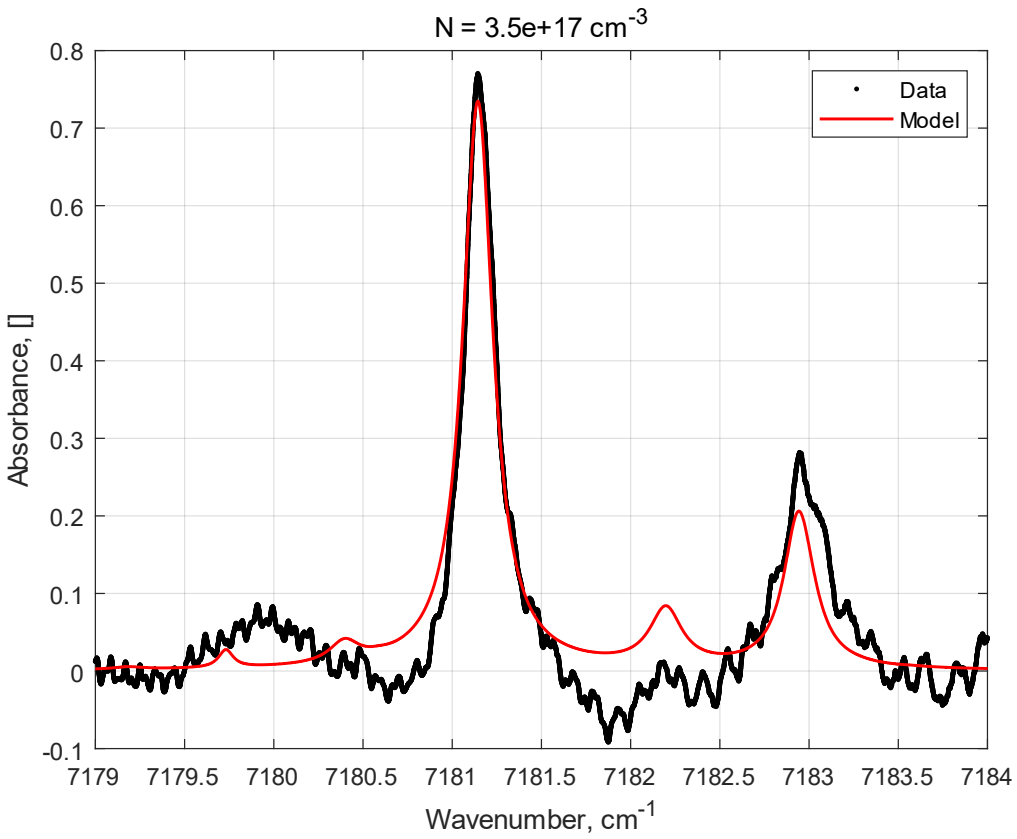

Figure 5.14. Measured and simulated absorbance as a function of wavenumber for H_2O in air for beam 1 of 2-point A-FLDI.

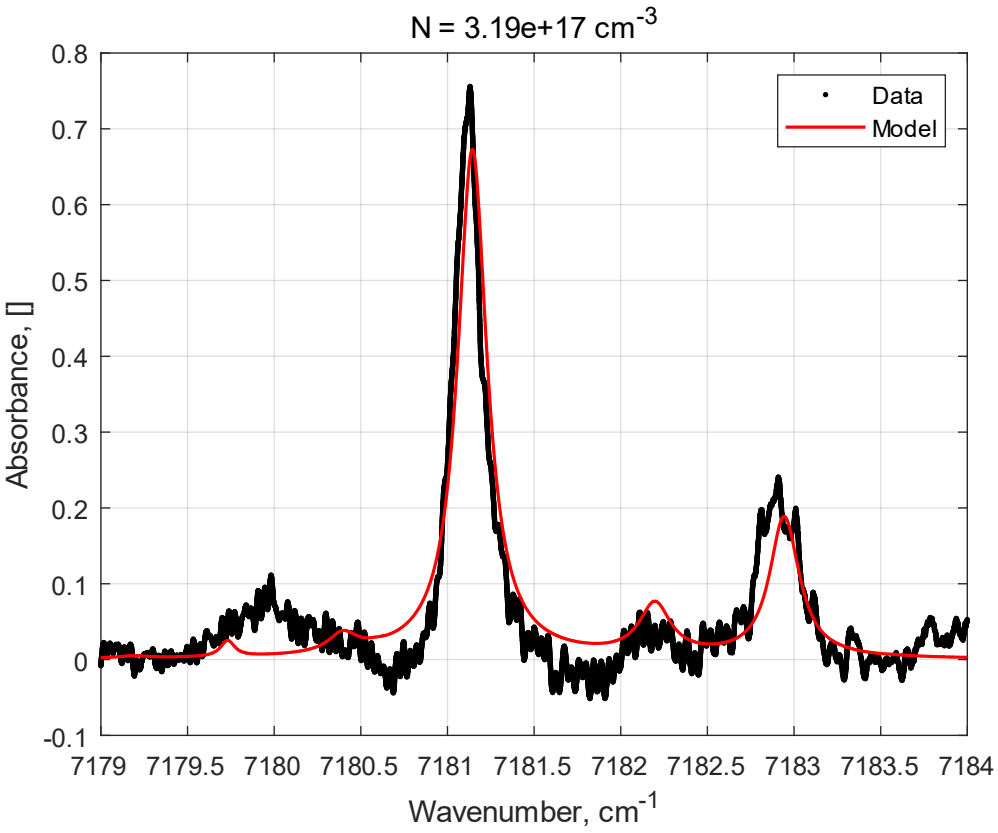

Figure 5.15. Measured and simulated absorbance as a function of wavenumber for H_2O in air for beam 2 of 2-point A-FLDI.

Although there remains some ambiguity from the signal oscillations at other wavenumbers, it is clear that the simulated absorbance curves approximate the general shape of the data. In **Fig. 5.14**, the agreement at the most prominent peak is extremely strong, and the second most prominent peak at 7182.9 cm^{-1} shows a reasonable similarity to the fits. Furthermore, the molecular density estimate of 3.5E+17 cm^{-3} from **Fig. 5.14** falls well within the hygrometer measurement range of 3.32E+17 to 4.11E+17 cm^{-3} for the time of testing.

In **Fig. 5.15**, the agreement at the most prominent peak is not as strong, but the second most prominent peak at 7182.9 cm^{-1} shows a more reasonable similarity to the fit. There even appears to be detection of the peak at 7182.2 cm^{-1} and marginal agreement with the simulated curve. However, the molecular density estimate of 3.19E+17 cm^{-3} from **Fig. 5.15** falls slightly outside of the hygrometer measurement range of 3.32E+17 to 4.11E+17 cm^{-3} for the time of testing. Given that there appears to be a slight rightward shift of the simulated curve relative to the data, it is possible that the quality of the beam 2 wavenumber fit is worse than in the beam 1 analysis. This would then cause the concentration estimate to undershoot in order to minimize the misaligned residual difference between the data and simulated curve. Later results bear this out more clearly.

5.6 Concluding Remarks

Considering this data was analyzed using an identical method to that of the TDLAS data, which does not take into account the specific physical differences of FLDI, the similarity in the estimations is peculiar and raises a couple of important questions. First, is it merely coincidence that the values are reasonably close, given the ambiguity in the majority of the wavenumber range? Naturally, this requires further data collection

from A-FLDI under different circumstances, as the current data is insufficient to make a true determination. Secondly, if the results are similar because the Beer-Lambert law is genuinely applicable to FLDI data under these specific conditions, how can that inform the development of a numerical model for A-FLDI? Considering this premise, the working hypothesis from this data is that the phase differences in the stagnant air are minimal enough that the phase-coupled term of the FLDI signal model does not greatly contribute to the total intensity. This would then allow for the intensity contributions of each of the orthogonally polarized beams to be the primary contributors. Furthermore, those intensity contributions are then dependent on a baseline intensity modified by an absorption term. If the phase differences are dependent on the local density differences and are also negligible, then the molecular density differences are also negligible. This would then allow for the intensities of the two orthogonally polarized beams to be approximated as a sum using the form of the Beer-Lambert law and potentially explain why the Beer-Lambert law seems to be a decent approximation for the absorbance peak in this case. The following section describes the various tests performed to evaluate this hypothesis.

Section 6: Development and Validation of Combined FLDI and Absorption Spectroscopy Model using Tunable Diode Infrared Laser in FLDI System in Different Test Environments

To further investigate the questions presented by the open path hygrometry measurements with the small-scale A-FLDI designs, it was decided to examine two simple phase objects with A-FLDI. The first of these was an underexpanded, supersonic jet of low humidity or "dry" air emitted from a small diameter pipe. It was selected to better understand the sensitivity of the A-FLDI system to reductions in molecular density of water vapor in the vicinity of the system measurement volume. The second of these was a flame from a paraffin candle, which was chosen to study the sensitivity of the A-FLDI system to increases in molecular density of water vapor as well as to an unstable, chemically luminescent phase object.

6.1 Experimental Setup for Testing with Small Air Jet

To examine the small jet flow and investigate the signal attenuation effect for the wavelength scan, it was necessary to construct a larger FLDI system capable of accommodating the pipe and a larger degree of translation along the beam axis. To this end, the setup in **Fig. 6.1** was designed and built utilizing the same laser. The angles of the laser focusing and diverging are exaggerated in the diagram for the sake of visibility.

The total optical path for this system increased to approximately 61 cm, which fell to approximately 47.5 cm after considering the light paths through the optics. Proceeding from left to right in **Fig. 6.1**, the laser beam is emitted from the fiber optic and passes through a collimating, achromatic lens (f = 7.54 mm) within the fiber mount.

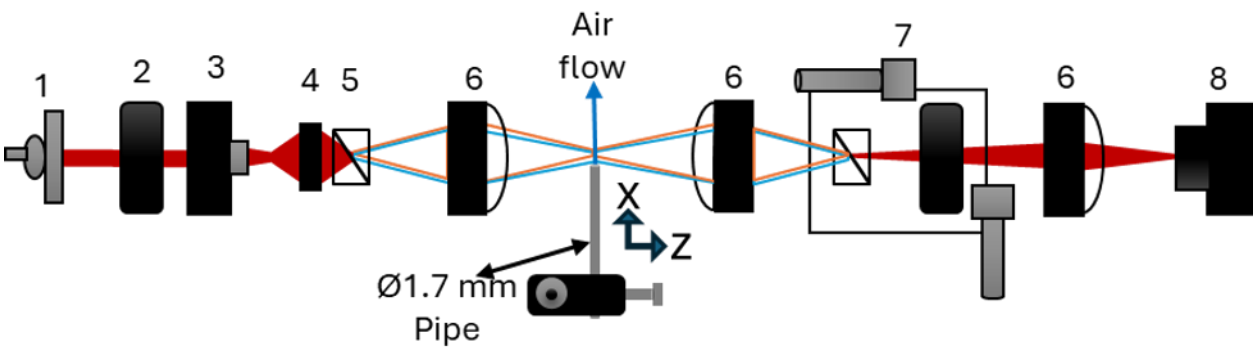

Figure 6.1. Top-down layout of 1-point A-FLDI for small jet. Components are (1) IR laser in collimating mount, (2) linear polarizer, (3) *f* = 11-mm aspheric lens, (4) *f* = 50-mm plano-convex lens, (5) Wollaston prism, (6) *f* = 60-mm plano-convex lens, (7) Wollaston prism and linear polarizer on 2-D translation stage, (8) Thorlabs PDA10CF.

The collimated beam then passes through a polarizer that linearly adjusts the beam's polarization to 45 degrees before entering an aspheric lens that focuses and then diverges the beam to the surface of a 1" diameter, plano-convex lens. This plano-convex lens focuses the beam down to the first Wollaston prism, which splits the beam in twain with a 0.067° separation angle. Both beams pass to a 2" diameter, plano-convex lens, and this produces the beam pair image with an approximate separation distance of 70 μm at 60 mm from the lens. The pipe used to produce the air jet is centered via 2D translation stage with its exit approximately 1 mm from the beam pair center as measured by calipers. The beam pair then diverges once more into an identical plano-convex lens, which focuses the beam pair into a second Wollaston prism, identical to the first.

This prism recombines the beams, and the subsequent polarizer is oriented in the same manner as the first to restore the recombined beam's polarization. The 2nd prism-polarizer pair is positioned along the beam axis such that the infinite fringe condition is achieved, and the pair is further translated perpendicular to the beam axis to achieve the necessary $\pi/2$ initial system phase shift. Finally, the recombined beam is then focused on to the tiny photodiode sensor by another 2" diameter, plano-convex lens. A full view of the assembled system is provided in **Fig. 6.2** for sense of scale. In this experiment, the laser settings matched that of the earlier 1-point A-FLDI experiment. However, different sampling rates were utilized to record measurements based on whether the signal was modulated or not. To evaluate the attenuation effect away from the system's focus and provide some basis of comparison for evaluating the system's operation with scanning wavelength, measurements were recorded using a single wavelength, namely 1392.5 nm, for various locations along the beam axis.

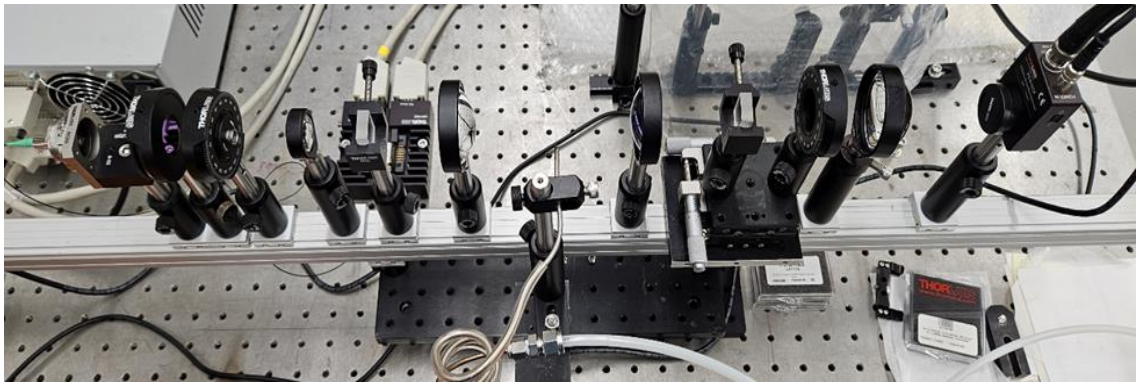

Figure 6.2. Assembled 1-point A-FLDI for small jet.

For this data, the air jet was operated from a building air supply at a pressure of approximately 105 psig and choked flow rate of 1 cfm or 28.3 L/min, and an image of the jet was obtained using a rudimentary, linear schlieren system. The A-FLDI beam pair passed through the jet within the region prior to the first Mach disk, and an image of the jet is shown in **Fig. 6.3**. Due to a slight angle in the cut of the piping for the nozzle, the jet also emits at a small angle away from the horizontal. The data was measured using a sampling rate of 2 MHz, and the resulting signals are illustrated in **Fig. 6.4**.

6.2 Results and Discussion for Testing with Small Air Jet

As expected, there is a significant attenuation of the signal for the single wavelength data as the jet is translated away from the system focus. This is in keeping with the theory of FLDI, and it also provides a means to estimate the length of the system's sensitive volume. Since this is a major benefit of FLDI, it stands to reason that the idea of scanning the wavelength for FLDI should retain this benefit to be considered an improvement. Due to the micrometer-scale focal length shift inherent to the use of N-BK7 glass lenses with a scanning wavelength length laser, it is important to attempt to verify that the system can still operate effectively under such conditions. To test this as well as the effect of using dry or extremely low humidity air on the signal, the air jet was operated via a grade D, compressed air canister set to supply air at 105 psig. There is an associated uncertainty of ±5 psig due to the analog regulator gauge that was used.

A sampling rate of 200 MHz was used to clearly visualize the modulated, triangular waveforms with associated absorption troughs, and the resulting time-series data at different locations along the beam axis is shown in **Fig. 6.5**.

Figure 6.3. Schlieren image of underexpanded, free air jet with shock diamond structures.

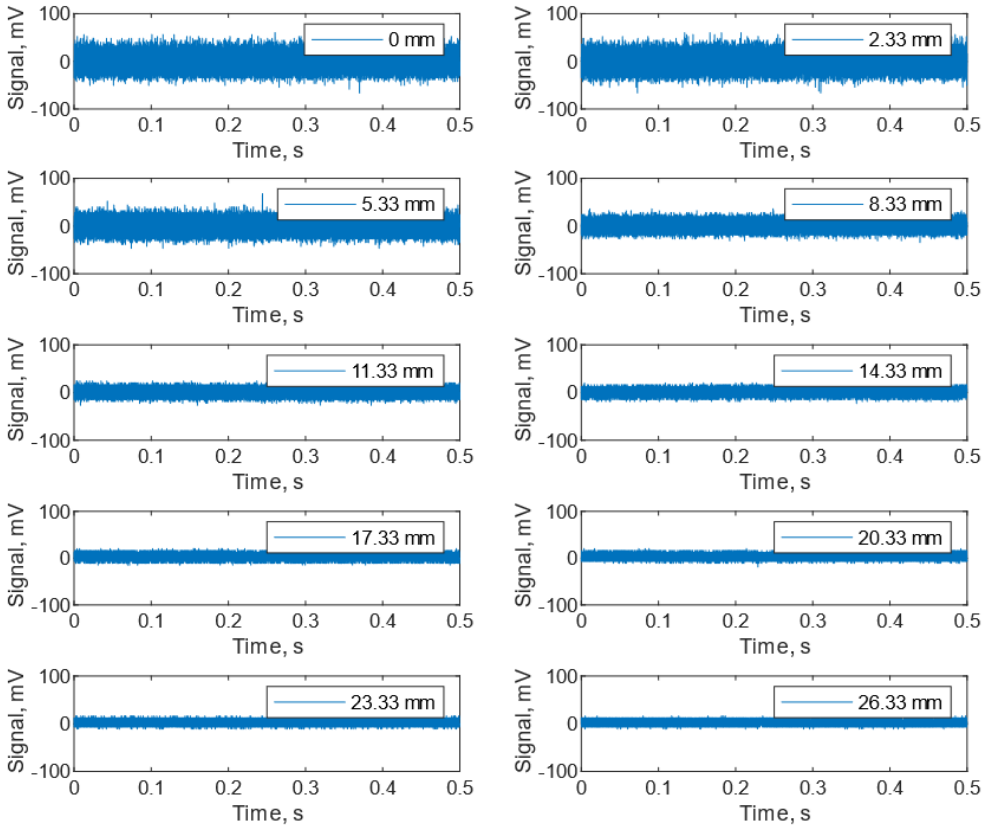

Figure 6.4. Small diameter, air jet signals over time at various displacements along the beam axis from the focal plane.

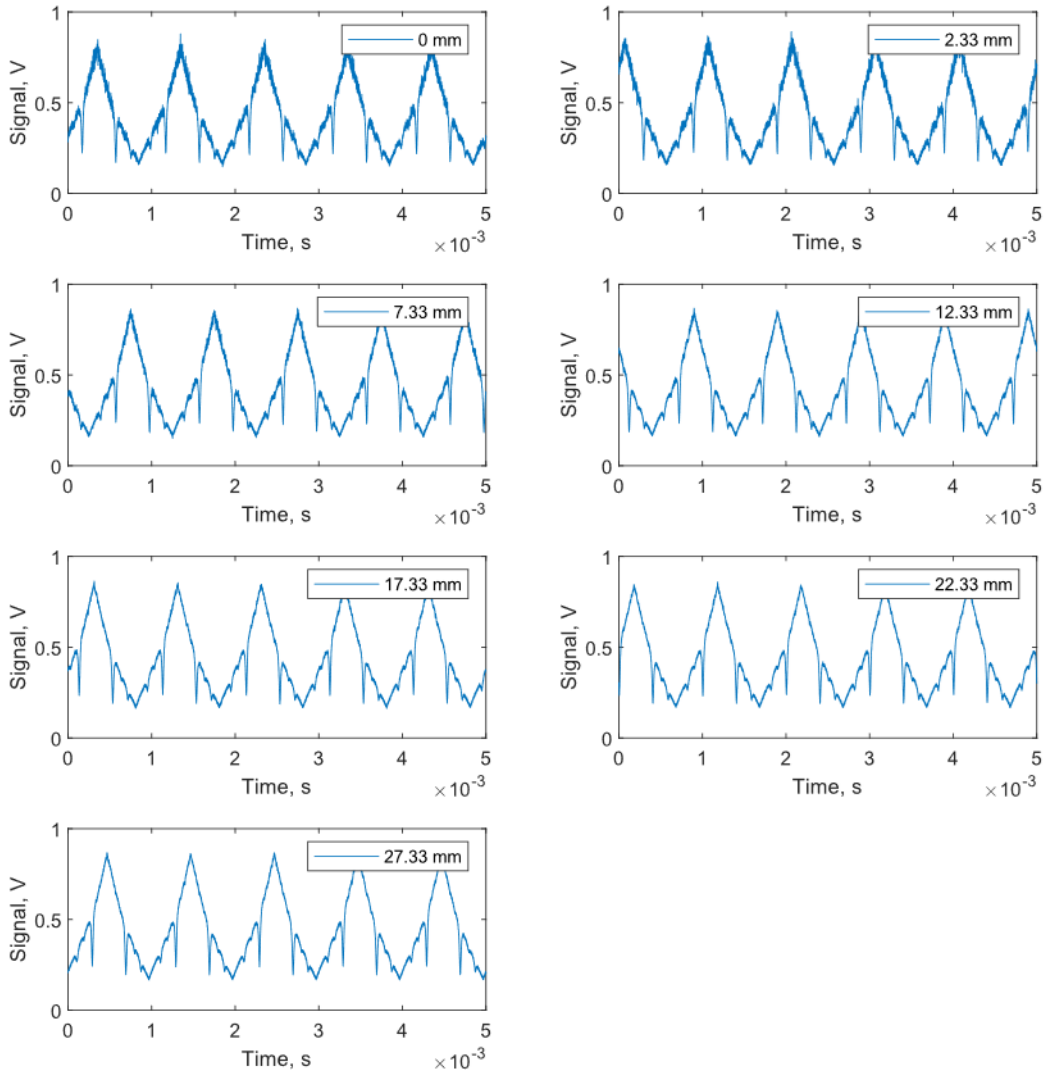

Figure 6.5. Small diameter, air jet signals over time with modulation at various displacements along the beam axis from the focal plane.

Fortunately, the triangular waveform data shows a similar attenuation effect to that of the single wavelength data, and, in contrast to the small-scale A-FLDI waveform presented earlier, these new waveforms allow for the clear identification of the 3 prominent and 2 relatively weak absorption troughs observed in the earlier TDLAS data. The more conspicuous troughs may very well be a result of the slightly increased optical path length or another aspect of this A-FLDI system's design, such as the smaller beam pair separation distance. Further experimentation will assist in making a firm assertion of the cause. However, it is instructive to first examine the power spectral density results of these two sets of data. The spectra for the 1392.5 nm case are shown in **Fig. 6.6** along with an example of the background spectrum, meaning without flow, to better understand which frequencies significantly differ from the noise. To reiterate from the theory section, the spectra are normalized by the quotient of each signal's frequency spacing and variance, which allows for comparison between data sets.

The 1392.5 nm spectra indicate that the jet flow exhibits a single, dominant frequency at approximately 83-84 kHz for the operating conditions at all displacements. Other peaks tend to coincide with the background signal and are therefore considered noise. The greatest change between displacements appears to be the slope heading into the higher frequencies. Evidently, the power spectral density rolls off much sooner at displacements farther away from the focal plane. A similar trend appears for the scanning wavelength spectra portrayed in **Fig. 6.7**. Since these spectra were recorded at a significantly higher sampling rate, there is a lack of resolution at lower frequencies that makes it difficult to ascertain whether the triangular waveforms registered the 83-84 kHz peak.

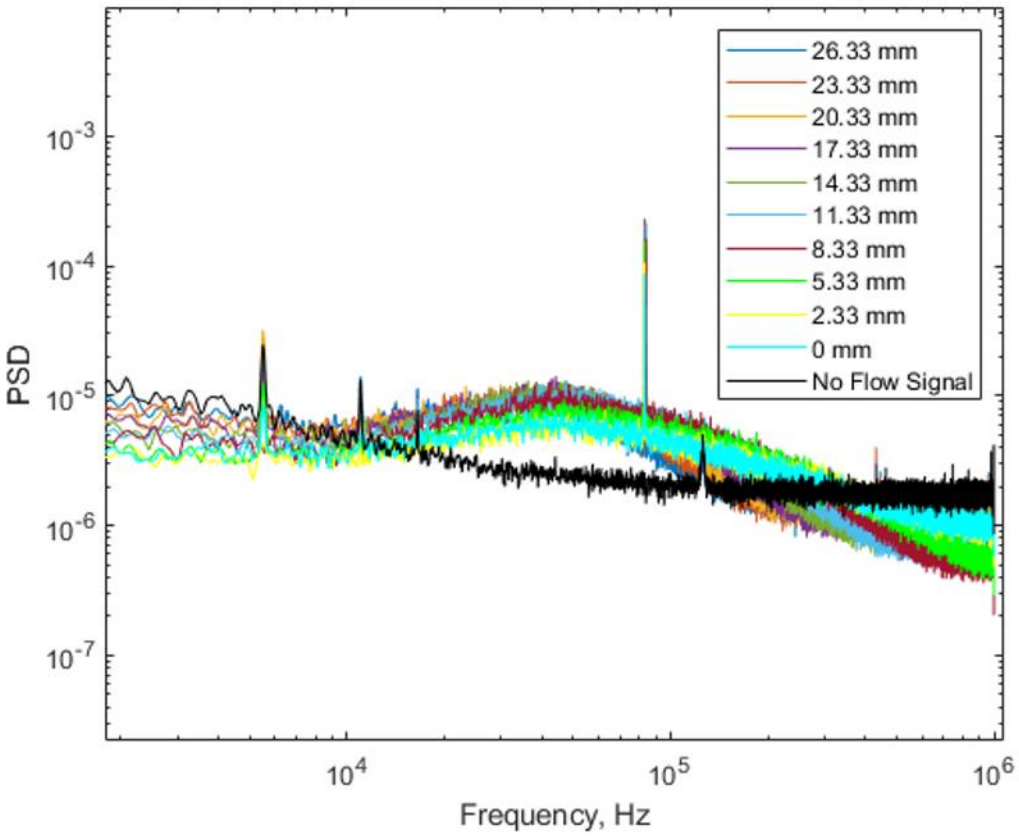

Figure 6.6. Power spectral density as a function of constituent frequencies in air jet flow at different displacements from the A-FLDI focal plane for 1392.5 nm beam.

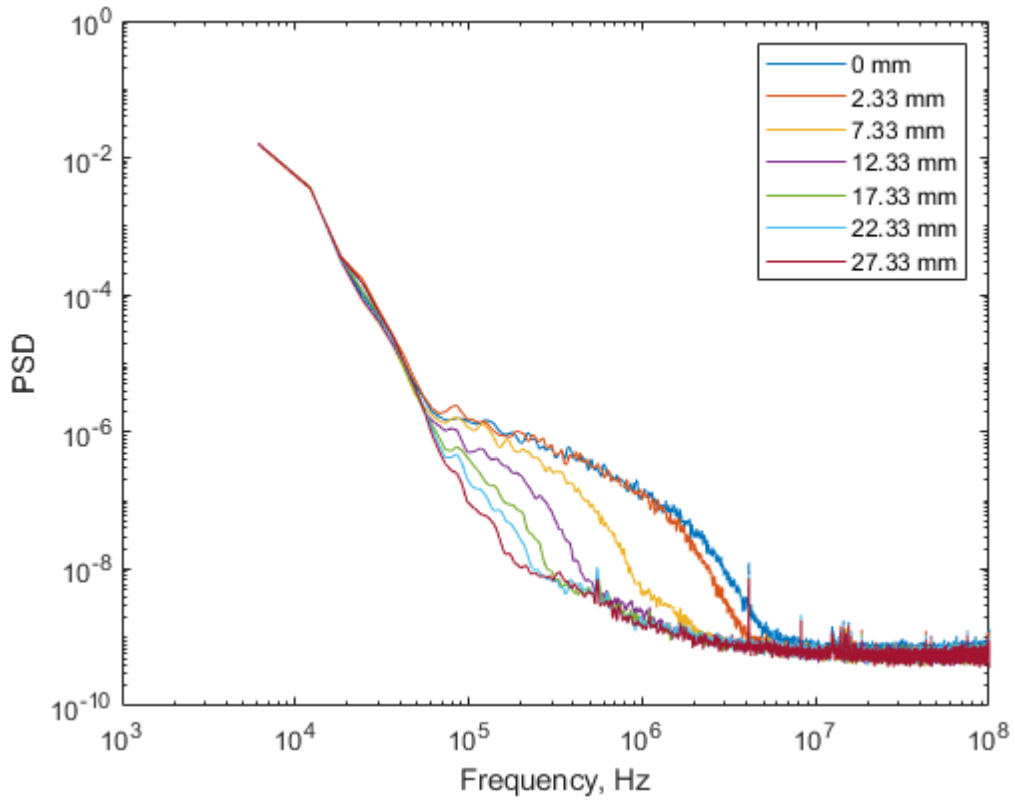

Figure 6.7. Power spectral density as a function of constituent frequencies in air jet flow at different displacements from the A-FLDI focal plane for triangular waveforms.

However, the attenuation effect is readily apparent, which gives some indication that the A-FLDI system, when scanning the wavelength range, operates in a similar manner to 1-point FLDI. This prompted the decision to reduce the modulation frequency of the current from 1 kHz to 20 Hz to allow for the usage of reduced sampling rates nearer to the 1-5 MHz range. This was suspected to allow better direct comparisons with existing FLDI data. To assess the theory that the A-FLDI design allows for estimates of water concentration, which are less influenced by path integration and more localized due to the observed signal attenuation effect, it was decided to compute the initial and final absorbance curves for the 0 mm position. During these tests, the hygrometer readings provided a range between approximately 3.02E+17 and 3.86E+17 cm^{-3} for the test's surrounding environment. The initial absorbance curve is shown in **Fig. 6.8**.

As expected from the signal data, the absorbance curve does contain some oscillations due to phase changes in the sensitive region, but the most prominent absorbance peaks are still quite visible. However, this initial model curve undershoots the data and is notably shifted away from the center of the 7183.0 cm^{-1} peak. Through manual iteration of the input temperature and pressure, as well as through automated iteration of the concentration, the final absorbance curve is obtained and illustrated in **Fig. 6.9**. Compared to the initial model curve, these results show significantly closer agreement with the measured data but continue to possess a noticeable shift away from the center of the 7183.0 cm^{-1} peak. This shift does not seem very dependent on any of the iterated inputs, so it may be indicative of a flaw in representing the A-FLDI results via the Beer-Lambert law. Put simply, it may lend itself to the idea that the necessary model for A-FLDI is a combination of the Beer-Lambert law and some modifying terms.

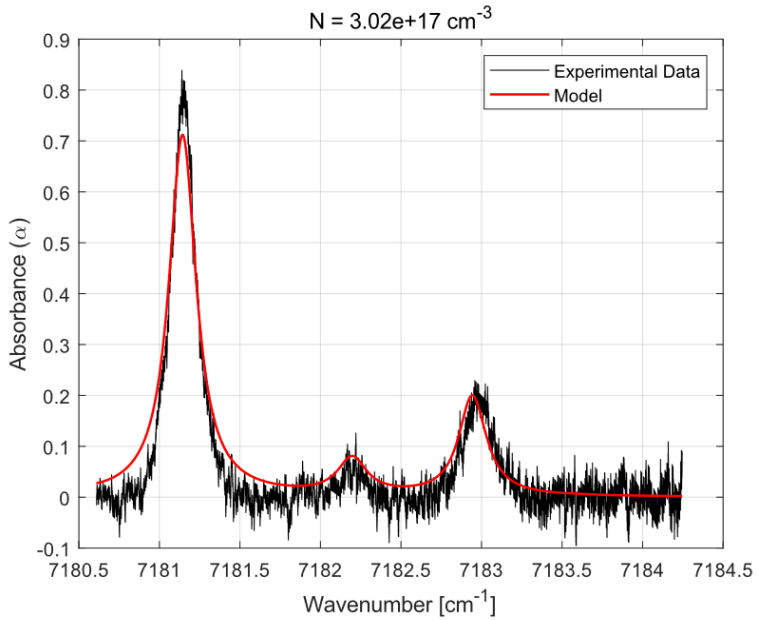

Figure 6.8. A-FLDI measured and initially simulated absorbance as a function of wavenumber for H_2O in small diameter, air jet.

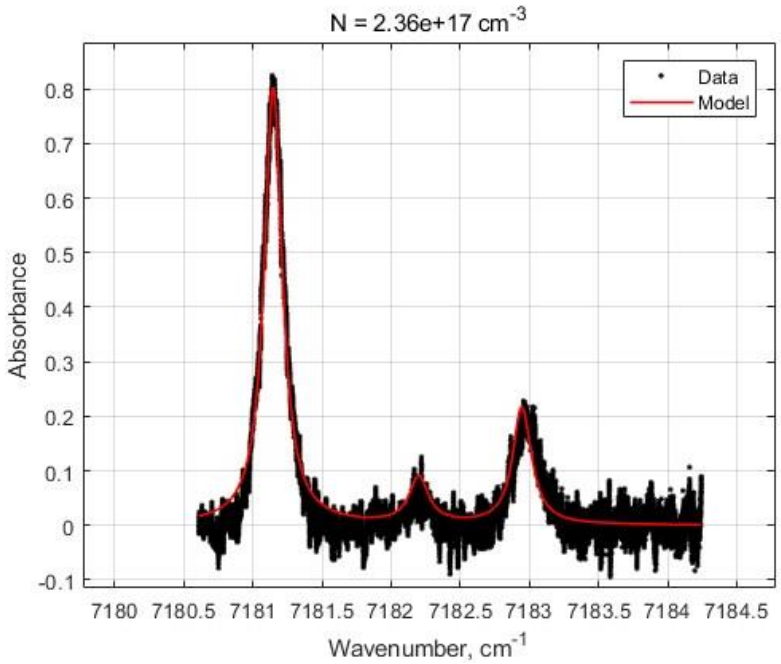

Figure 6.9. A-FLDI measured and simulated absorbance as a function of wavenumber for H_2O in small diameter, air jet.

Evaluating the final values of the inputs gives some credence to the idea that the A-FLDI signal is influenced more heavily by pressure, temperature, and water concentration changes localized to its sensitive region, which is smaller than the total path length. Compared to the concentration range of 3.02E+17 to 3.86E+17 cm^{-3} that is expected for the room's ambient air conditions, the model's estimated value of water concentration is significantly less at 2.36E+17 cm^{-3}. When one considers that the water concentration of the "dry" air from the canister is nearly negligible at approximately 0.23% relative humidity, this suggests that the A-FLDI system's path-integrated estimate is heavily influenced by the tiny segment of the total path that contains the jet [88]. Furthermore, to achieve close agreement between the model and data, the pressure and temperature were iteratively decreased to values of 0.67 atm and 260 K, respectively. This is also consistent with the idea that the much lower pressure and lower temperature region represented by the jet significantly influences the result, which indicates the potential for extracting more localized measurements of these quantities with an appropriate model. These insights were then applied to planning and conducting the A-FLDI tests with the paraffin candle.

6.3 Experimental Setup for Testing with Paraffin Candle Emissions

Unlike with the small diameter jet of air, the flame and associated products of the paraffin candle possessed an unknown water concentration, so the analysis of the data was primarily focused on its effects on the A-FLDI signal's shape and how the numerical model for FLDI must be altered to more accurately describe the signal's behavior in the presence of significantly absorbing media. Fortunately, the design of the A-FLDI system

for these tests needed no material changes beyond swapping the candle flame for the air jet, as shown in **Fig. 6.10**.

For these tests, the candle wick was located approximately 3 cm below the focal region, and the flame was approximately 1 cm beneath the focal region of the system. The water vapor from the combustion process would then rise through the plume into the focal region. Due to the location of the flame below the beam axis, the visible light of the flame was propagated through the optics to a point above the photodiode sensor area, which suggests that the effect on the signal from the chemiluminescence was minimal. For these tests, four flow measurements of the A-FLDI signal response were recorded in short succession with a sampling rate of 5 MHz, and a background measurement was also recorded at the same sampling rate. The laser settings remained the same, except for the modulation rate. As previously mentioned, this was lowered from 1 kHz to 20 Hz to utilize a lower sampling rate and retain a clear view of the absorption troughs of the signals. These signals are illustrated in **Fig. 6.11**.

6.4 Results and Discussion for Testing with Paraffin Candle Emissions

Compared to data from the earlier experiments, these signals show a peculiar rounding off on the peaks. Comparing Run 3 with the measured background, as in **Fig. 6.12,** indicates that the phenomenon is independent of the phase object being detected. Anecdotally speaking, subsequent experiments revealed that this is due to a slight misorientation of the photodiode with the recombined beam, and it appeared to exclusively impact the higher wavelengths. Small rotations and vertical adjustments of the photodiode were generally sufficient to restore the triangular waveform shape.

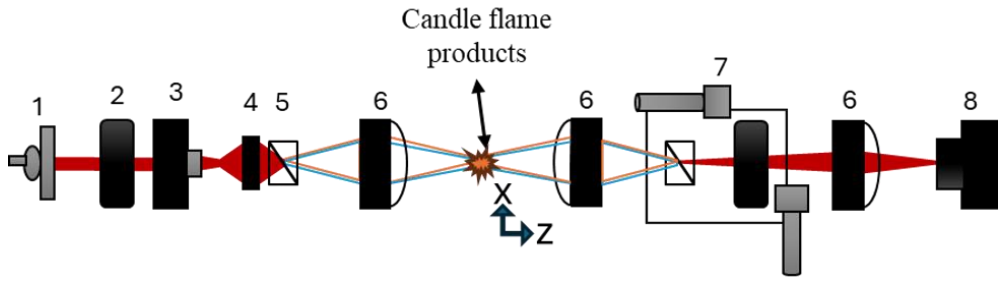

Figure 6.10. Top-down layout of A-FLDI setup with candle below focal region.

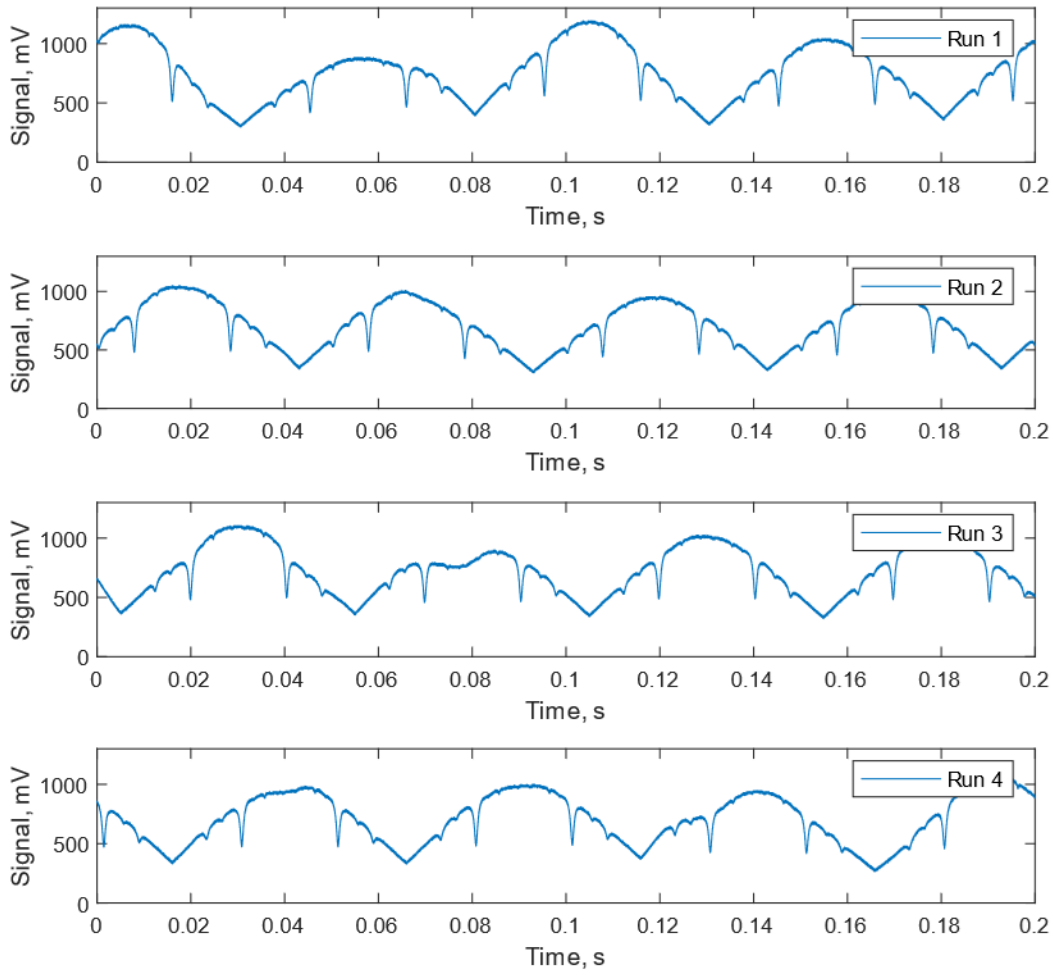

Figure 6.11. A-FLDI signal measurements of candle flame products in plume.

Both **Fig. 6.11** and **Fig. 6.12** show a repeating deformation in the plume signal compared to the background signal, which produces a significant drop in intensity near the upper portion of the wavelength scan. Although it does not occur for each upward ramp in the signals, it occurs with varying magnitude over the course of the four recorded signals. It is speculated that this is due to a low frequency feature of the candle's plume, in part because a comparison of the signal spectra in **Fig. 6.13** reveals significant similarity between the background and plume measurements at higher frequencies.

Close examination shows the greatest deviations occur in the lower frequencies between 0-20 kHz. This is further reinforced by assessing the power spectrum of run 1 with the background noise removed. The prevailing frequency information for the plume is illustrated in **Fig. 6.14**. An unfortunate effect of utilizing a relatively high sampling rate of 5 MHz to visualize the frequency scanning effect is that the frequency resolution of the power spectrum is nearly 20 kHz, and, therefore, it is not possible to discern more accurately the actual frequency of the disturbance impacting the plume. However, this does contribute some evidence that the A-FLDI achieves the detection of dominant frequencies in flow.

Ultimately, tests with the supersonic jets appear more appropriate for assessing this facet of A-FLDI. For now, it is more instructive to examine the application of the Beer-Lambert Law to the candle's plume measurements. A well-defined portion of run 2's signal is selected, and appropriate wavenumbers for the scan are fit to the data. The resulting measured absorbance curve and the final simulated curve are illustrated in **Fig. 6.15**.

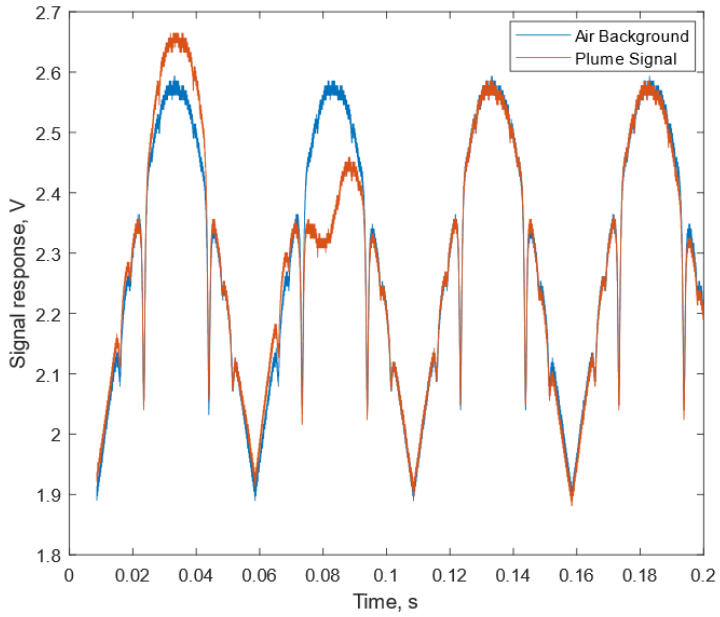

Figure 6.12. A-FLDI signal comparison of plume and background.

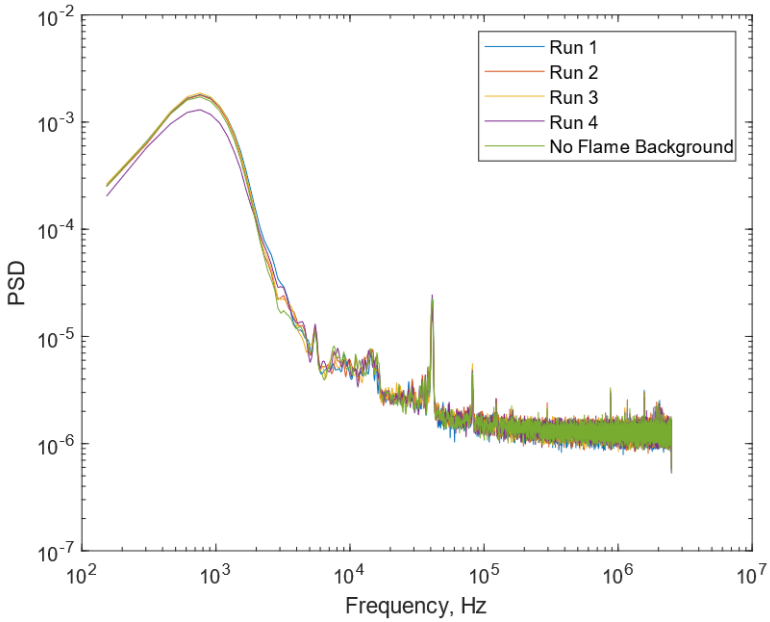

Figure 6.13. A-FLDI power spectral density as a function of constituent frequencies.

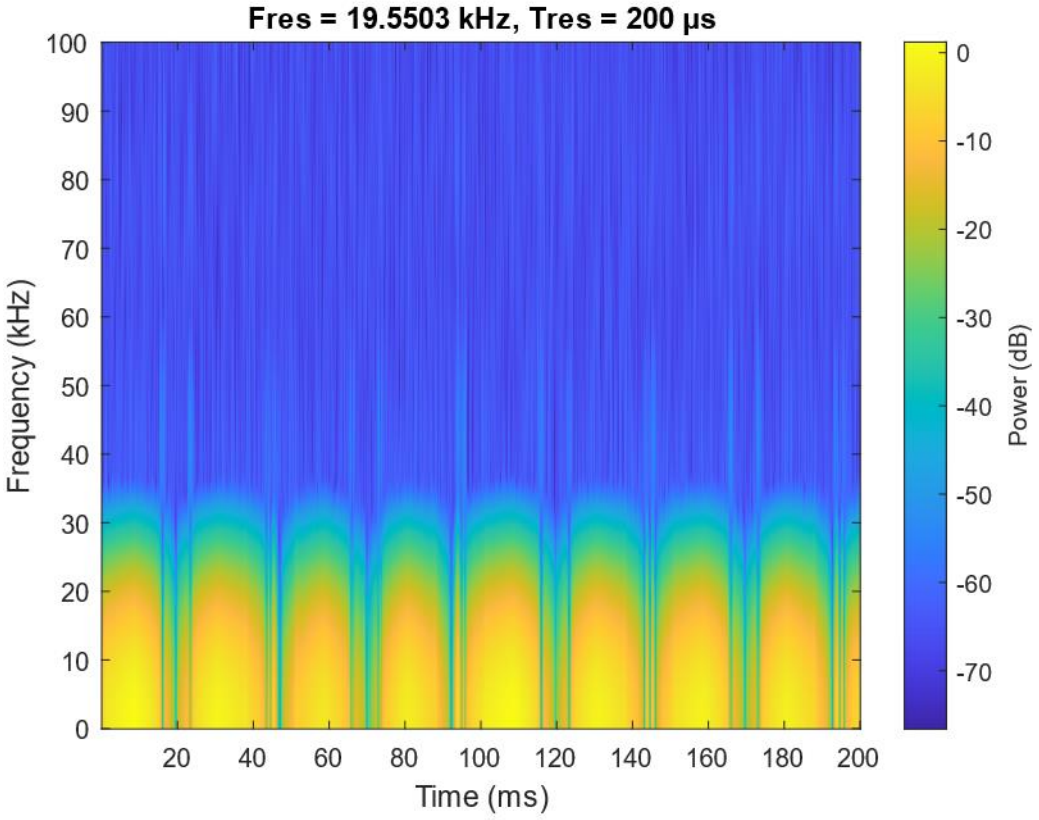

Figure 6.14. A-FLDI power spectrum of plume measurements with background frequencies removed.

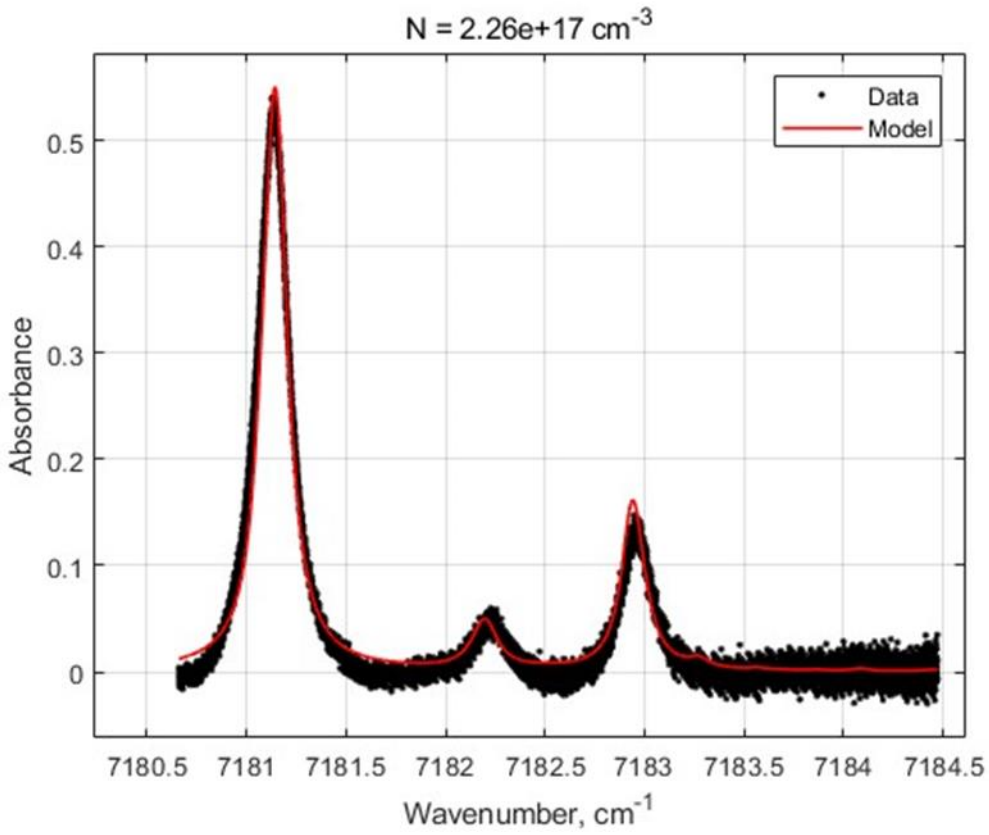

Figure 6.15. A-FLDI measured and final simulated absorbance as a function of wavenumber for H_2O in candle plume.

Given that the nature of the candle plume's structure requires a pressure approximately equal to the surroundings, only the temperature and concentration were iterated. As a result, the molecular density and temperature for the final curve approached approximate values of 2.26E+17 cm^{-3} and 500 K, respectively. However, it is evident that there is still some shift for the estimated curve away from the centers of the 7182.2 and 7183.0 cm^{-1} peaks, which again suggests the need for modification to the Beer-Lambert law and FLDI equations to better estimate these peaks. Similarly to the earlier jet data, this estimate of water vapor molecular density is significantly different from the prior values seen for the room air, and this reinforces the idea of significant sensitivity to a relatively small region of the total path length.

Given that paraffin candle flames can achieve temperatures of nearly 1700 K and plume temperatures anywhere between 400-1200 K, the estimated temperature is somewhat reasonable [89]. However, a more accurate determination should theoretically stem from considering the phase differences as well in the numerical approach. After all, for the wavenumbers where absorption is negligible, A-FLDI should operate according to the same principles as FLDI, and it is only when the wavenumbers induce significant absorption that the signal will begin to deviate from the expected behavior and thus require a new numerical model to fill in the gaps. To illustrate this concept, the phase differences for the unaffected wavenumbers were calculated and are shown in **Fig. 6.16**. The graph shows rapid oscillations between different phase shift levels for the unaffected wavenumbers and gaps in the data where the absorbance becomes significant.

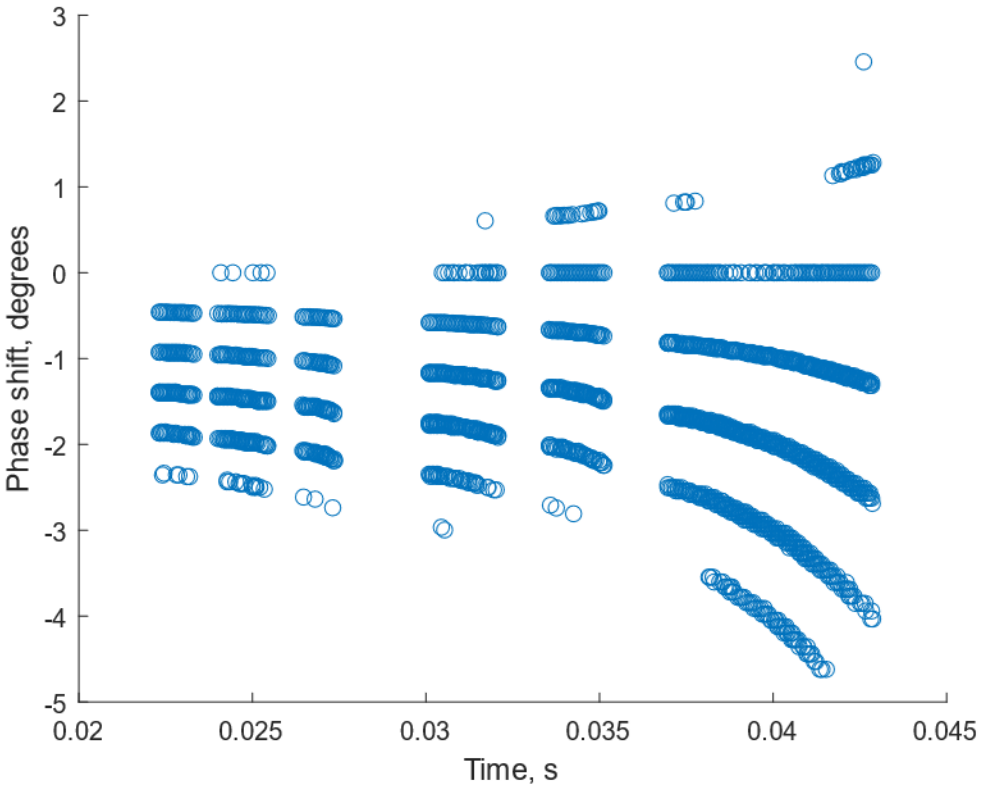

Figure 6.16. A-FLDI measured phase shift as a function of time for unaffected wavenumbers in sampled absorbance curve.

6.5 Theoretical Model from Results

To delve into this idea further, the Beer-Lambert law was merged with the earlier equation for the total FLDI signal to create a modified form that accounts for the wavelength dependency of the absorption on the intensity signals of the two orthogonally polarized beams. This relationship is given by Eq. (6.5.1).

$$I_T = I^0 e^{-N_1\sigma_1 L_1} + I^0 e^{-N_2\sigma_2 L_2} - 2I^0\sqrt{e^{-N_1\sigma_1 L_1 - N_2\sigma_2 L_2}}\sin\Delta\varphi \tag{6.5.1}$$

When expanded to encompass the full expression for the phase differences, Eq. (6.5.1) can be written in the form of Eq. (6.5.2).

$$I_T = I^0\left(e^{-N_1\sigma_1 L_1} + e^{-N_2\sigma_2 L_2} - 2\sqrt{e^{-N_1\sigma_1 L_1 - N_2\sigma_2 L_2}}\sin\left(\frac{2\pi KLM_w}{\lambda\bar{N}k_b}\left(\frac{P_1}{T_1} - \frac{P_2}{T_2}\right)\right)\right) \tag{6.5.2}$$

Considering the earlier equations for the absorption cross-section, it is clear that this new and expanded equation for the A-FLDI signal is dependent on the unknown variables of molecular density of the absorbing species, pressure, and temperature along each of the FLDI beam paths. As they are represented in Eq. (6.5.2), there is a slight disconnect in the regions to which the variables apply. In effect, the molecular densities apply to the regions defined by the total optical path lengths of the orthogonally polarized beams. However, the pressures and temperatures are written in a way where they apply to the region of each orthogonally polarized beam contained within the sensitive length of the system. The next experiment phase concerned the analysis of a Hencken burner flame using this nascent A-FLDI numerical framework. The disconnect in the flow regions covered by the phase-based component and the individual beam contributions was addressed by removing the absorbance contributions of the ambient air's water vapor. Values like the optical path lengths and sensitive length are still estimated however, and

the quality of those estimates will of course influence the results, which will form an important aspect of the uncertainty analysis. The remaining quantities are effectively constants depending on the stage of the flow chemistry when the measurements are recorded.

Recalling the ability of TDLAS to obtain temperature measurements via dual-line thermometry, one is inclined to wonder if a similar method may be applied here to determine the temperature to refine the concentration estimate. If we consider the new form of the A-FLDI signal, it bears obvious similarity to the Beer-Lambert law, but, clearly, there is no easy way to isolate the absorbances by applying the natural logarithm. As a result, a ratio of absorbances that leads to a ratio solely of the line strengths is not possible. Therefore, a more complicated, iterative approach to determining the two temperature variables is required. To achieve this, the model must be validated, and an appropriate data reduction approach needs to be developed.

6.6 Experimental Setup 1 for Testing with Hencken Burner Flame

To further explore A-FLDI, it was deemed necessary to examine a flow region with better understood characteristics. To this end, a Hencken burner flame was recognized as being especially suitable, specifically for its stable and predictable water vapor concentration and overall temperature profiles. Hencken burners are widely utilized for research in a calibration capacity, precisely because of their predictable behavior and ability to produce near-adiabatic flames. Hencken burners are designed with numerous, small flow channels to allow significant mixing of the fuel and oxidizer before reaching the flame. As a result of their unique design, these burners produce “flat” flames, which possess nearly uniform characteristics except near their edges, and the

burner used here produces a laminar flow as well. With knowledge of the supplied fuel and oxidizer, Hencken burner flames can be carefully controlled to achieve specific equivalence ratios that correspond to repeatable temperature, pressure, and concentration measurements [90-94].

Two designs of the A-FLDI system were utilized to examine the Hencken burner flame in question. Both possessed larger optical path lengths than previous experiments due to a need to accommodate the bulky Hencken burner. The first of these designs incorporated two photodiodes to measure both the A-FLDI signal and the signal response of the A-FLDI beam pair before being brought to interfere. This measurement of the uncombined pair signal was effectively like a focused version of TDLAS, and it was recorded to provide more information about the behavior of the beam pair signals for use in the numerical model. The specifics of this will be expanded upon shortly. The second of the A-FLDI designs incorporated a 3rd photodiode to allow both of the A-FLDI beam signals to be measured individually before being brought to interfere on the main signal path. This was done to provide even more information of the individual beam signals and allow for improved analysis of the underlying physics.

The 2-photodiode A-FLDI design, which can be conceptualized as akin to a co-linear combination of A-FLDI and pseudo-TDLAS, is shown in **Fig. 6.17**. As with previous setups, this one was designed and built utilizing the same IR laser. The angles of the laser focusing and diverging are exaggerated in the diagram for the sake of visibility. The total optical path for this system increased to approximately 112 cm for the main optical path and 78 cm for a side optical path, but, after accounting for the paths lengths through the optics, this reduced to approximately 99.3 cm and 71.5 cm, respectively.

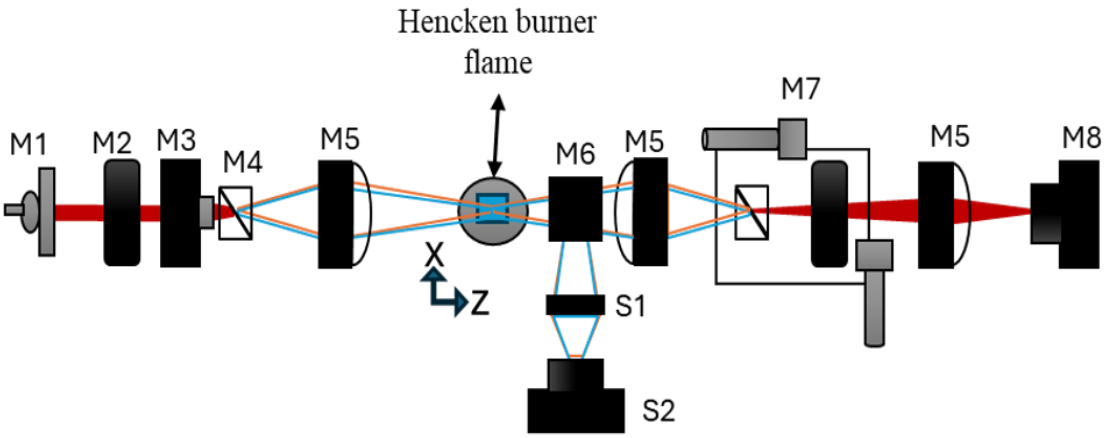

Figure 6.17. Top-down layout of 1-point A-FLDI setup with offshoot measurement path for examining Hencken burner flame. Components are (M1) IR laser in collimating mount, (M2) linear polarizer, (M3) f = 11-mm aspheric lens, (M4) Wollaston prism, (M5) f = 60-mm plano-convex lens, (M6) 50:50 beamsplitter, (M7) Wollaston prism and linear polarizer on 2-D translation stage, (M8) Thorlabs PDA10CF, (S1) f = 50-mm plano-convex lens, (S2) Thorlabs PDA05CF2.

In this setup, the 50-mm focal length lens is shifted outside of the main optical path to a side path, and the aspheric lens is moved to focus the laser into the first Wollaston prism. This was done to increase the divergence of the laser entering the lens just before the measurement volume. As earlier researchers have noted, increasing the divergence into the focusing lens before the measurement volume enhances FLDI system sensitivity [21].

The burner was positioned such that the A-FLDI beam pair propagates through the flat flame front, approximately 2.42 mm above the burner's surface, and focuses at the flame's center with approximately 37 μm separation distance as before. The burner area is a square approximately 2.5 cm on a side. Half of each beam's intensity is split off before the next focusing lens and sent perpendicular to the original optical path. These split-off beams enter a lens, which then focuses the beams into a photodiode. The combined signal of these beams is detected by that photodiode, which may entail some interference between the individual signals. The later 3-photodiode setup assists in addressing this potential source of ambiguity. The remaining intensity-halved beams proceed through the A-FLDI system as normal. A view of the assembled system is shown in **Fig. 6.18** for context.

The Hencken burner flame was produced by combustion of methane with air, and the mixture utilized in this experiment was provided by combining methane at 0.5 L/min with air at 4 L/min. This yielded an equivalence ratio of approximately 1.19 and a steady uniform flame. Attempts were made to lower the equivalence ratio to unity by adjusting the flow rates, but the flame would consistently snuff out upon doing so. Three measurements of the flame were recorded with the system at a 5 MHz sampling rate.

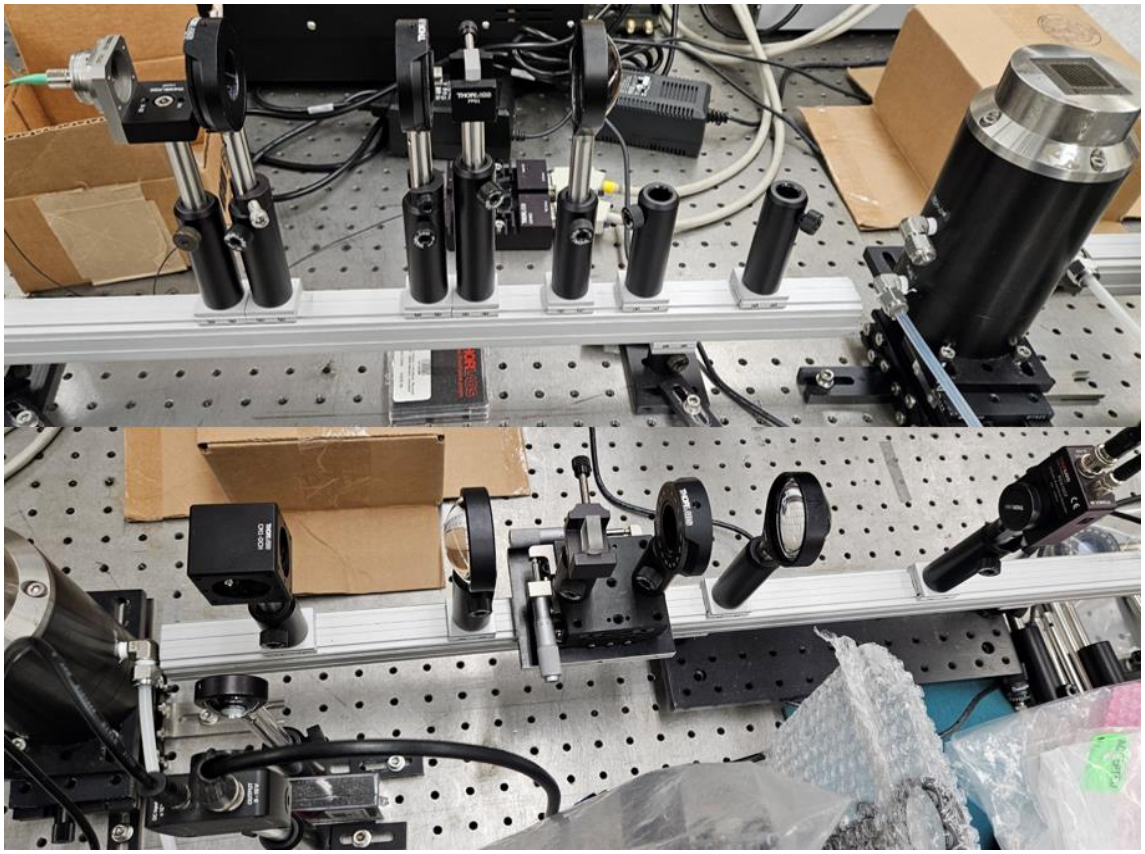

Figure 6.18. Assembled 1-point A-FLDI and colinear, 1-path TDLAS for examining Hencken burner flame.

A background waveform was also measured at the same sampling rate for both the main and side optical paths. These represented the main A-FLDI signal and pseudo-TDLAS signal, respectively.

6.7 Theory of Operation

Using the notion that the flame signals share highly similar optical paths and are affected by largely unchanged water vapor concentrations outside of the flame compared to the background measurements, a background removed representation of Eq. (6.5.1) can be developed. This relationship is expressed in Eq. (6.7.1), and it shows how the signal may be separated into two primary components, the in-flame and background parts. It utilizes the assumption that the differences in the A-FLDI signal for the flame measurements compared to the background are overwhelmingly the result of the flame itself, and, therefore, any changes to environmental conditions away from the flame remain negligible.

$$I_T = I^0 e^{-N_{Intbgd}\sigma_{Intbgd}(L_{Intbgd}-L_{flame})} \times \left(e^{-N_1\sigma_1 L_{flame}} + e^{-N_2\sigma_2 L_{flame}} - 2\sqrt{e^{-N_1\sigma_1 L_{flame}-N_2\sigma_2 L_{flame}}}\sin\Delta\varphi\right) \quad (6.7.1)$$

Furthermore, this lends itself to an additional assumption in which the sensitive length of the A-FLDI system is largely encompassed by the flame. Since the phase differences across the beam pair in FLDI are directly dependent on the local density changes, it stands to reason that the measured phase differences from A-FLDI are directly dependent on the changing pressure and temperature across the beam pair over the sensitive length affected by the phase object. For this experiment, Eq. (6.7.2) shows the relationship between the phase shift, pressure, temperature, and sensitive length.

$$\Delta\varphi = \frac{2\pi K L_{flame} M_w}{\lambda \bar{N} k_b}\left(\frac{P_1}{T_1} - \frac{P_2}{T_2}\right) \tag{6.7.2}$$

Quantities like the Gladstone-Dale constant and molecular weight are dependent on the equivalence ratio and present species, which are considered controlled inputs in this case. Equivalence ratio in a methane-air combustion may be defined through the ratio of the fuel and oxidizer volumetric flow rates as described by Eq. (6.7.3) [95].

$$\phi = 9.52\left(\frac{Q_{CH_4}}{Q_{air}}\right) \tag{6.7.3}$$

Furthermore, the global equation for balancing the combustion process as a function of equivalence ratio can be represented by Eq. (6.7.4), if one assumes that the reaction results almost entirely in leftover fuel and primary combustion products [95].

$$C_1H_4O_0 + \frac{1}{\phi}\left(1 + \frac{4}{4} - \frac{0}{2}\right)(O_2 + 3.76N_2) \rightarrow$$
$$\left(\frac{1}{\phi}\right)C_1O_2 + \frac{4}{(2 * \phi)}H_2O_1 + \frac{3.76}{\phi}\left(1 + \frac{4}{4} - \frac{0}{2}\right)N_2 + \left(1 - \frac{1}{\phi}\right)C_1H_4O_0 \tag{6.7.4}$$

The rationale for the use of the beamsplitter lies in its ability to help isolate the signals of the beam pair before they are brought to interfere and recombine. The total signal of the beam pair could then potentially be represented by Eq. (6.7.5), which shows how the signal is also a combination of an in-flame and background portion.

$$I_{BS} = I^0 e^{-N_{BSbgd}\sigma_{BSbgd}(L_{BSbgd} - L_{flame})}(e^{-N_1\sigma_1 L_{flame}} + e^{-N_2\sigma_2 L_{flame}}) \tag{6.7.5}$$

Through the rearrangement of this equation, one can obtain a relationship between the sum of the absorbance terms, as shown in Eq. (6.7.6).

$$\frac{I_{BS}}{I^0 e^{-N_{BSbgd}\sigma_{BSbgd}(L_{BSbgd} - L_{flame})}} = (e^{-N_1\sigma_1 L_{flame}} + e^{-N_2\sigma_2 L_{flame}}) \tag{6.7.6}$$

This could then be substituted into Eq. (6.7.1) to yield a somewhat simplified form, given by Eq. (6.7.7).

$$\frac{I_T}{I^0 e^{-N_{Intbgd}\sigma_{Intbgd}(L_{Intbgd}-L_{flame})}} - \frac{I_{BS}}{I^0 e^{-N_{BSbgd}\sigma_{BSbgd}(L_{BSbgd}-L_{flame})}} = \left(-2\sqrt{e^{-N_1\sigma_1 L_{flame}-N_2\sigma_2 L_{flame}}}\sin\frac{2\pi K L_{flame} M_w}{\lambda \bar{N} k_b}\left(\frac{P_1}{T_1}-\frac{P_2}{T_2}\right)\right) \quad (6.7.7)$$

To begin assessing this model, the measured signals for the flame and background were compared in **Fig. 6.19** and **Fig. 6.20**.

6.8 Results and Discussion for 2-photodiode Hencken Burner Flame Tests

Upon examining the flame and background signals for the main path of the interferometer, it is clear that the flame signal experiences a significant uniform drop in intensity. This uniform drop in intensity may indicate that the flame optical density is nontrivial. Furthermore, analysis of the side path signals indicates a similar behavior. The noninterference path's signals do display significantly reduced oscillations relative to the interference signals, which one might expect to have more phase shift-induced oscillations. In addition, there are no indications of highly disruptive, low-frequency behavior as seen with the candle tests. Although, there does appear to be some variation in the lower frequencies, based on the power spectral density results in **Fig. 6.21**. Since the data does not contain any significant irregularities, it seems reasonable to proceed to isolating individual wavelength scans for analysis. The background signals selected for the analysis are shown in **Fig. 6.22**.

Direct comparison of the background signals reveals that the system is sensitive enough to detect the five main absorbing wavelengths in the room temperature air. Although, the weakest absorbance features are less visible in the interference signal.

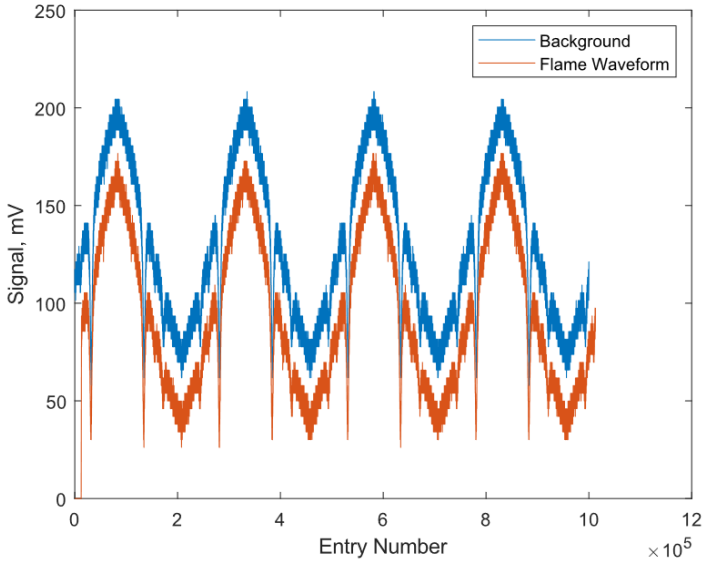

Figure 6.19. Aligned comparison of interference path's Hencken burner flame signal and background.

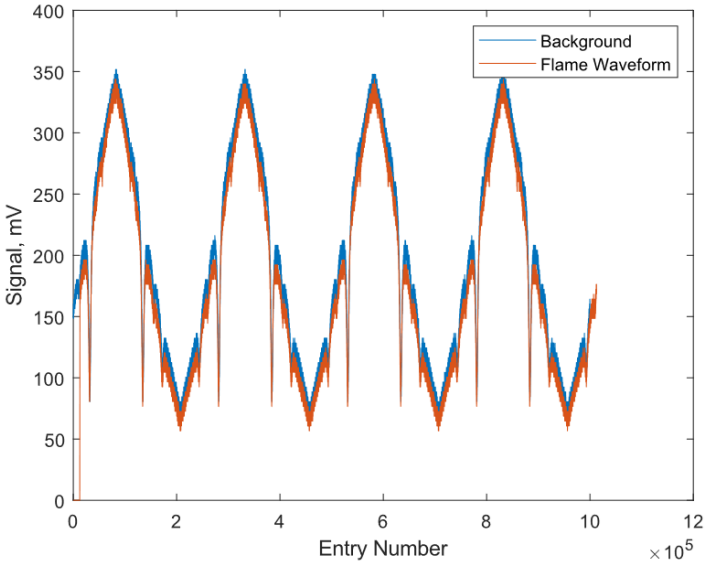

Figure 6.20. Aligned comparison of noninterference path's Hencken burner flame signal and background.

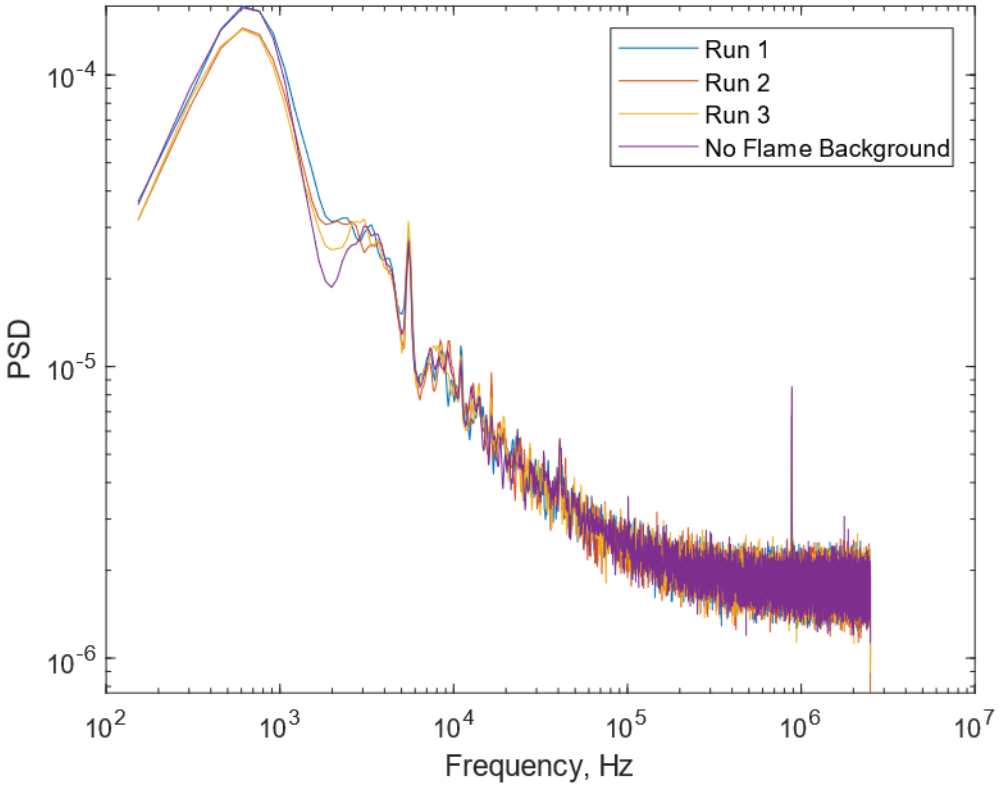

Figure 6.21. Comparison of power spectral density as function of constituent frequencies in Hencken burner flame using A-FLDI with triangular waveforms.

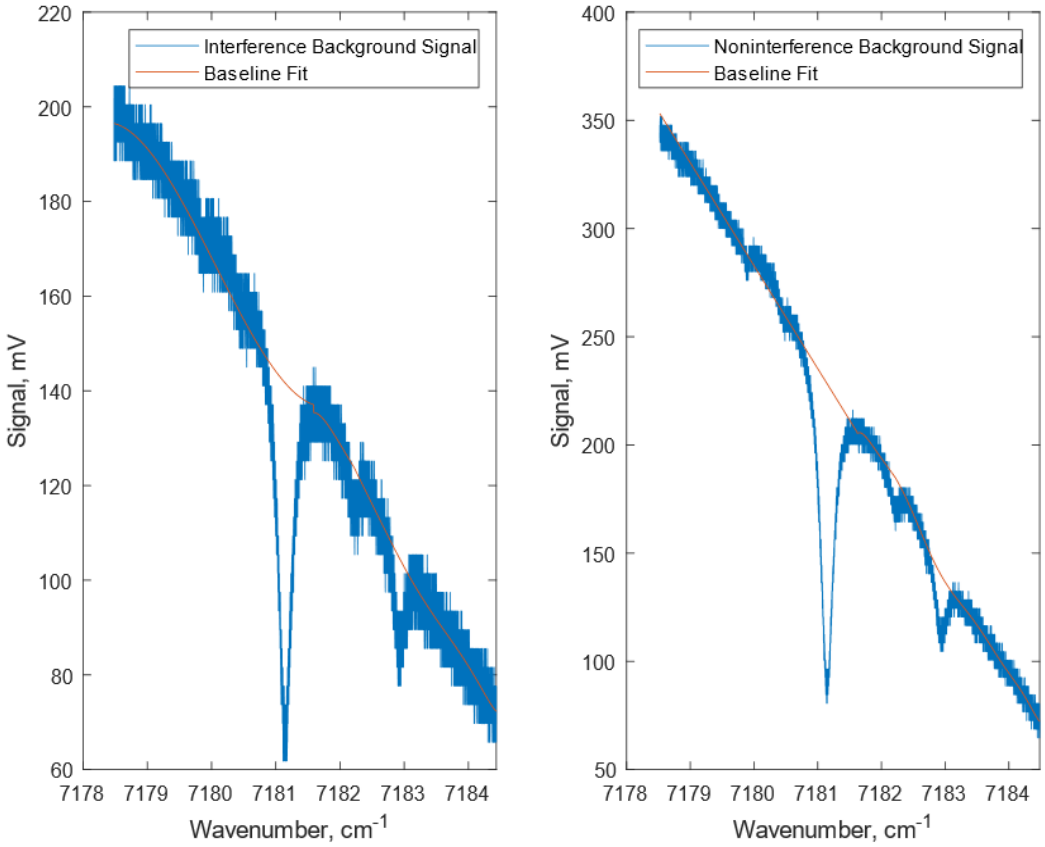

Figure 6.22. A-FLDI background signals with baseline curve fits.

This appears to be due to the greater relative signal oscillations. Fortunately, after applying the Beer-Lambert law, the absorbance curves show the peaks a bit more clearly. The background absorbance from the main path of the interferometer is shown in **Fig. 6.23**.

The agreement at the three more prominent peaks is quite strong, and the two less prominent peaks on the left of the graph show comparable magnitudes to the simulated ones. However, they appear to be shifted to the right of the simulated quantities. Given the similarity of the more intense peaks, this shift may simply be a product of the relative insensitivity at the smaller wavenumbers of the scan. Furthermore, the molecular density estimate of 1.902E+17 cm^{-3} from above falls toward the low end of the hygrometer measurement range of 1.90E+17 to 2.50E+17 cm^{-3} for the time of testing. By comparison, the absorbance curve for the noninterference path is of generally higher magnitude than the interference signal's. This is shown in **Fig. 6.24**.

Notably, the simulated curve undershoots the most prominent peak and retains the wavenumber shift for the two smaller peaks. However, the curve still closely follows the peaks at 7182.2 cm^{-1} and 7182.9 cm^{-1}. It is unclear whether the undershooting of the main peak is related to both beams being measured on the same photodiode. It does suggest that the concentration estimate may be too low for this data, which would then potentially put it outside of the hygrometer range. Bearing this in mind, the next step in implementing the proposed model for A-FLDI was to take these background estimates of absorbance and use Eq. (6.7.6) with the measured flame data to compute the unitless signal ratio for the A-FLDI side path. The first of these is illustrated by **Fig. 6.25.**

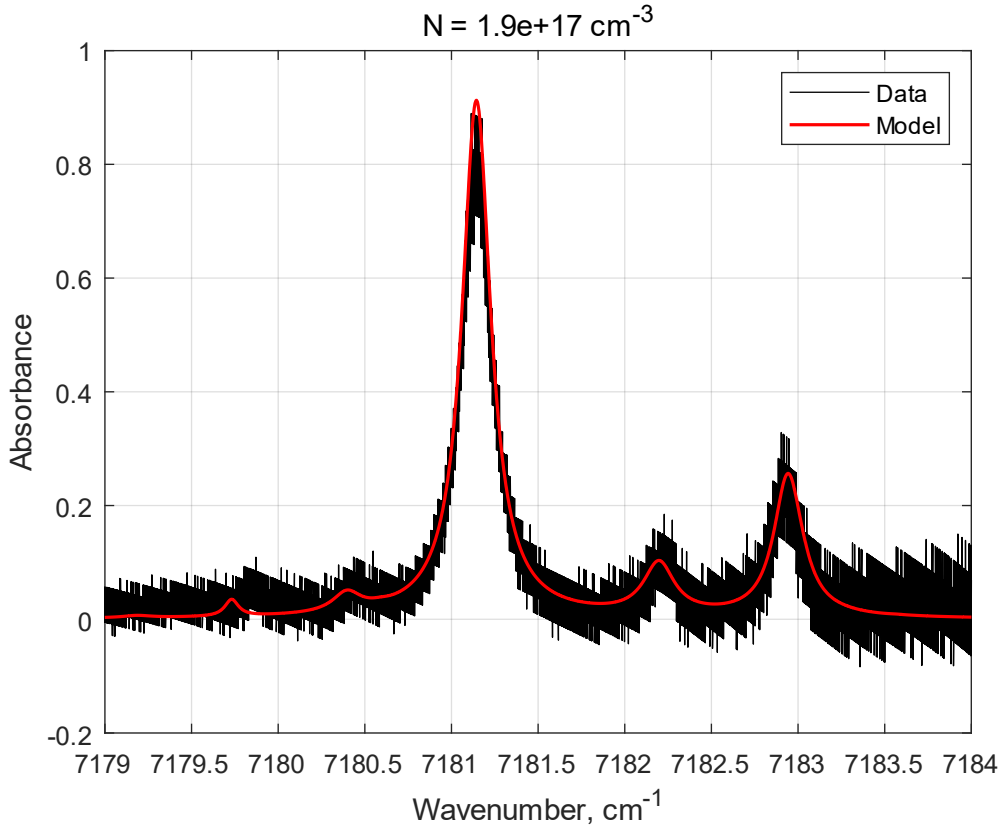

Figure 6.23. A-FLDI interference path's measured and simulated absorbance as a function of wavenumber for no flow case.

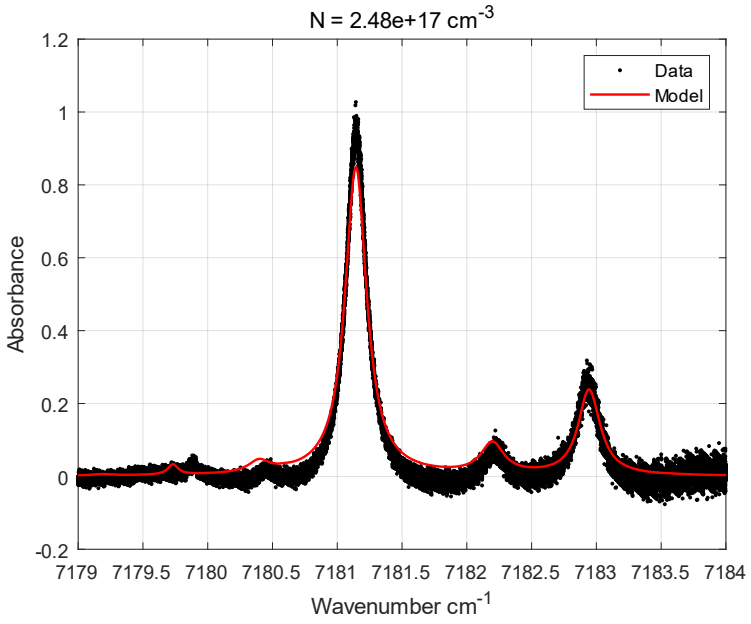

Figure 6.24. A-FLDI noninterference path's measured and simulated absorbance as a function of wavenumber for no flow case.

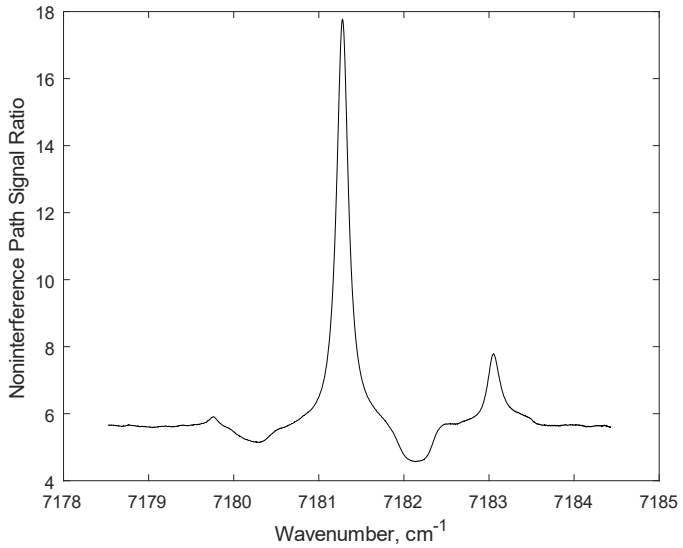

Figure 6.25. Ratio of measured flame signal over non-flame background for noninterference path as a function of wavenumber.

The graph of the signal ratio effectively serves as a stand-in for the absorbance curve that would normally be calculated, as it is completely dependent on the sum of the absorbance exponential terms in Eq. (6.7.6). One would then expect absorbance features corresponding to the flame to be present. However, it is clear that the only peaks being detected are already present in the background data. For the given equivalence ratio and Hencken burner design, the adiabatic flame temperature for these measurements is indicated in **Fig. 6.26** to be approximately 2200 K [93]. Compared to an example absorption plot from HITRAN via Spectraplot.com, there should be major peaks in the low end of the wavenumber scanning range. This example is given in **Fig. 6.27**.

The lack of many of these peaks suggests that the noninterference signal is either not detecting the absorbance information of the flame, or the model itself is not suitable. To improve on this, the clearest approach is to modify the system to add a 3rd photodiode to allow measuring each beam individually and conduct a similar set of measurements. Furthermore, it was decided to measure slightly above the visible flat flame front to ensure that more water vapor would propagate through the probe region and that the laser would be less affected by the visible flame, which could potentially be optically thick [96].

6.9 Experimental Setup 2 for Testing with Hencken Burner Flame

This A-FLDI design is shown in **Fig. 6.28**. As with previous setups, this one was designed and built utilizing the same IR laser. The angles of the laser focusing and diverging are again exaggerated in the diagram for the sake of visibility. The main optical path for this system remains unchanged from the 2-photodiode setup with the exception of the Wollaston prisms.

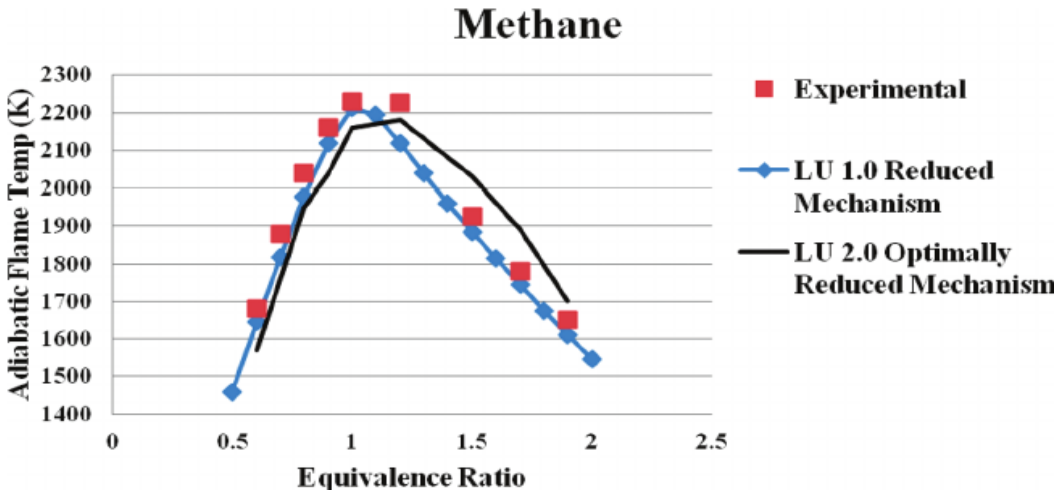

Figure 6.26. Methane and air adiabatic flame temperature as a function of equivalence ratio determined via empirical and rigorous skeleton mechanism optimization.

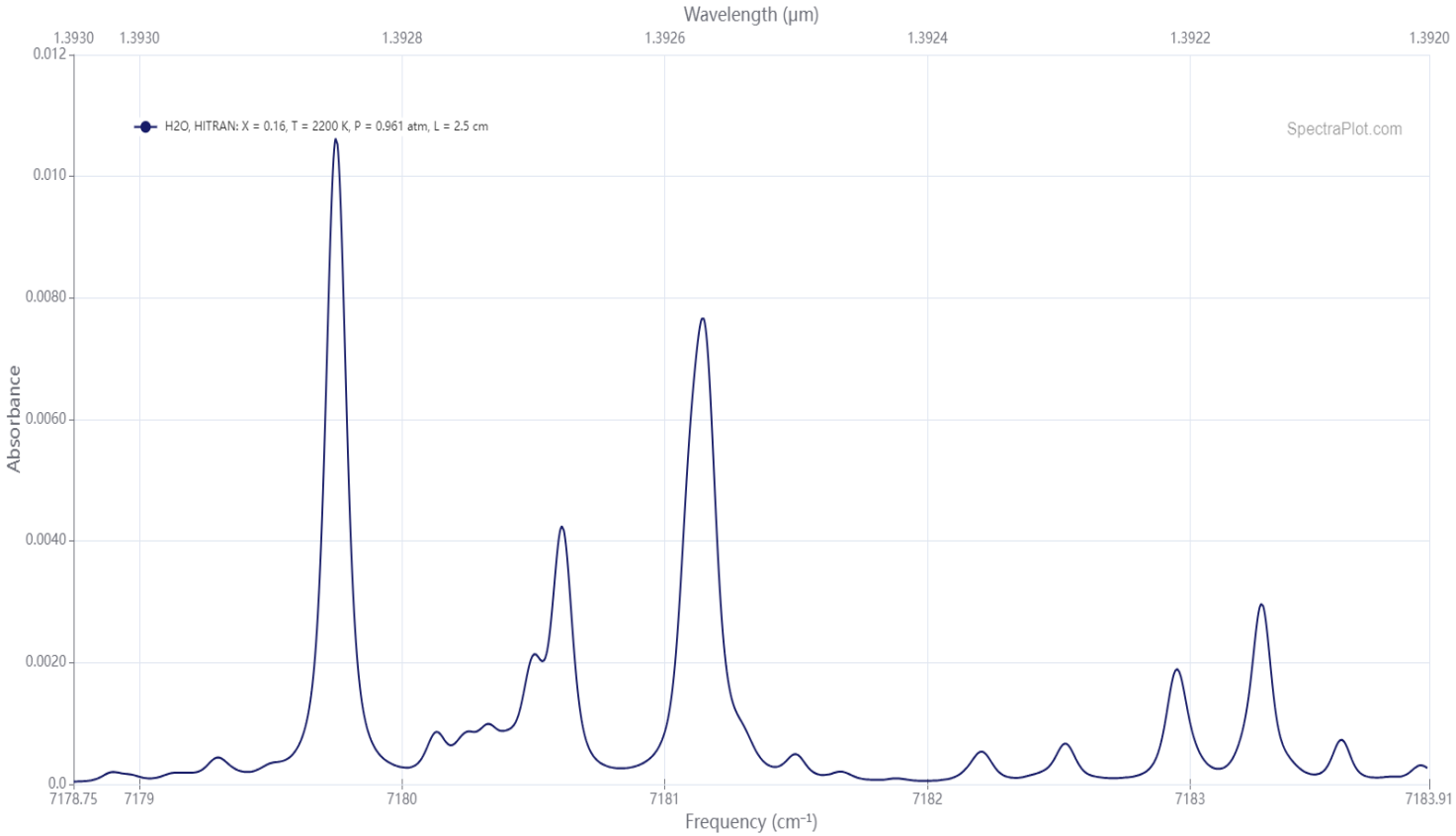

Figure 6.27. Simulated absorbance curve for H_2O via HITRAN and SpectraPlot.

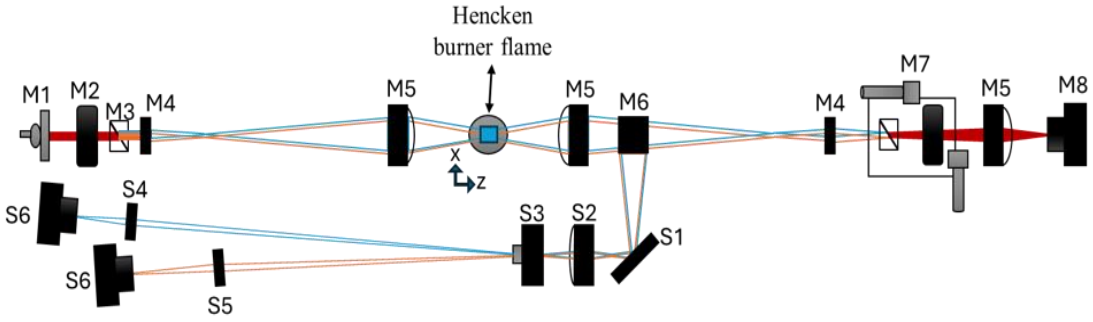

Figure 6.28. Top-down layout of 1-point A-FLDI setup and colinear, 2-path TDLAS for examining Hencken burner flame. Components are (M1) IR laser in collimating mount, (M2) linear polarizer, (M3) Wollaston prism, (M4) *f* = 11-mm aspheric lens, (M5) *f* = 60-mm plano-convex lens, (M6) 50:50 beamsplitter, (M7) Wollaston prism and linear polarizer on 2-D translation stage, (M8) Thorlabs PDA10CF, (S1) Protected aluminum mirror, (S2) *f* = 100-mm plano-convex lens, (S3) *f* = 11-mm aspheric lens, (S4) *f* = 50-mm plano-convex lens, (S5) *f* = 75-mm plano-convex lens, (S6) Thorlabs PDA05CF2.

To improve the ease with which the individual beams could be diverged to different photodiodes in the side paths, new Wollaston prisms were installed, which possessed separation angles of 1 degree instead of the previous 0.067-degree variants. The burner was lowered such that the A-FLDI beam pair propagates approximately 0.58 ± 0.01 mm above the flat flame and focuses at the flame's center with approximately 180 μm separation distance. Half of each beam's intensity is split off before the next focusing lens and sent perpendicular to the original optical path. These split-off beams are redirected by a mirror into a plano-convex lens and then aspheric lens, which together focus and diverge the beams from one another along the axis of their separation. Each beam then enters a different lens and is directed to a corresponding photodiode. The remaining intensity-halved beams proceed through the A-FLDI system as normal. A view of the assembled system is shown in **Fig. 6.29** for context.

The Hencken burner flame was again produced by combustion of methane with air, and the mixture utilized in this experiment was provided by combining methane at 0.48 L/min with air at 2.8 L/min. The different flow rates were necessary to maintain the steady flame. This yielded an equivalence ratio of approximately 1.632, which corresponds to an adiabatic flame temperature averaging approximately 1850 K between the three techniques described by Lou et al. [93]. Three measurements of the flame were recorded with the system at a 5 MHz sampling rate, and a background waveform was also measured at the same sampling rate for both the main and side optical paths. These represented the main A-FLDI signal and pseudo-TDLAS signals, respectively.

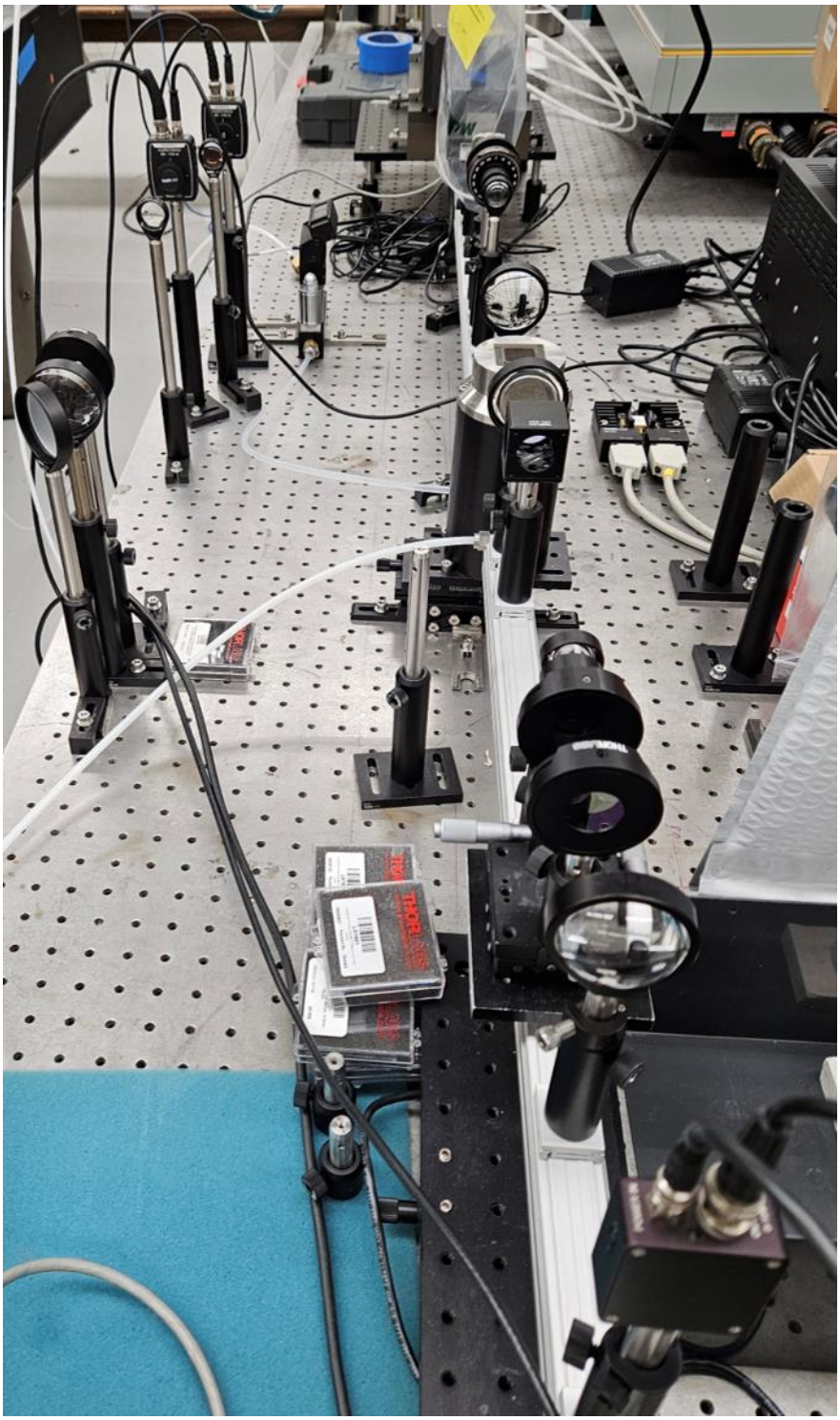

Figure 6.29. Assembled 1-point A-FLDI and colinear, 2-path TDLAS for examining Hencken burner flame.

6.10 Results and Discussion for 3-photodiode Hencken Burner Flame Tests

As with the 2-photodiode data, individual wavenumber scans were isolated, baselines were fit, and background absorbances were determined. The model in Eq. (6.7.6) was then applied for each of the individual A-FLDI beams recorded in the side path. The resulting absorbance curves for the beams are shown in **Fig. 6.30** and **Fig 6.31**. Examining these absorbance curves reveals that the prominent peaks are all present within the background absorbance curves observed previously in the 2-photodiode data. These results show that the proposed model is not adequate to capture the information from the flame. Therefore, a different approach needed to be taken. Evaluating the system design suggests that the flame absorbance data must be found in the difference between the background and sample data, since the signals would otherwise be identical. It stands to reason that background subtraction is then necessary. In the process of applying this idea, it was recognized that the backgrounds first needed to be corrected to the level of the flame signals in order to account for thermal drift in the photodiode signals over the course of testing. The extent of this thermal drift can be visualized in the difference between the signals shown by **Fig. 6.32** and **Fig. 6.33**. The signal curves exhibit improved detection of the weaker absorbance features, leading to all five being easily visible. Proceeding to the removal of the background and similarly adjusting the baselines reveals new signals with a fraction of the original magnitude.

These new signals are illustrated in **Fig. 6.34** and **Fig. 6.35**. For the sake of understanding the structure of the data sets, they are smoothed by a 500-point moving average. These signals no longer follow the slope of the original triangle waveform but retain some of the oscillatory behavior.

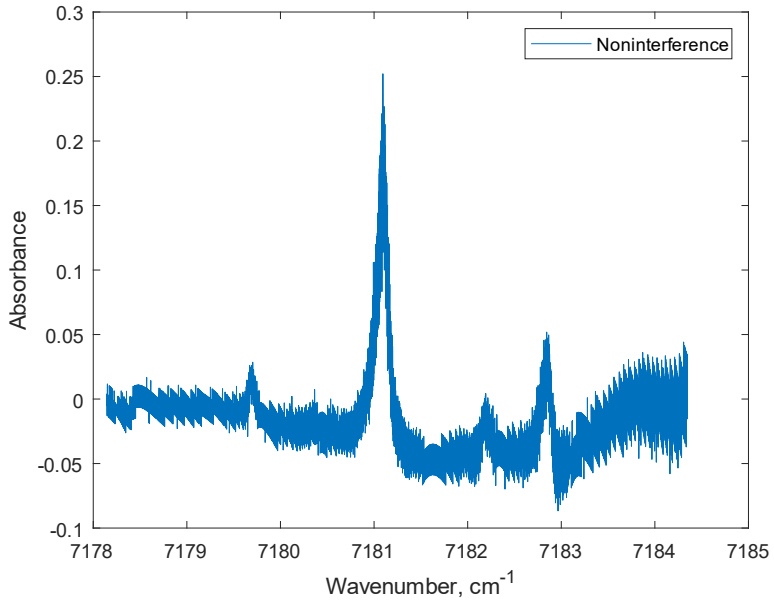

Figure 6.30. Absorbance as a function of wavenumber for first A-FLDI beam using proposed model.

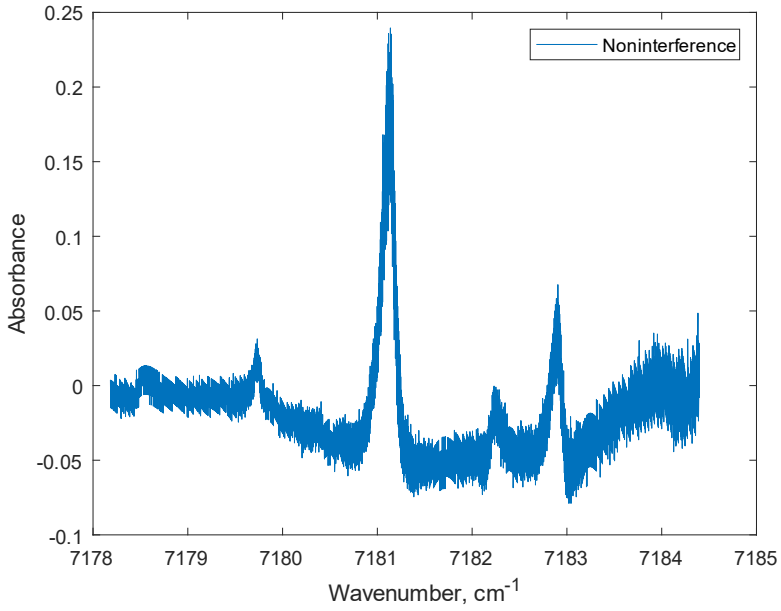

Figure 6.31. Absorbance as a function of wavenumber for second A-FLDI beam using proposed model.

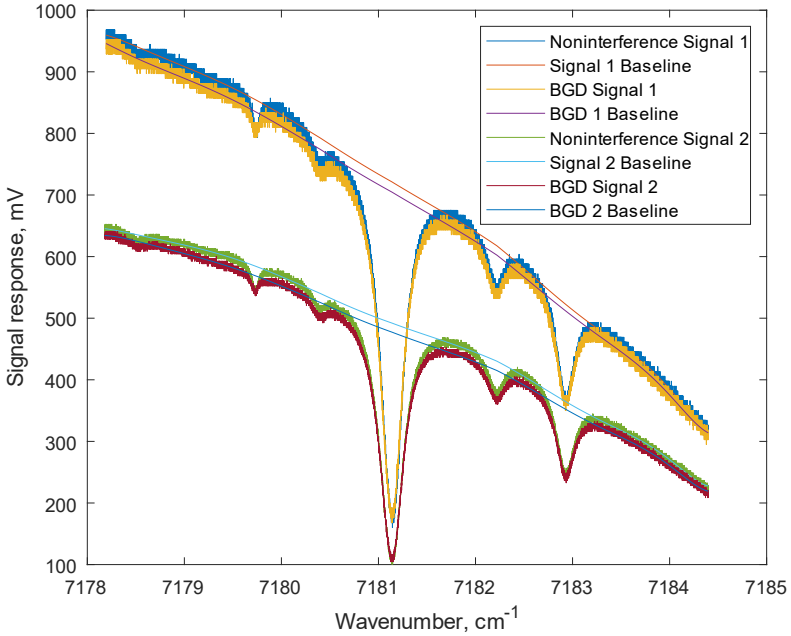

Figure 6.32. Comparison of noninterference flame signals and backgrounds with corresponding baseline fits.

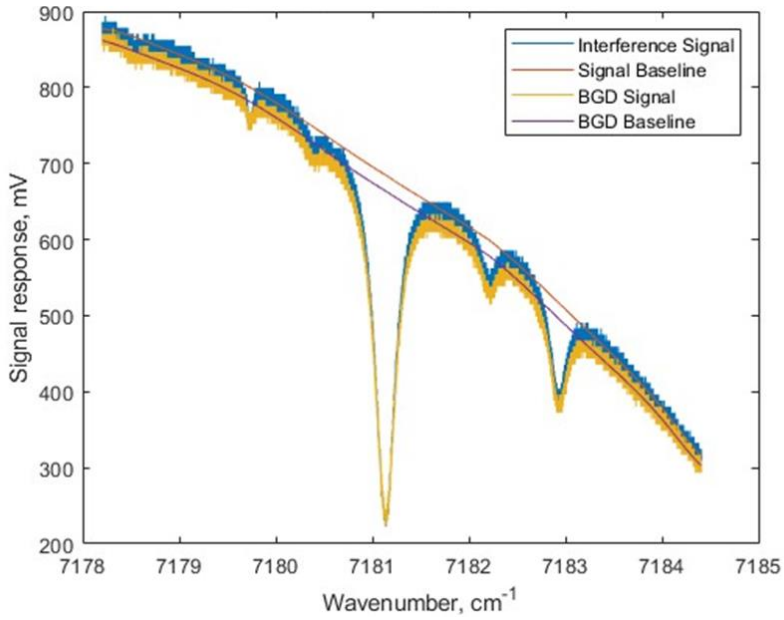

Figure 6.33. Comparison of interference flame signal and background with corresponding baseline fits.

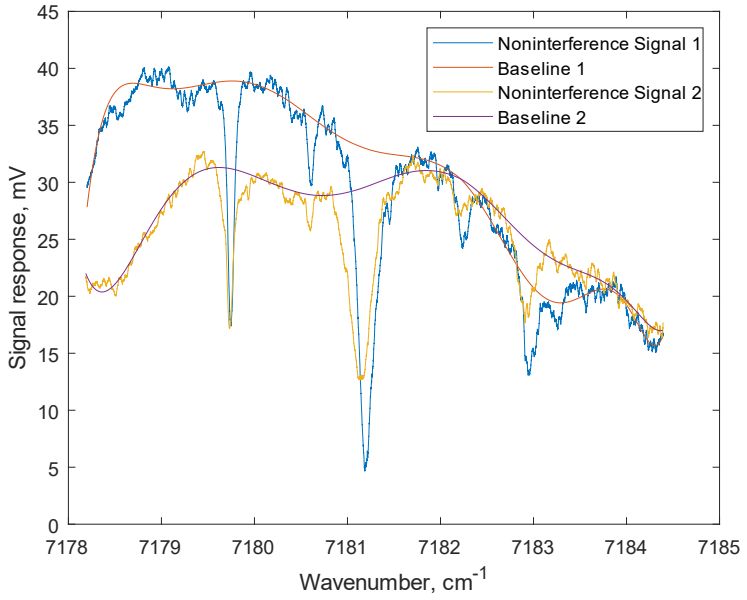

Figure 6.34. Noninterference signals and baselines from methane-air flame after background removal.

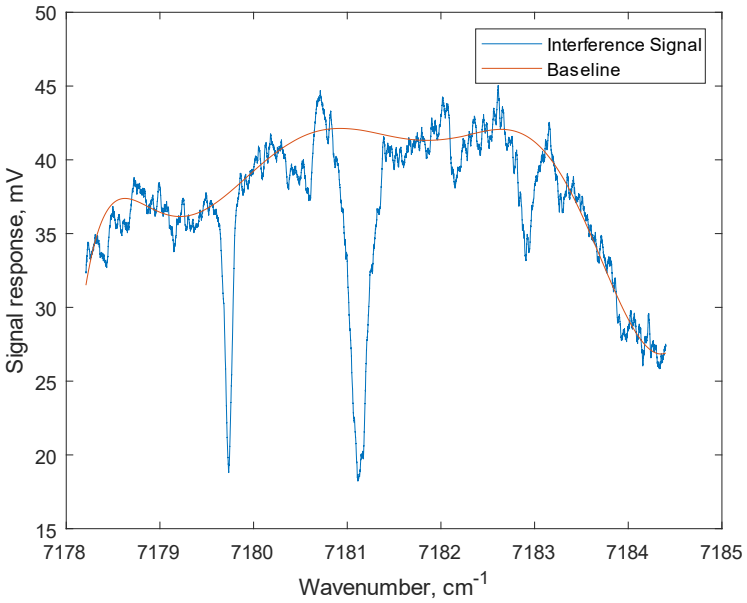

Figure 6.35. Interference signal and baseline from methane-air flame after background removal.

The clearest difference appears to be the presence of new troughs in the curves, which stand out prominently relative to the baselines. The prominent troughs of the data suggest the presence of significant laser energy absorption at different wavenumbers relative to the background. To obtain corresponding absorbance curves, a modified form of the Beer-Lambert law given by Eq. (6.10.1) is used.

$$-\ln\left[\frac{I_n - I_{n_{BGD}} + \left(I_{0_n} - I_{0_{n_{BGD}}}\right)}{2\left(I_{0_n} - I_{0_{n_{BGD}}}\right)}\right] = \alpha_{flame} \qquad (6.10.1)$$

The equation represents how a beam's signal, I_n, has its background, $I_{n_{BGD}}$, removed after correcting by the difference between their baselines, I_{0_n} and $I_{0_{n_{BGD}}}$. By then dividing by the new baseline of the curve, which is approximately double the baseline difference, the appropriate signal ratio is obtained for computing the absorbance via the natural logarithm. The absorbance curves for the noninterference signals are illustrated in **Fig. 6.36** and **Fig. 6.37**. The arrangement of their prominent peaks and the corresponding wavenumbers bears encouraging similarity to the previously shown simulated absorbance curve for the flame at an approximate temperature near 2200 K.

However, the relative heights of the peaks suggest that the absorbances reflect a lower overall temperature. Considering the flame temperature for the 3-photodiode experiments is approximately 1800 K, this is to be expected. Yet, if 1800 K is used to simulate the measured absorbance curves, the relative strengths of the simulated absorbance peaks differ notably from the data.

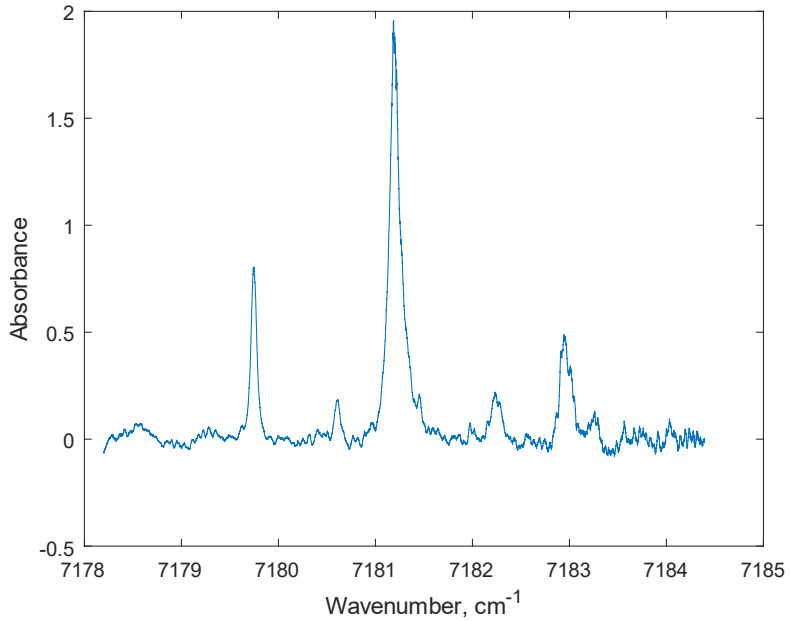

Figure 6.36. Absorbance curve for first beam of noninterference path through Hencken burner flame after background removal.

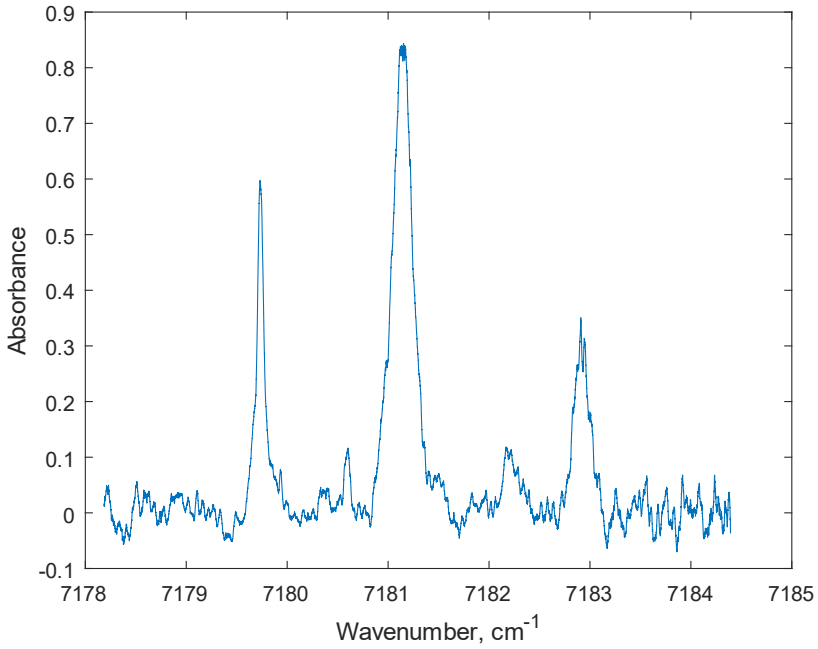

Figure 6.37. Absorbance curve for second beam of noninterference path through Hencken burner flame after background removal.

Considering that the absorbance curves in question still represent path-integrated measurements of absorbance, the possibility remains that the measurements are significantly influenced by co-flow in the boundary regions of the flame, which the A-FLDI sensitive length may partially include. The boundary regions of the flame contain a rapid decline in local temperature, as the flame region borders on room temperature air flow from the surrounding microchannels of the outer Hencken burner grid [90]. Examining the mean value theorem of integrals, given in Eq. (6.10.2), provides a possible explanation for the observed behavior.

$$f(c) = \frac{1}{b-a}\int_a^b f(x)dx \tag{6.10.2}$$

In simple terms, the mean value theorem states that the mean value of a function along a path is equivalent to the integral of that function divided by the difference of the starting and ending points of the path [97]. When one considers the symmetrical nature of the flame in these experiments, in which the temperature rises from room temperature to an approximate maximum of 1800 K and declines back to the room temperature, it seems quite possible that the measurements might correspond to the mean value of the temperature over such a temperature profile. As a result, the absorbance curves may simply represent the integral of the absorbance over the path in which the flame and co-flow are significant. To test this, the measured data was simulated using an input temperature of approximately 1000 K, which was a simple average between the expected co-flow and adiabatic flame temperatures. Comparisons of the measured data and model results are shown in **Fig. 6.38** and **Fig. 6.39**.

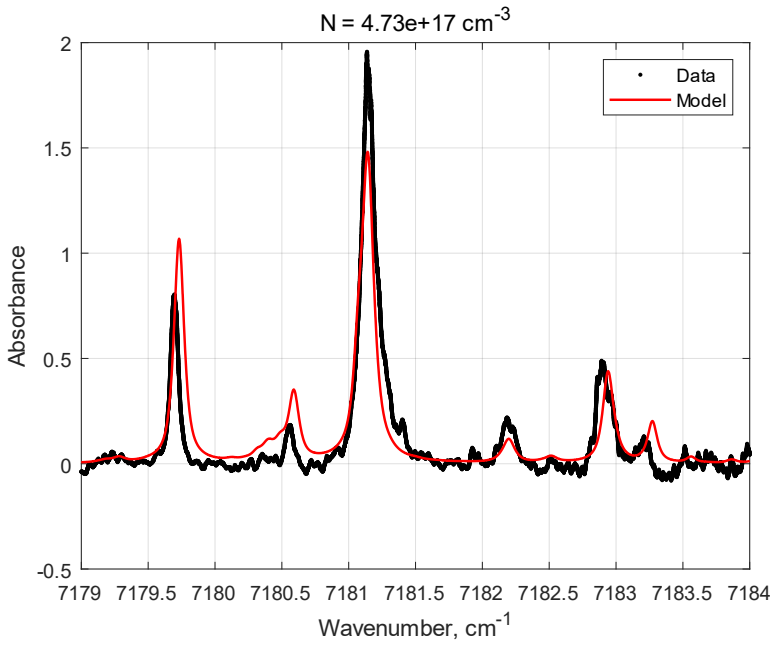

Figure 6.38. Measured and simulated absorbance as a function of wavenumber for methane-air flame via first noninterference beam of A-FLDI.

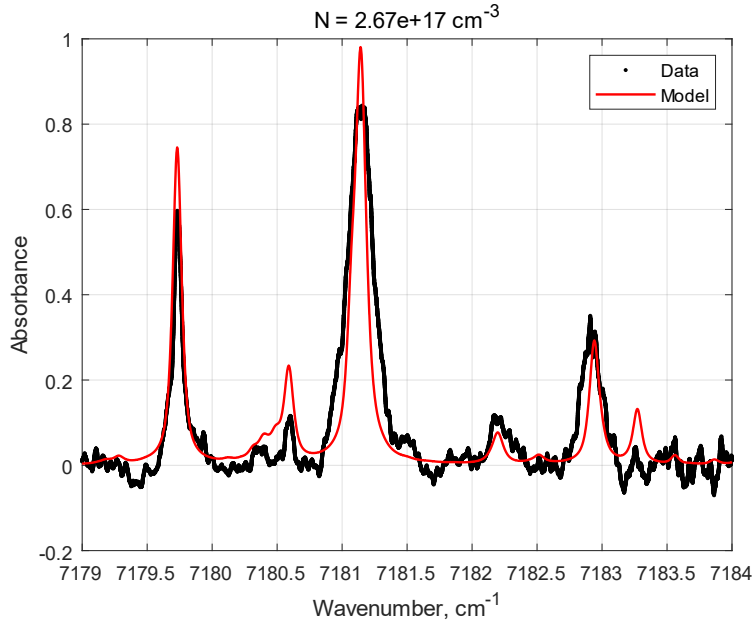

Figure 6.39. Measured and simulated absorbance as a function of wavenumber for methane-air flame via second noninterference beam of A-FLDI.

Although the simulated curves are substantially smoother than the measured data, the presence of the same absorbance peaks in each of them is quite apparent. Although, there are evident misalignments of some of the peaks. This could be caused by either small variations in pressure, which can induce a pressure shift relative to the simulated results, or more likely potential flaws in the baseline or wavenumber fitting to the original signals. These are important factors to keep in mind when performing this kind of analysis. However, it remains promising that the absorbance profiles are generally similar.

The differences in magnitude of the peaks between the simulated curves and data are thought to occur primarily due to poor fitting of the baseline in some places and the adverse effect this can have on the estimated molecular density as it is iterated. In the course of using this iterative process throughout the previous experiments, it was found that uncertainty in the baseline of up to 2.5% is possible due to the nature of curve fitting oscillatory data with higher order polynomials, which has a similar effect on the absorbance.

To further investigate the validity of this approach, it was decided to employ Eq. (6.5.2) with the baseline of the interference signal and the measured absorbances of the two beams to simulate the interference signal and compare the results. The last piece needed for this computation took the form of the phase shifts as a function of the wavenumbers. To provide an easier method of computation, the phase shifts were calculated via a 1D Hilbert transform method. Although common in other areas of phase-shifting interferometry measurements, this technique has been notably absent from FLDI research [98-101]. It provides a direct solution to computing the phase shifts in the

presence of significant laser absorption, thus overcoming the problem first noted by Smeets and George [21]. The Hilbert transform is a technique that utilizes the Fourier transform to obtain the signal frequencies, replaces negative frequencies with zero, and then performs an inverse Fourier transform to produce the original signal plus an imaginary component. The Hilbert transform of the interference signal is given by Eq. (6.10.3) [98-99].

$$H = HT(I_T) \tag{6.10.3}$$

The phase of the interference signal is then determined via Eq. (6.10.4).

$$\varphi_T = \tan^{-1}\left(\frac{Imag.(H)}{Real(H)}\right) \tag{6.10.4}$$

Both equations can be applied in the same way for the background signal. This provides a reference phase for the system. The phase shift may then be calculated via Eq. (6.10.5).

$$\Delta\varphi = \varphi_T - \varphi_{BGD} \tag{6.10.5}$$

With the phase shifts determined, it is also relatively straightforward to estimate the variations in the pressure-to-temperature ratio. The phase shifts and pressure-to-temperature ratio variations are illustrated in **Fig. 6.40** and **Fig. 6.41**, respectively. The comparison of simulated and measured signals is shown in **Fig. 6.42**, and the residual percent error between the model and data is given in **Fig. 6.43**. The residual percent error is split into two regions. This was done to separately align those regions of the curves for more accurate error estimation.

Examining these results, one can see that the interference signal contains relatively small phase shifts, rarely exceeding a magnitude of 6°. These phase shifts also appear to be caused by very small fluctuations in the local pressure-to-temperature ratio

in the flame. This is within expectations given the small separation distance between the FLDI beams and the relative uniformity of a Hencken burner flame in the inner region. It is not difficult to imagine how an array of A-FLDI beams could allow for multiple measurements of the change in this ratio along a particular dimension. It would then be a relatively simple procedure to integrate the gradient along the path and potentially infer the temperature changes perpendicular to the beam axis. An infrared camera would be ideal for such an approach.

On a related note, these phase shifts may provide a necessary constraint to estimate the temperature and concentration from the absorbance data via an underdetermined optimization process. An entire area of research could be devoted specifically to developing adequate gradient descent approaches for this minimization problem. Anecdotally, individual testing of gradient descent approaches with line searching modifications, genetic algorithms, and particle swarm optimization all seem to be promising avenues of inquiry.

Unfortunately, they require significant computational resources, often taking days to examine small portions of a total signal. This slows the refinement of the optimization problem considerably. Research in other areas using phase-shifting interferometry and laser absorption spectroscopy may provide promising springboards from which to develop this concept further. Phase unwrapping and Abel inversion both utilize measurements similar to those available from A-FLDI to extract localized estimates of quantities like temperature in axisymmetric phenomena [102-105]. However, for the sake of brevity, this discussion will be limited to assessing the feasibility of the proposed model in the form of Eq. (6.5.2).

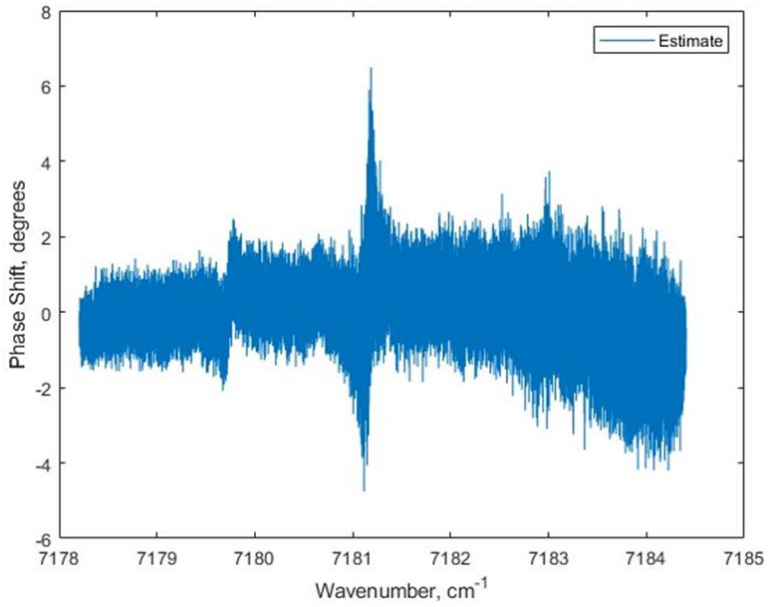

Figure 6.40. Phase shift for interference signal as a function of wavenumber from methane-air flame using A-FLDI.

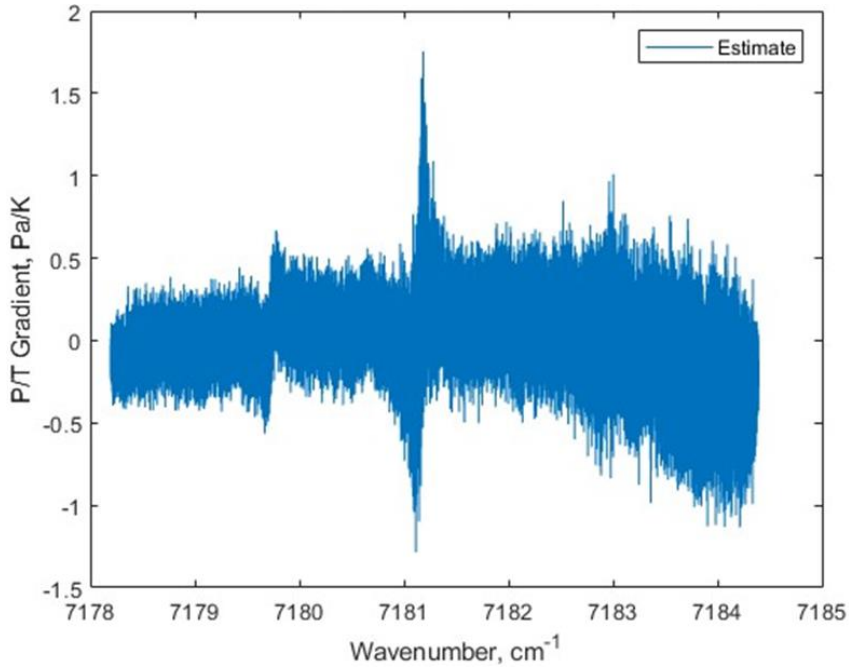

Figure 6.41. Variations in P/T gradient as a function of wavenumber for methane-air flame from A-FLDI.

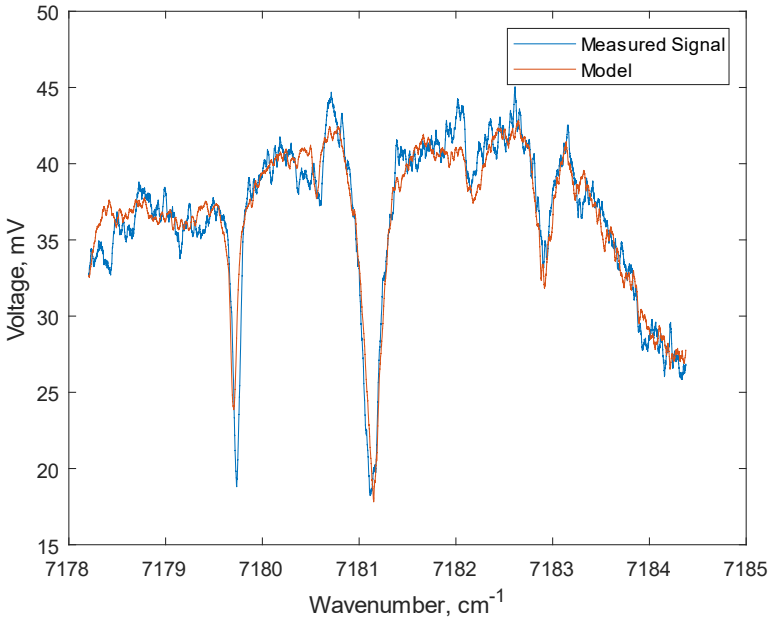

Figure 6.42. Measured and simulated interference signal results after background removal from methane-air flame via A-FLDI.

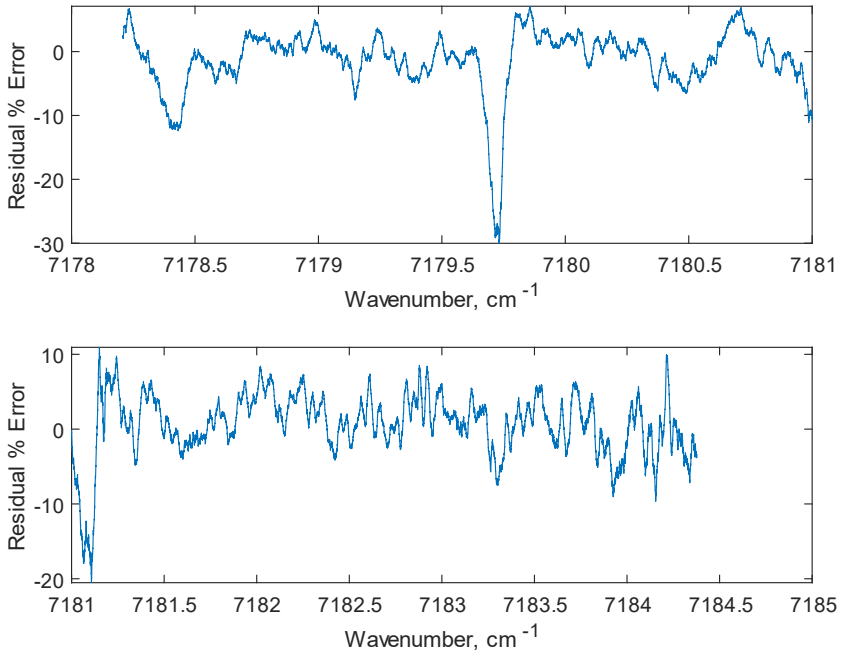

Figure 6.43. Residual error between data and model as a function of wavenumber.

Qualitatively comparing the model and measured signal, it certainly appears that the model follows the general profile of the data. Reasonable agreement is shown for several of the prominent troughs, including the main peak at 7181.1 cm^{-1}. The most significant deviations occur where the curves seem to be misaligned. This is especially evident when examining the residual percentage errors. Although the percentage errors are generally less than 10%, there are two notable exceptions, which correspond to the troughs at approximately 7179.9 and 7181.1 cm^{-1}. The first of these exhibits an error of nearly 30%, which is largely due to the difference between the peak magnitudes in the signal and model. This may be due to a poor local fit of the baseline. The error spike of nearly 20% around 7181.1 cm^{-1} appears to be somewhat erroneous. The qualitative comparison of the signal and model does not illustrate a difference in trough magnitude at that location anywhere near what is seen for 7179.9 cm^{-1}. Instead, the 20% error there seems to be due to local misalignment of the side portions of the trough minimum.

Overall, the results of the Hencken burner flame analysis illustrate that A-FLDI is able to capture similar information to that of TDLAS, and the model given by Eq. (6.5.2) is a suitable mathematical representation of the observed behavior. This may allow for future computational and simulation techniques to be developed for A-FLDI to refine its application. The last portion of this dissertation to focus on A-FLDI will consider its application in a Mach 1.5, underexpanded air jet. This will provide additional information on the ability to use A-FLDI to obtain power spectral density data and allow for a determination of the potential sensitivity of A-FLDI to absorbing species.

6.11 Experimental Setup for Testing with Mach 1.5 Air Jet

This A-FLDI design is shown in **Fig. 6.44**. All optics are unchanged from the previous experiment, but the Mach 1.5 nozzle assembly has replaced the Hencken burner in the measurement region as the phase object of interest. As with previous setups, this one was designed and built utilizing the same IR laser. The angles of the laser focusing and diverging are again exaggerated in the diagram for the sake of visibility. A view of the nozzle assembly above the Hencken burner is shown in **Fig. 6.45** for context.

The compressed air was supplied to the system at a pressure of 60 psig, which corresponded to a nozzle pressure ratio of approximately 5.25. The pressure gauge was identical to that used in all previous experiments. The air was taken from the same canister as with the small diameter, air jet and possessed similar water content of 0.23% or 63 ppm. Measurements were recorded using both the center wavelength of 1392.5 nm and the previously used wavelength scan. The sampling rate was 5 MHz, and measurements were recorded starting at the center of the air jet and at ten positions along the beam axis. The jet was translated in increments of 4 mm from position to position. Background and dark noise signals were also measured for comparison. The center wavelength signals are illustrated in **Fig. 6.46**, and the ramping signals are shown in **Fig. 6.47** and **Fig. 6.48**.

The center wavelength data shows very clearly the attenuation of the signal detection as the air jet is translated away from the focal region. This builds on the earlier data from the small diameter, air jet, and they both demonstrate that the A-FLDI exhibits the classic signal attenuation behavior expected of an FLDI system.

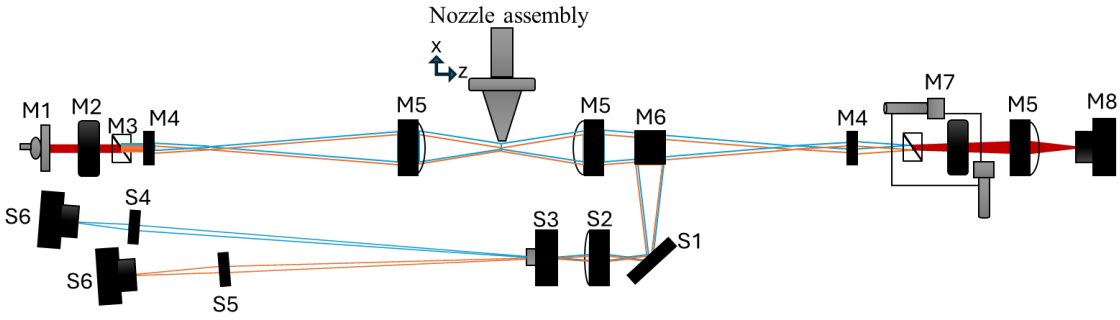

Figure 6.44. Top-down layout of 1-point A-FLDI setup and colinear, 2-path TDLAS for examining Mach 1.5 jet.

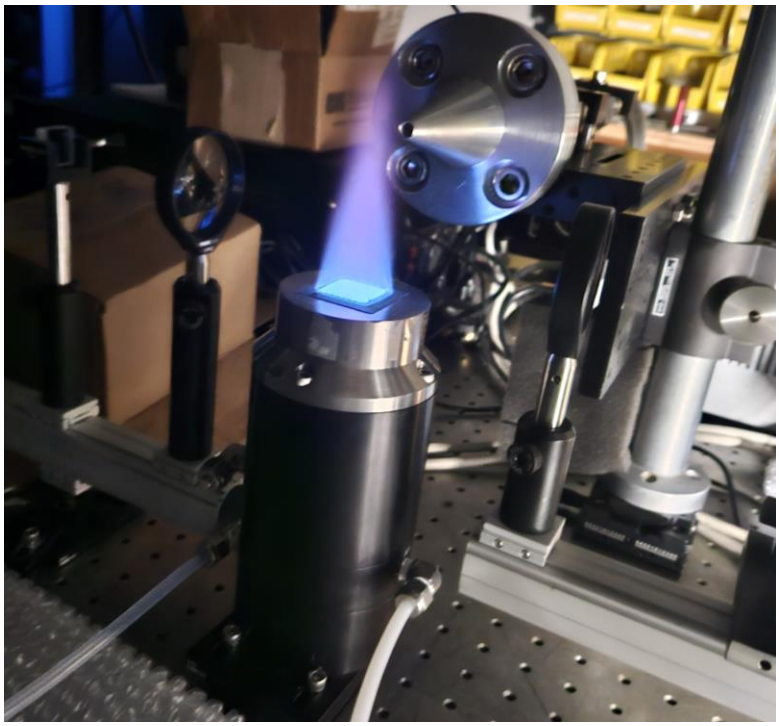

Figure 6.45. Mach 1.5, conical nozzle assembly and Hencken burner with flame in measurement region.

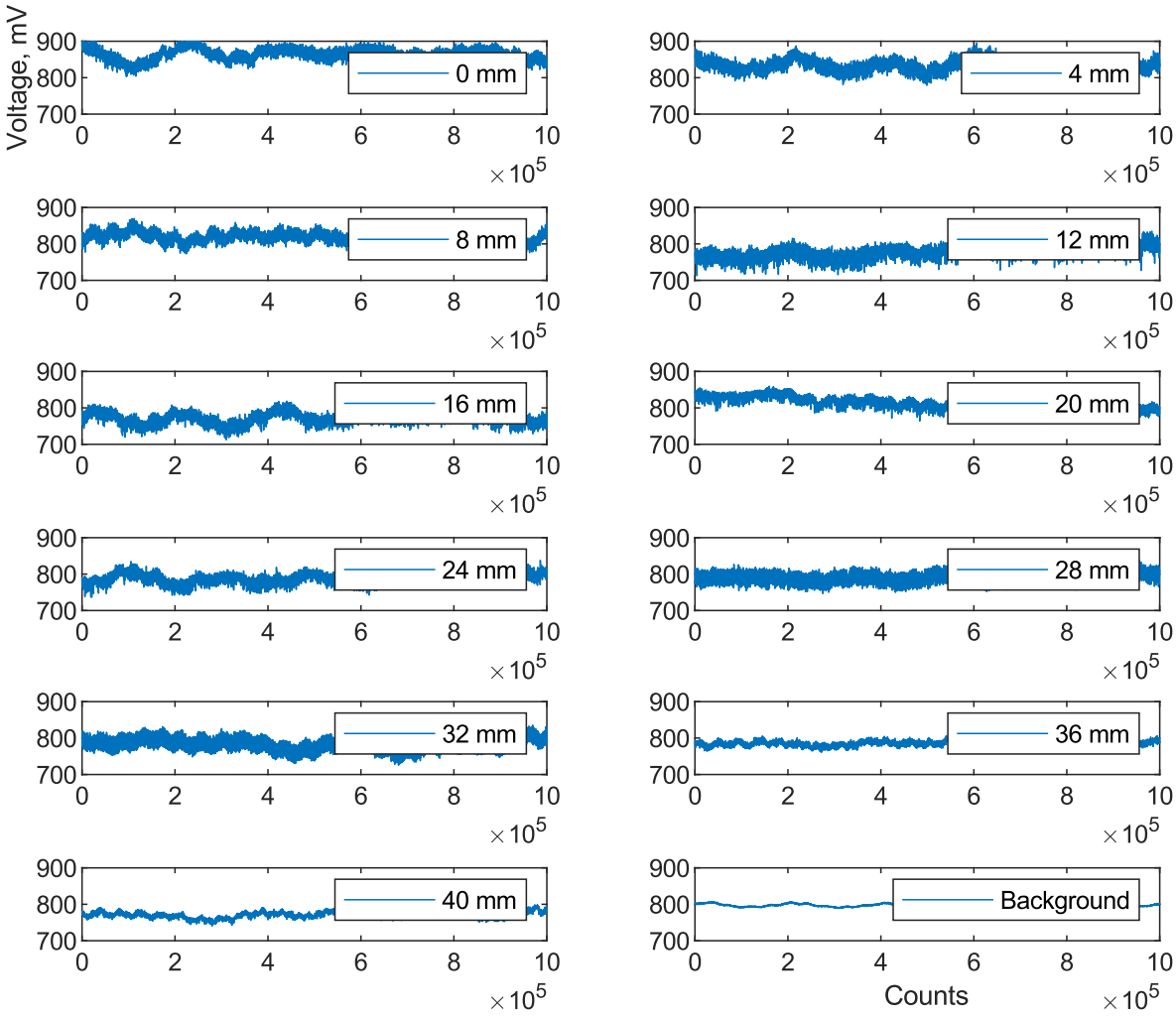

Figure 6.46. 1392.5 nm interference signals from A-FLDI in Mach 1.5, underexpanded jet of dry air.

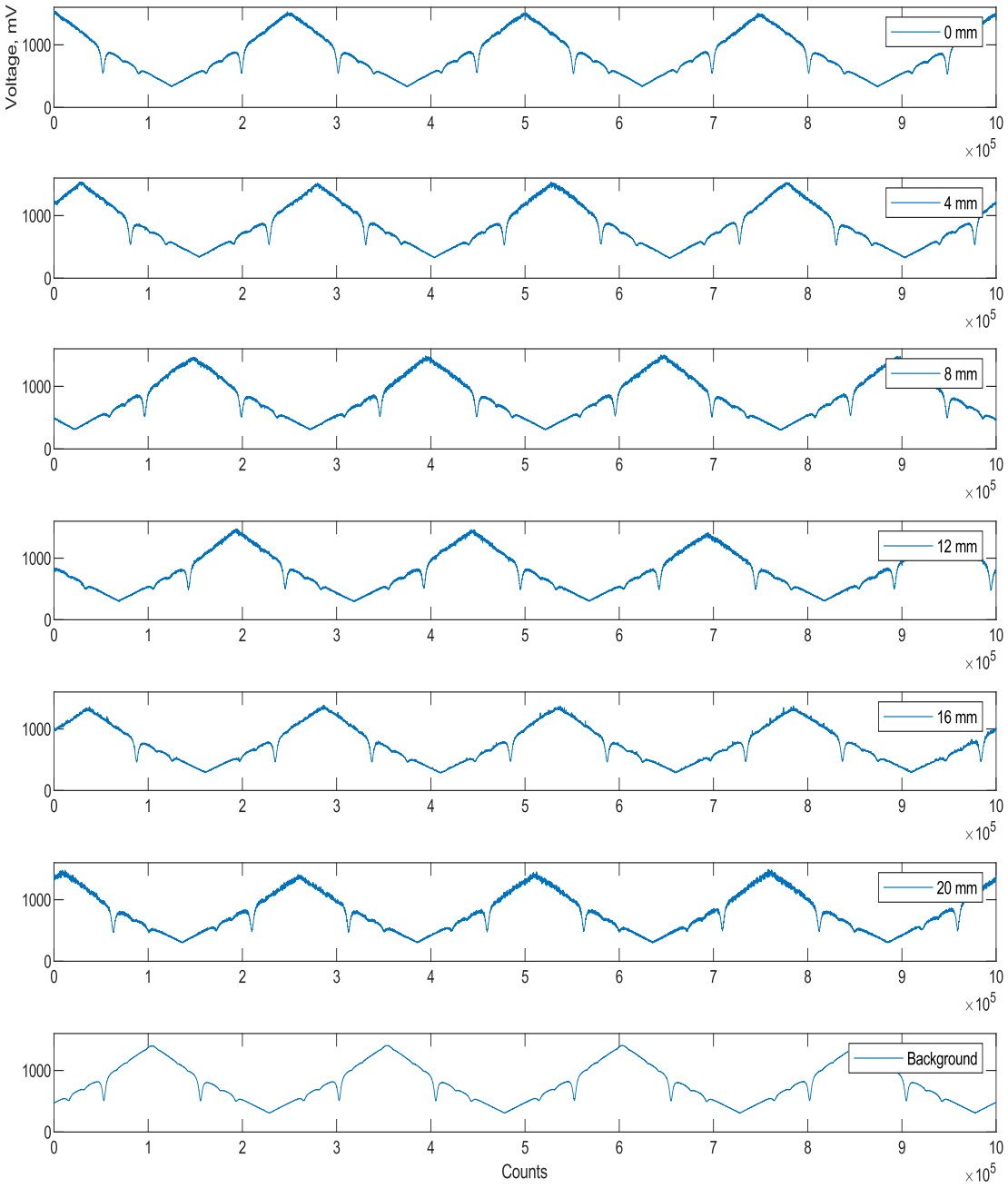

Figure 6.47. Wavelength-scanned interference signals from A-FLDI at displacements of 0-20 mm in Mach 1.5, underexpanded jet of dry air.

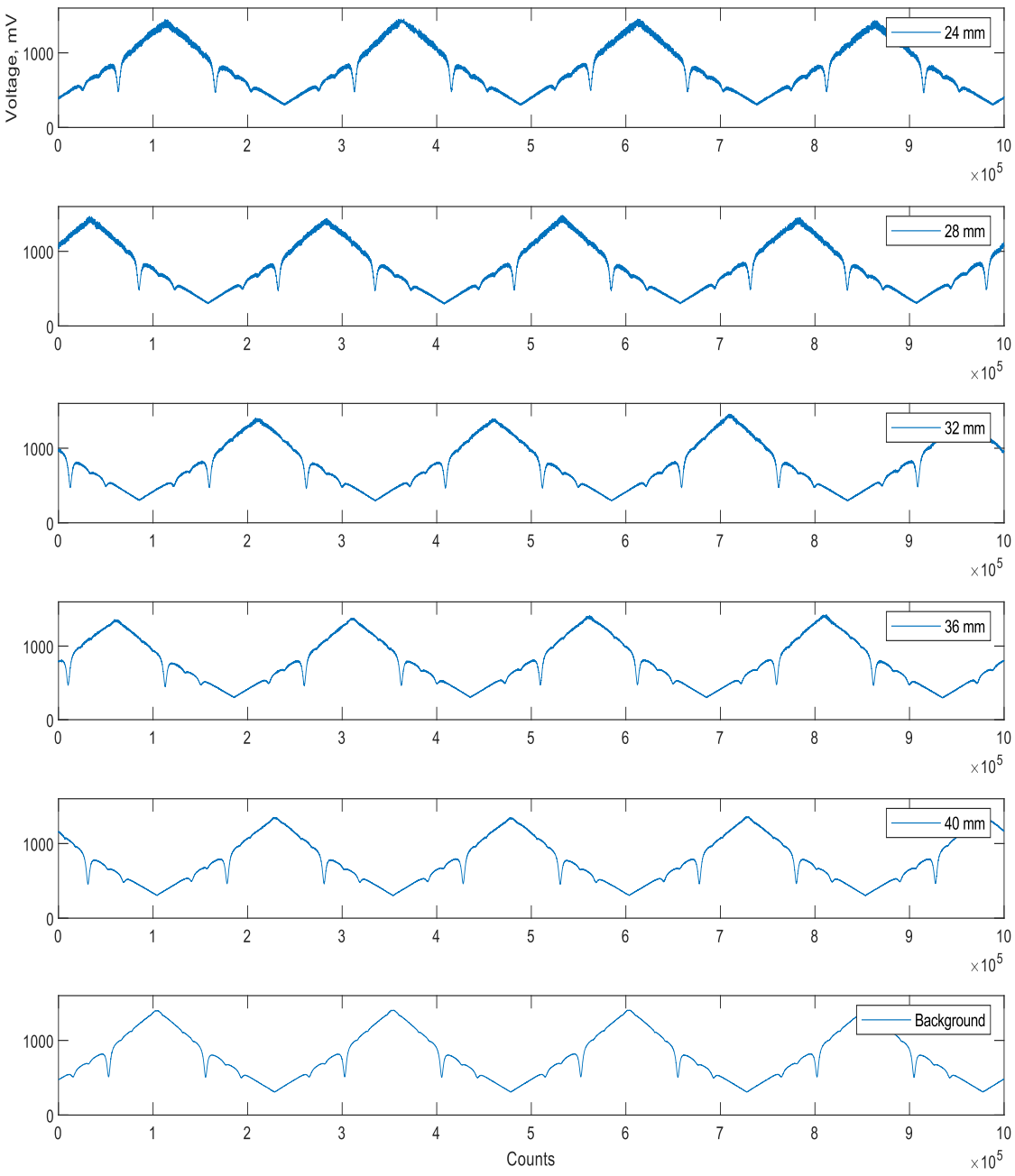

Figure 6.48. Wavelength-scanned interference signals from A-FLDI at displacements of 24-40 mm in Mach 1.5, underexpanded jet of dry air.

Due to limitations in displaying all of the wavelength-scanned signals together, the signal oscillations in these triangular waves are not as apparent. However, examining the power spectral densities of the center wavelength signals and these triangular wave signals further illustrates that the signals display very similar frequency detection. These power spectral density profiles are shown in **Fig. 6.49**.

Despite being recorded in separate tests, the majority of significant differences appear in the lower frequencies where certain dominant frequency peaks appear. Much like with previous analysis of the power spectral density profiles for this particular conical nozzle and air jet, it is not unusual for dominant frequency peaks to shift several kHz due to changes of 0.1 in the nozzle pressure ratio [38]. Since the same pressure regulator is used, the uncertainty of 5 psig could easily produce such differences. Furthermore, the 2000-point moving average that is used to estimate the mean of the triangular waveforms creates some ambiguity in the final result. The differences in magnitude in the 32 mm and 40 mm results may indicate some changes in the degree of turbulence in those regions between tests. However, the close agreement between the two data sets provides assurance that the techniques are effectively interchangeable.

The second part of analyzing this data involved isolating individual wavelength scans for each of the beam signals, fitting baselines, and fitting the wavenumber ranges. A comparison of these signal segments is shown in **Fig. 6.50**. Again, five absorbance troughs appear in the data, corresponding primarily to the effect of the water vapor present in the room's stagnant air. The general behavior of these signals can be portrayed through evaluating the interference signal. This again involves the removal of the signal's background, adjustment of the baseline, and applying a 2000-point moving average.

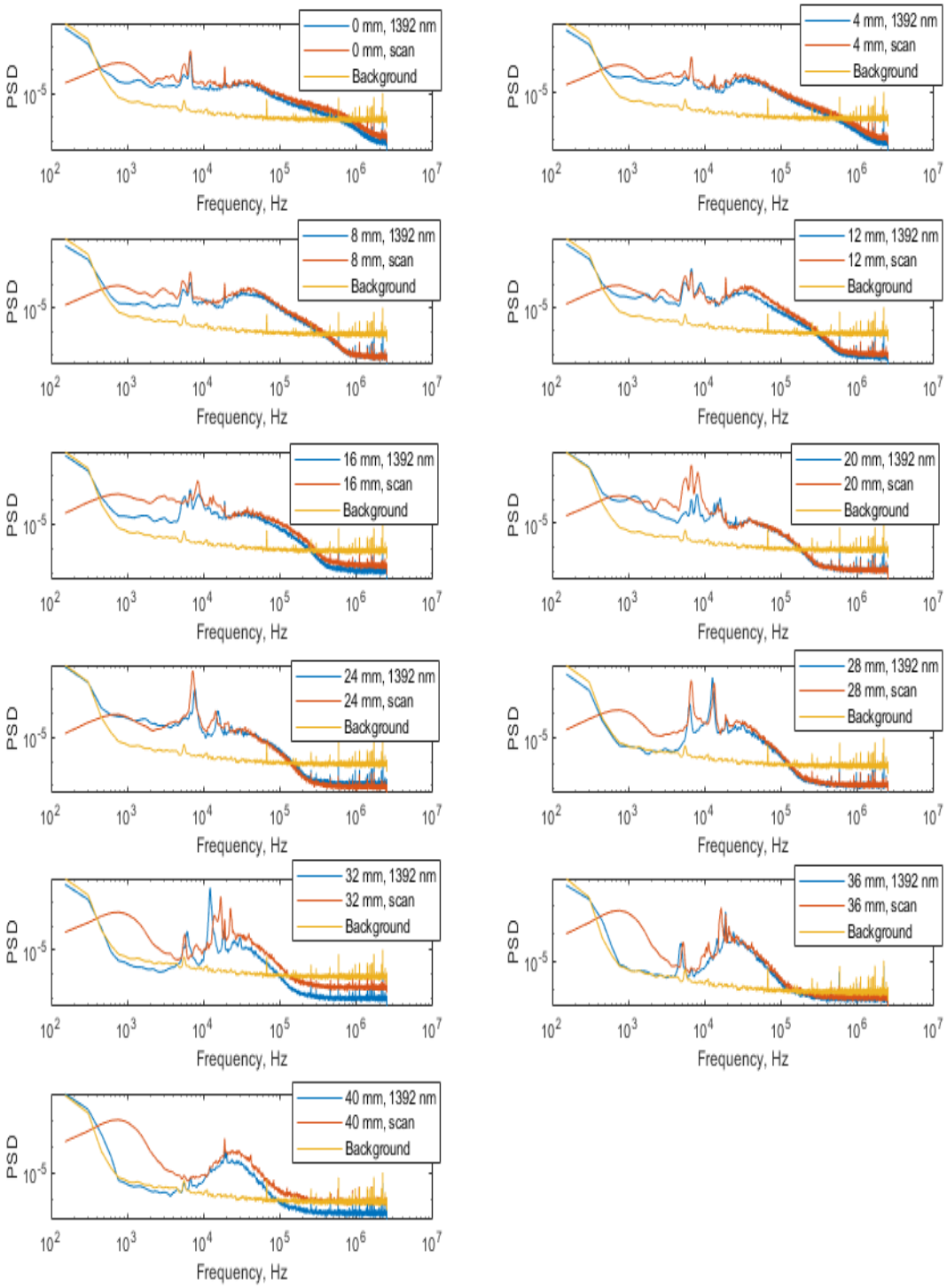

Figure 6.49. Power spectral density as a function of frequency for center wavelength and wavelength-scanned signals at varying displacements of Mach 1.5 jet from A-FLDI focal plane.

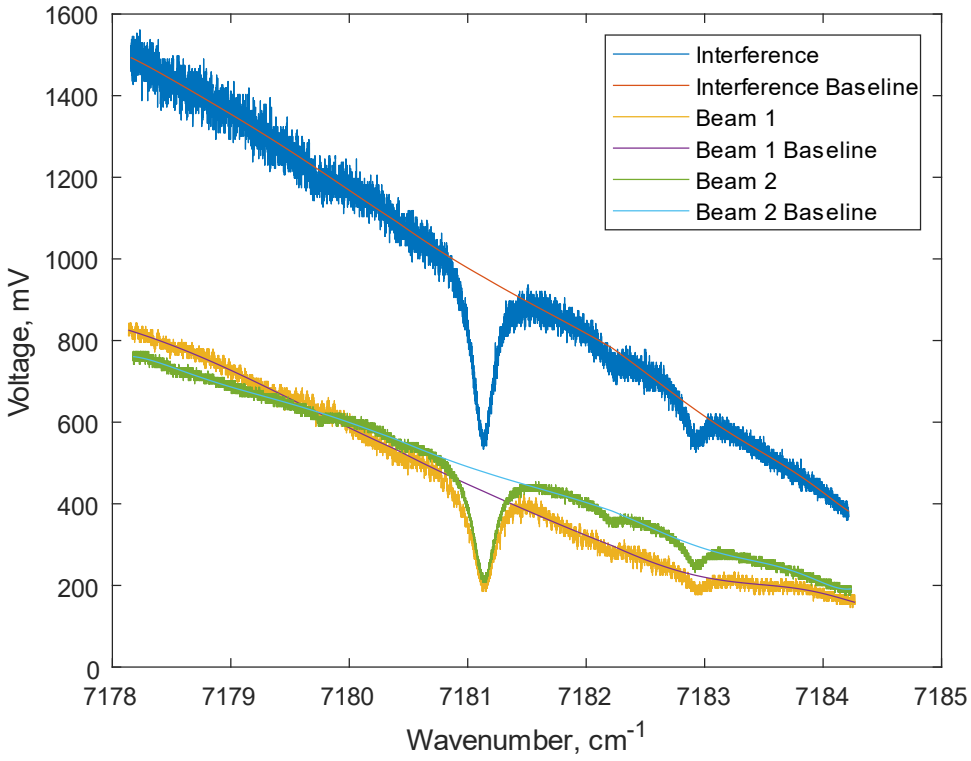

Figure 6.50. Interference and noninterference signals as functions of wavenumber from Mach 1.5 jet of dry air measured via A-FLDI.

The results in **Fig. 6.51** show a similar phenomenon to the prior Hencken burner tests. Effectively, the background removal eliminates much of the linearity in the baseline of the signal. This also occurs in the noninterference signals. However, the interference signal still shows troughs that seemingly correspond to absorbing wavenumbers.

Applying the Beer-Lambert relation as a first estimate provides a glimpse into the potential absorbance curve, which is illustrated in **Fig. 6.52**. A simulated TDLAS curve for the approximate conditions of the jet is also shown for comparison. The jet is estimated via isentropic analysis to have a higher pressure of nearly 1.2 atm and a lower temperature of approximately 204 K relative to the surroundings at the nozzle exit. Although, the presence of expansion fans at the exit likely means these values will be lower in reality.

The estimated absorbance curve from the interference signal displays significant differences in the lower wavenumbers compared to the simulated results. Examining the baseline fit and the original signal shows that the baseline in that region is lower than the signal, which creates the pronounced trough that appears in the absorbance curve. It appears highly likely that it is a case of the baseline fit failing to follow the signal. The simulated results show that the expected behavior is for absorbance to be near zero in that region with very slight peaks near 7179.7 and 7180.4 cm^{-1}. Looking at the higher wavenumbers, the comparison is a bit more favorable. A central peak is still well defined at 7181.1 cm^{-1}, and its magnitude is notably closer to that of the simulated curve. Furthermore, the two rightward peaks of the simulated results show some agreement with the estimated curve. Although, the relative magnitudes appear to be out of proportion.

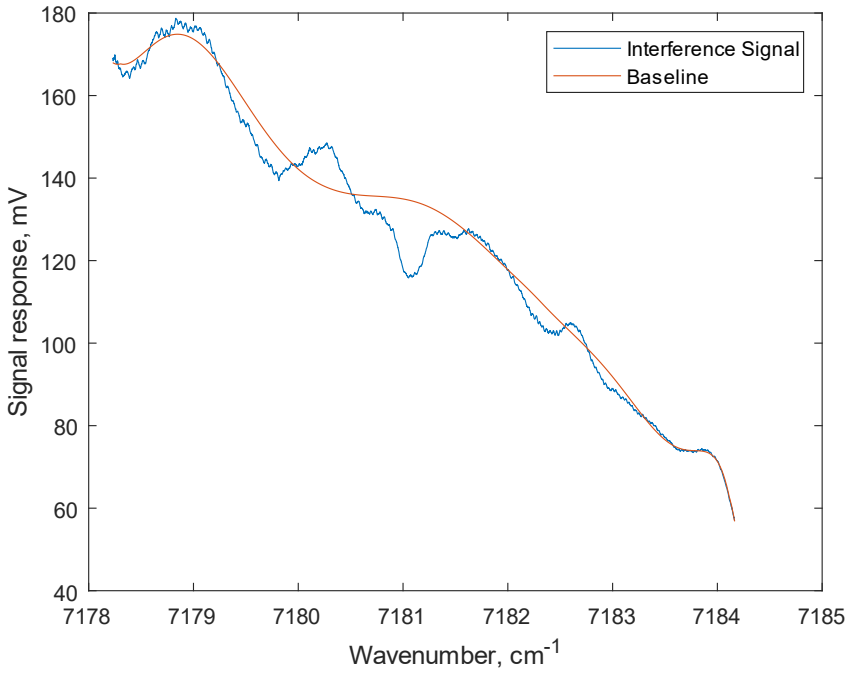

Figure 6.51. Interference signal as a function of wavenumber in Mach 1.5 jet of dry air measured via A-FLDI after background removal.

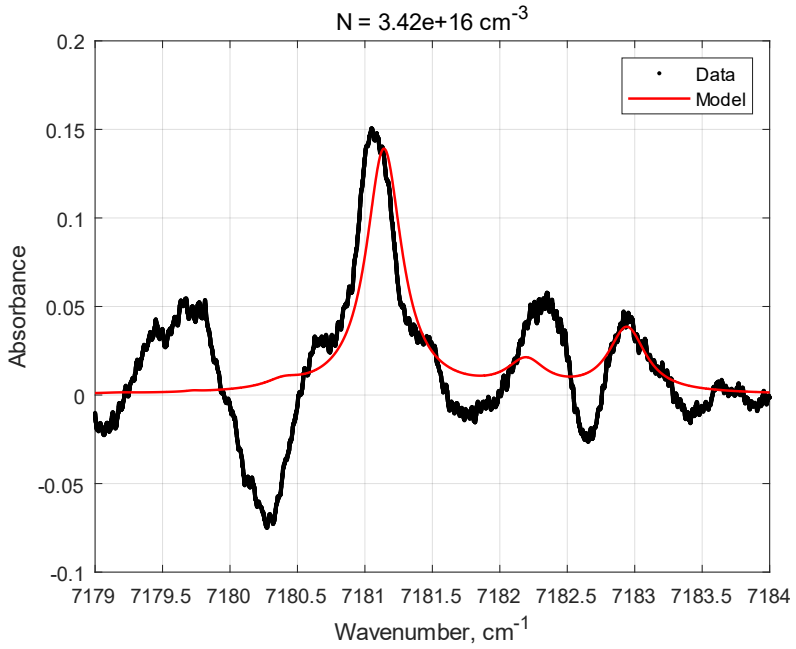

Figure 6.52. Estimated and simulated absorbance for water vapor in Mach 1.5 jet of dry air measured via A-FLDI.

This comparison provides some indication that the A-FLDI system is capable of detecting water vapor at a concentration of 63 ppm, but its sensitivity in this configuration may not extend much below that level. The molecular density estimate of 3.42E+16 cm^{-1} that is shown in **Fig. 6.52** is much lower than the expected value of 9.93E+16 cm^{-1}.

This is due to the iterative curve fitting, but it is most likely an erroneous estimate stemming from lower temperature and pressure across the air jet. Examining the noninterference signals and their baselines, given in **Fig. 6.53**, shows that they provide a more ambiguous picture of the local physics. The troughs in the signals are quite weak in magnitude and do not deviate from the baseline in well-defined ways. The baselines also appear to go below the signal in places, which would also produce negative absorbances in any estimates. This seems to suggest that the A-FLDI signal is more sensitive than the noninterference signals, which resemble TLDAS in their application. Altogether, this work provides support for the idea that absorption spectroscopy techniques are compatible with FLDI and may enable more information to be obtained during experiments than with traditional unabsorbing FLDI.

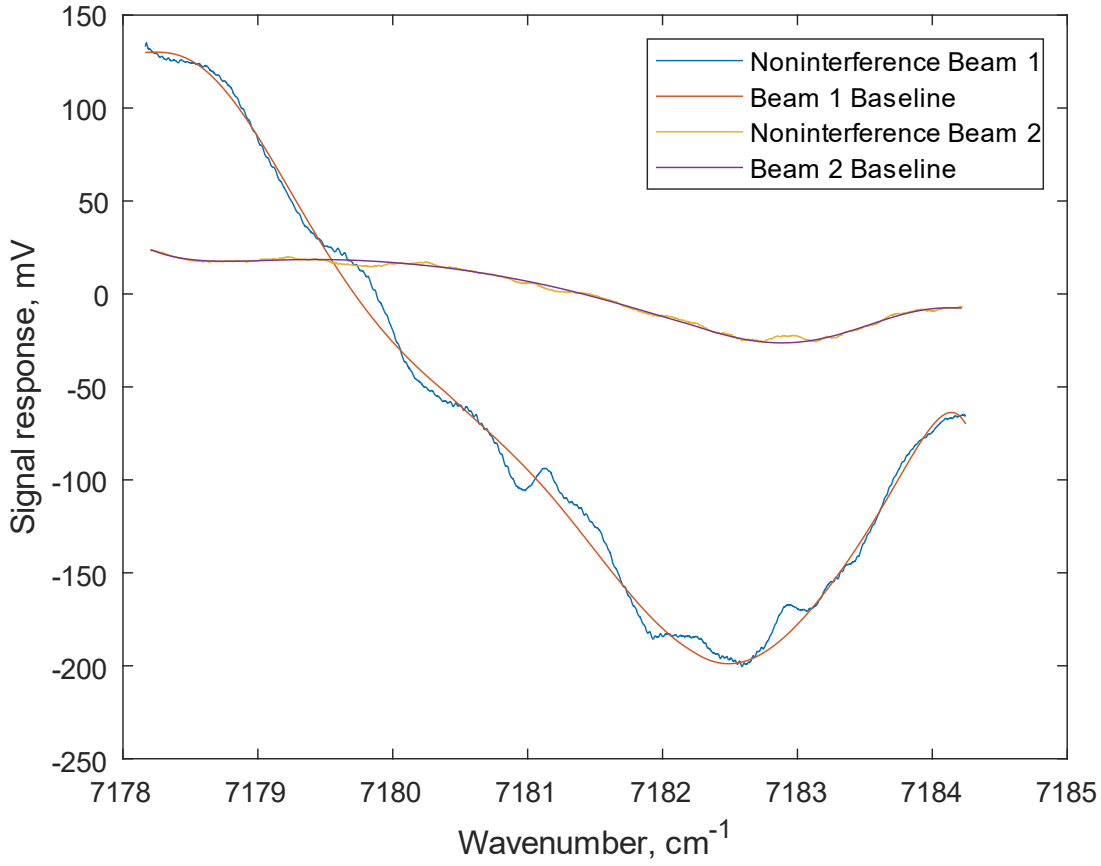

Figure 6.53. Noninterference signals as functions of wavenumber after background removal in Mach 1.5 jet of dry air measured via A-FLDI.

Section 7: Concluding Summary

Ultimately, this work expands the ways in which FLDI systems can be designed by exploring significant gaps in FLDI literature regarding the use of high-speed imaging, spatial light modulation, small-scale implementation, and integration of absorption spectroscopy. It describes the existing theoretical underpinnings for FLDI and absorption spectroscopy and discusses the operating principles of twisted-nematic liquid crystal spatial light modulators. Experiments using a high sampling rate (e.g., 900 kHz maximum) camera for data acquisition from an LA-FLDI system were discussed, and the results were presented. The results showed that high-speed imaging can achieve similar detection of dominant frequencies in flows compared to photodiode arrays. When utilizing large beam arrays, cameras with high sampling rates may provide significant advantages in ease of alignment, reducing system complexity, and obtaining more spatially resolved measurements. The primary tradeoffs appear to be the higher cost and loss of sampling rate bandwidth compared to existing photodiodes.

Next, a set of experiments utilizing a spatial light modulator to generate arbitrarily shaped beam arrays in FLDI was described. A working design of this SLM-FLDI was presented. Measurements from the SLM-FLDI and a typical 1-point FLDI were gathered in the same region of a supersonic air jet, and the power spectral density profiles were found to be notably similar. This validated that SLM-FLDI achieves similar detection of frequency information within the flow compared to 1-point FLDI. The limitations of the SLM-FLDI design, namely the creation of a base diffraction pattern and correspondingly low intensity, were described. However, hardware changes in the design are proposed to mitigate these limitations. The potential of SLM-FLDI to improve analysis of flows with

complex geometries warrants further investigation. With appropriate optics, an SLM-FLDI system could feasibly produce an array of beams that closely follows the perimeter of a model in a ground testing facility. In conjunction with high-speed imaging, this might enable simultaneous acquisition of data along much of the surface of a given model and, thus, provide an alternative means to investigate entire flow fields for turbulence, velocimetry, etc.

Following the SLM-FLDI section, experiments describing reducing the scale of FLDI were discussed. These further include tests associated with enabling it to measure quantities like number density, local pressure, or local temperature through combining FLDI and absorption spectroscopy techniques. Small-scale designs of FLDI were shown, and the physical setups were utilized for testing absorption spectroscopy through FLDI. Measurements were performed in stagnant, room temperature air using these FLDI systems, a TDLAS system, and an electrical hygrometer. The detected absorbances due to water vapor were discovered to agree between the three instrument types, which supported the concept of utilizing absorption spectroscopy through FLDI.

The last section describes several experiments conducted to further develop the concept of using absorption and taking advantage absorbing media in FLDI to create an A-FLDI system. Tests using a small diameter, air jet and a paraffin candle flame demonstrated A-FLDI sensitivity to localized disturbances in measured absorbance due to water vapor. Further inquiry via the use of a Hencken burner flame provided evidence of A-FLDI detection of mean absorbance conditions within the flame plume, which is significantly smaller than the total optical path. Comparison with laser absorption spectroscopy results in a supersonic jet of dry air showed higher sensitivity of the A-

FLDI system to low water vapor concentration. Perhaps due to the attenuation effect of FLDI, its absorbance measurements appear to be less path-integrated and may even provide a desirable alternative to TDLAS if optical system complexity is not an issue. Even more localized results of static conditions, rather than mean conditions, could potentially be obtained in the future by solving the underdetermined optimization problem presented by the combination of the calculable phase shifts and available absorbance information. This will likely necessitate less computationally intensive approaches to be widely implemented, but there are analogues in other interferometry and laser absorption spectroscopy research areas that may provide a solid foundation.

For ground testing facilities, the ability to obtain additional measurements with FLDI for the same tests has the potential to save time and money. Beyond ground testing, small-scale FLDI could become a replacement for hot wire anemometers in weather balloons performing atmospheric turbulence measurements or even gain adoption as part of a sensor suite for monitoring in spacecraft engines. The general scope of this work and potential future avenues of research are summarized in **Fig. 7.1**. It is this author's hope that this work establishes a new foundation from which advances in FLDI can be built and that having a better tool will one day prove beneficial to the wider scientific community.

Figure 7.1. Summary of work and ideas for future research.

References

1. Toepler, A. J. I. *Beobachtungen nach einer neuen optischen methode: Ein beitrag experimentalphysik*: W. Engelmann, 1906.

2. Adamson Jr, T. C., and Nicholls, J. A. "On the structure of jets from highly underexpanded nozzles into still air," *Journal of the Aerospace Sciences* Vol. 26, No. 1, 1959, pp. 16-24.

3. Behrouzi, P., and McGuirk, J. J. "Underexpanded jet development from a rectangular nozzle with aft-deck," *AIAA Journal* Vol. 53, No. 5, 2015, pp. 1287-1298.

4. Franquet, E., Perrier, V., Gibout, S., and Bruel, P. "Free underexpanded jets in a quiescent medium: A review," *Progress in Aerospace Sciences* Vol. 77, 2015, pp. 25-53.

5. Ma, L., Li, X., Sanders, S. T., Caswell, A. W., Roy, S., Plemmons, D. H., and Gord, J. R. "50-kHz-rate 2D imaging of temperature and H2O concentration at the exhaust plane of a J85 engine using hyperspectral tomography," *Optics Express* Vol. 21, No. 1, 2013, pp. 1152-1162.
doi: 10.1364/OE.21.001152

6. Crist, S., Glass, D., and Sherman, P. "Study of the highly underexpanded sonic jet," *AIAA Journal* Vol. 4, No. 1, 1966, pp. 68-71.

7. Santiago, J. G., and Dutton, J. C. "Velocity measurements of a jet injected into a supersonic crossflow," *Journal of Propulsion and Power* Vol. 13, No. 2, 1997, pp. 264-273.

8. Gamba, M., Miller, V., Mungal, G., and Hanson, R. "Combustion characteristics of an inlet/supersonic combustor model," *50th AIAA Aerospace Sciences Meeting including the New Horizons Forum and Aerospace Exposition*. 2012, p. 612.

9. Kidd, F. G., Narayanaswamy, V., Danehy, P. M., Inman, J. A., Bathel, B. F., Cabell, K. F., Hass, N., Capriotti, D., Drozda, T. G., and Johansen, C. T. "Characterization of the NASA Langley arc heated scramjet test facility using NO PLIF," *30th AIAA Aerodynamic Measurement Technology and Ground Testing Conference*. 2014, p. 2652.

10. Dogariu, A., Dogariu, L. E., Smith, M. S., Lafferty, J., and Miles, R. B. "Single shot temperature measurements using coherent anti-Stokes Raman scattering in Mach 14 flow at the Hypervelocity AEDC Tunnel 9," *AIAA Scitech 2019 Forum*. 2019, p. 1089.

11. Abram, C., Fond, B., and Beyrau, F. "Temperature measurement techniques for gas and liquid flows using thermographic phosphor tracer particles," *Progress in Energy and Combustion Science* Vol. 64, 2018, pp. 93-156.
doi: 10.1016/j.pecs.2017.09.001

12. Begley, R., Harvey, A., and Byer, R. L. "Coherent anti-Stokes Raman spectroscopy," *Applied Physics Letters* Vol. 25, No. 7, 1974, pp. 387-390.

13. Russell, C., Jiang, N., Danehy, P., Zhang, Z., and Roy, S. "Three-component flow velocity measurements with stereoscopic picosecond laser electronic excitation tagging," *Applied Optics* Vol. 60, No. 15, 2021, pp. C121-C130.
doi: 10.1364/AO.420067

14. Clark, A., McCord, W., and Zhang, Z. "Air resonance enhanced multiphoton ionization tagging velocimetry," *Applied Optics* Vol. 61, No. 13, 2022, pp. 3748-3753.
doi: 10.1364/AO.455216

15. Danehy, P. M., Burns, R. A., Reese, D. T., Retter, J. E., and Kearney, S. P. "FLEET Velocimetry for Aerodynamics," *Annual Review of Fluid Mechanics* Vol. 54, 2022, pp. 525-553.

16. Gross, K. P., McKenzie, R. L., and Logan, P. "Measurements of temperature, density, pressure, and their fluctuations in supersonic turbulence using laser-induced fluorescence," *Experiments in Fluids* Vol. 5, No. 6, 1987, pp. 372-380.
doi: 10.1007/bf00264400

17. Miller, V. A., Gamba, M., Mungal, M. G., and Hanson, R. K. "Single-and dual-band collection toluene PLIF thermometry in supersonic flows," *Experiments in Fluids* Vol. 54, No. 6, 2013, pp. 1-13.

18. Chang, L. S., Strand, C. L., Jeffries, J. B., Hanson, R. K., Diskin, G. S., Gaffney, R. L., and Capriotti, D. P. "Supersonic mass-flux measurements via tunable diode laser absorption and nonuniform flow modeling," *AIAA Journal* Vol. 49, No. 12, 2011, pp. 2783-2791.

19. Zhou, X., Liu, X., Jeffries, J. B., and Hanson, R. "Development of a sensor for temperature and water concentration in combustion gases using a single tunable diode laser," *Measurement Science and Technology* Vol. 14, No. 8, 2003, p. 1459.

20. Farooq, A., Jeffries, J. B., and Hanson, R. K. "In situ combustion measurements of H2O and temperature near 2.5 μm using tunable diode laser absorption," *Measurement Science and Technology* Vol. 19, No. 7, 2008, p. 075604.

21. Smeets, G., and George, A. "Laser-Differential Interferometer Applications in Gas Dynamics." Institute Franco-Allemand de Recherches de Saint-Louis, 1975, pp. 1-67.

22. Settles, G. S., and Fulghum, M. R. "The Focusing Laser Differential Interferometer, an Instrument for Localized Turbulence Measurements in Refractive Flows," *Journal of Fluids Engineering* Vol. 138, No. 10, 2016.
doi: 10.1115/1.4033960

23. Toyota, T., and Nishida, M. "Diagnostics of shock tube flows by laser interferometry," *Kyoto University Faculty Engineering Memoirs* Vol. 44, 1982, pp. 410-429.

24. Parziale, N. J., Shepherd, J. E., and Hornung, H. G. "Differential Interferometric Measurement of Instability in a Hypervelocity Boundary Layer," *AIAA Journal* Vol. 51, No. 3, 2012, pp. 750-754.
doi: 10.2514/1.J052013

25. Parziale, N. J., Shepherd, J. E., and Hornung, H. G. "Free-stream density perturbations in a reflected-shock tunnel," *Experiments in Fluids* Vol. 55, No. 2, 2014, p. 1665.
doi: 10.1007/s00348-014-1665-0

26. Ceruzzi, A., McManamen, B., and Cadou, C. P. "Demonstration of Two-Point Focused Laser Differential Interferometry (2pFLDI) in a Mach 18 flow," *AIAA SciTech 2021 Forum*. American Institute of Aeronautics and Astronautics, 2021.

27. Benitez, E. K., Borg, M. P., Rhodes, C., and Jewell, J. S. "Optical-Axis Spatial Sensitivity of a Simulated Focused Laser Differential Interferometer," *AIAA Journal* Vol. 61, No. 5, 2023, pp. 1925-1938.
doi: 10.2514/1.J062270

28. Benitez, E. K., Borg, M. P., Luke Hill, J., Aultman, M. T., Duan, L., Running, C. L., and Jewell, J. S. "Quantitative focused laser differential interferometry with hypersonic turbulent boundary layers," *Applied Optics* Vol. 61, No. 31, 2022, pp. 9203-9216.
doi: 10.1364/AO.465714

29. Dean, T., Siddiqui, F., Gragston, M. T., and Bowersox, R. D. "Index of Refraction Fluctuation Spectra in Aerothermochemical Non-equilibrium Shock Layers," *AIAA SciTech 2023 Forum*. American Institute of Aeronautics and Astronautics, 2023.

30. Sander, T., Jakobs, L., and Mundt, C. "Measuring the Free-Stream Turbulence Spectrum in the Shock Tunnel HELM using the Focused Laser Differential

Interferometry (FLDI)," *25th AIAA International Space Planes and Hypersonic Systems and Technologies Conference*. American Institute of Aeronautics and Astronautics, 2023.

31. Lawson, J. M., and Austin, J. M. "Recovering density disturbance spectra from FLDI. Part 1," *Applied Optics* Vol. 62, No. 12, 2023, pp. 3042-3053. doi: 10.1364/AO.480352

32. Lawson, J. M., and Austin, J. M. "Recovering density disturbance spectra from FLDI. Part 2: comparisons with previous methods," *Applied Optics* Vol. 62, No. 12, 2023, pp. 3054-3061. doi: 10.1364/AO.480354

33. Berger, A. R., and Borg, M. P. "Co-linear FLDI/Schlieren and Surface Pressure Measurements of Bluntness Induced Elongated Structures in Hypersonic Flow," *AIAA SciTech 2023 Forum*. American Institute of Aeronautics and Astronautics, 2023.

34. Gragston, M., Price, T., Davenport, K., Zhang, Z., and Schmisseur, J. D. "Linear array focused-laser differential interferometry for single-shot multi-point flow disturbance measurements," *Optics Letters* Vol. 46, No. 1, 2021, pp. 154-157. doi: 10.1364/OL.412495

35. Houpt, A., and Leonov, S. "Cylindrical Focused Laser Differential Interferometer," *AIAA Journal* Vol. 59, No. 4, 2021, pp. 1142-1150. doi: 10.2514/1.J059750

36. Weisberger, J. M., Bathel, B. F., Herring, G. C., Buck, G. M., Jones, S. B., and Cavone, A. A. "Multi-point line focused laser differential interferometer for high-speed flow fluctuation measurements," *Applied Optics* Vol. 59, No. 35, 2020, pp. 11180-11195. doi: 10.1364/AO.411006

37. Holladay, S., and Zhang, Z. "Supersonic and Plasma Flow Characterization by 1D Focused Laser Differential Interferometry," *AIAA SciTech 2022 Forum*. American Institute of Aeronautics and Astronautics, 2022.

38. Price, T. J., Gragston, M., and Kreth, P. A. "Analysis of Screech Phenomena in a Mach 1.0 Jet with Linear Array Focused Laser Differential Interferometry," *AIAA SciTech 2022 Forum*. American Institute of Aeronautics and Astronautics, 2022.

39. Davenport, K., and Gragston, M. "Simultaneous Velocity Profile and Scalar Spectra with Linear Array-Focused Laser Differential Interferometry," *AIAA Journal*, 2022, pp. 1-6. doi: 10.2514/1.J061945

40. Hoffman, E. N. A., Rodriguez, J. M., Cottier, S. M., Combs, C. S., Bathel, B. F., Weisberger, J. M., Jones, S. B., Schmisseur, J. D., and Kreth, P. A. "Modal Analysis of Cylinder-Induced Transitional Shock-Wave/Boundary-Layer Interaction Unsteadiness," *AIAA Journal* Vol. 60, No. 5, 2022, pp. 2730-2748.
doi: 10.2514/1.J060880

41. Hameed, A., Parziale, N. J., Paquin, L. A., Laurence, S. J., Yu, W. M., and Austin, J. M. "Characterization of Transitional, High-Enthalpy Boundary Layers on a Blunted Cone. Part II: FLDI and Higher Order Spectral Analysis," *AIAA SciTech 2023 Forum*. American Institute of Aeronautics and Astronautics, 2023.

42. Jiang, N., Hsu, P. S., Slipchenko, M., Roy, S., Lauriola, D. K., Webb, A. M., Meyer, T. R., Gragston, M., Parker, R., Portoni, P., McDermott, C., Seitz, K., and Wadhams, T. P. "Megahertz-Rate Imaging of Hypersonic Boundary-Layer Instabilities in a Mach 10 Shock Tunnel," *AIAA Journal* Vol. 61, No. 2, 2022, pp. 534-542.
doi: 10.2514/1.J061880

43. Weisberger, J. M., Bathel, B. F., Lee, J. W., and Cavone, A. A. "Linear Array Photodiode and Data Acquisition System Development for Multi-Point Line FLDI Measurements," *AIAA SciTech 2022 Forum*. American Institute of Aeronautics and Astronautics, 2022.

44. Davenport, K., Ledbetter, S., Siddiqui, F., and Gragston, M. T. "Development of a Simple Compact Photodiode Array for Use with Linear Array-FLDI," *AIAA SciTech 2023 Forum*. American Institute of Aeronautics and Astronautics, 2023.

45. Parziale, N. J., Shepherd, J. E., and Hornung, H. G. "Differential Interferometric Measurement of Instability in a Hypervelocity Boundary Layer," *AIAA Journal* Vol. 51, No. 3, 2013, pp. 750-754.
doi: 10.2514/1.J052013

46. Parziale, N. J., Shepherd, J. E., and Hornung, H. G. "Observations of hypervelocity boundary-layer instability," *Journal of Fluid Mechanics* Vol. 781, 2015, pp. 87-112.
doi: 10.1017/jfm.2015.489

47. Schmidt, B. E., and Shepherd, J. E. "Analysis of focused laser differential interferometry," *Applied Optics* Vol. 54, No. 28, 2015, pp. 8459-8472.
doi: 10.1364/AO.54.008459

48. Kai, Y., Garen, W., and Teubner, U. "Experimental Investigations on Microshock Waves and Contact Surfaces," *Physical Review Letters* Vol. 120, 2018.
doi: 10.1103/PhysRevLett.120.064501

49. Ceruzzi, A., Callis, B., Weber, D., and Cadou, C. P. "Application of Focused Laser Differential Interferometry (FLDI) in a Supersonic Boundary Layer," *AIAA SciTech 2020 Forum*.

50. Davenport, K., and Gragston, M. "Simultaneous Velocity Profile and Scalar Spectra with Linear Array-Focused Laser Differential Interferometry," *AIAA Journal* Vol. 61, No. 2, 2022, pp. 934-939.
doi: 10.2514/1.J061945

51. Lawson, J. M., Neet, M. C., Grossman, I. J., and Austin, J. M. "Characterization of a Focused Laser Differential Interferometer," *AIAA SciTech 2019 Forum*.

52. Price, T., Gragston, M., Schmisseur, J., and Kreth, P. "Measurement of Supersonic Jet Screech with Focused Laser Differential Interferometry," *Applied Optics* Vol. 59, 2020.
doi: 10.1364/AO.402011

53. Bathel, B. F., Herring, G. C., Weisberger, J. M., Chou, A., and Jones, S. B. "Simultaneous focused laser differential interferometry and high-speed schlieren in a Mach 6 flow," *Measurement Science and Technology* Vol. 32, No. 9, 2021, p. 095907.
doi: 10.1088/1361-6501/abf67a

54. Weisberger, J., Bathel, B., Herring, G., Buck, G., Jones, S., and Cavone, A. "Multi-point line focused laser differential interferometer for high-speed flow fluctuation measurements," *Applied Optics* Vol. 59, 2020, p. 11180.
doi: 10.1364/AO.411006

55. Gragston, M., Price, T., Davenport, K., Zhang, Z., and Schmisseur, J. "Linear Array Focused-Laser Differential Interferometry for Single-Shot Multi-Point Flow Disturbance Measurements," *Optics Letters* Vol. 46, 2020.
doi: 10.1364/OL.412495

56. Chism, J. R., Gragston, M., Peltier, S. J., and McManus, T. A. "Measurements of a Mach 2.3 Turbulent Boundary Layer Using High-Speed Imaging of Linear Array-FLDI," *AIAA Aviation 2022 Forum*. American Institute of Aeronautics and Astronautics, 2022.

57. Weisberger, J. M., Bathel, B. F., Herring, G. C., and Chou, A. "Absorption Laser Differential Interferometry for Simultaneous Colinear Flow Property and Fluctuation Measurements," *AIAA Aviation 2023 Forum*. American Institute of Aeronautics and Astronautics, 2023.

58. Neet, M. C., Lawson, J. M., and Austin, J. M. "Design, alignment, and calibration of a focused laser differential interferometer," *Applied Optics* Vol. 60, No. 26, 2021, pp. 7903-7909.
doi: 10.1364/AO.435112

59. Kawata, S., Shimamura, K., Suzuki, S., Manoharan, R., and Tanno, H. "Hypersonic boundary transition measurement by Focused Laser Differential Interferometry in high-enthalpy shock tunnel HIEST," *AIAA SciTech 2022 Forum*. American Institute of Aeronautics and Astronautics, 2022.

60. Ceruzzi, A., and Cadou, C. "Simultaneous Velocity and Density Gradient Measurements using Two-Point Focused Laser Differential Interferometry", 2019.

61. Welch, P. "The use of fast Fourier transform for the estimation of power spectra: A method based on time averaging over short, modified periodograms," *IEEE Transactions on Audio and Electroacoustics* Vol. 15, No. 2, 1967, pp. 70-73.
doi: 10.1109/TAU.1967.1161901

62. Hermerschmidt, A. "Theoretical Foundations," *OptiXplorer Manual*. Vol. 1.8, HOLOEYE Photonics AG, 2019, pp. 10-34.

63. Kim, H., and Lee, Y. H. "Unique measurement of the parameters of a twisted-nematic liquid-crystal display," *Applied Optics* Vol. 44, No. 9, 2005, pp. 1642-1649.
doi: 10.1364/AO.44.001642

64. Jelloian, C. C., Minesi, N. Q., and Spearrin, R. M. "High-speed mid-infrared laser absorption spectroscopy of CO2 for shock-induced thermal non-equilibrium studies of planetary entry," *Applied Physics B* Vol. 128, No. 12, 2022, p. 216.
doi: 10.1007/s00340-022-07934-4

65. Ghanekar, S., Rajasegar, R., Traina, N., Mitsingas, C., Kesler, R. M., Horn, G. P., Zevotek, R., Kerber, S., and Lee, T. "In-situ measurement of water-vapor in fire environments using a real-time tunable diode laser based system," *Fire Safety Journal* Vol. 120, 2021, p. 103114.
doi: https://doi.org/10.1016/j.firesaf.2020.103114

66. Nie, W., Xu, Z., Kan, R., Ruan, J., Yao, L., Wang, B., and He, Y. "Development of a Dew/Frost Point Temperature Sensor Based on Tunable Diode Laser Absorption Spectroscopy and Its Application in a Cryogenic Wind Tunnel," *Sensors*; Vol. 18, No. 8, 2018.
doi: 10.3390/s18082704

67. Gharavi, M., and Buckley, S. G. "Diode laser absorption spectroscopy measurement of linestrengths and pressure broadening coefficients of the methane

2ν3 band at elevated temperatures," *Journal of Molecular Spectroscopy* Vol. 229, No. 1, 2005, pp. 78-88.
doi: https://doi.org/10.1016/j.jms.2004.07.016

68. Wu, K., Li, F., Cheng, X., Yang, Y., Lin, X., and Xia, Y. "Sensitive detection of CO2 concentration and temperature for hot gases using quantum-cascade laser absorption spectroscopy near 4.2 μm," *Applied Physics B* Vol. 117, No. 2, 2014, pp. 659-666.
doi: 10.1007/s00340-014-5880-4

69. Liu, Y., Lin, J., Huang, G., Guo, Y., and Duan, C. "Simple empirical analytical approximation to the Voigt profile," *Journal of the Optical Society of America B* Vol. 18, No. 5, 2001, pp. 666-672.
doi: 10.1364/JOSAB.18.000666

70. Olivero, J. J., and Longbothum, R. L. "Empirical fits to the Voigt line width: A brief review," *Journal of Quantitative Spectroscopy and Radiative Transfer* Vol. 17, No. 2, 1977, pp. 233-236.
doi: https://doi.org/10.1016/0022-4073(77)90161-3

71. Penner, S. S., and Kavanagh, R. W. "Radiation from Isolated Spectral Lines with Combined Doppler and Lorentz Broadening*," *Journal of the Optical Society of America* Vol. 43, No. 5, 1953, pp. 385-388.
doi: 10.1364/JOSA.43.000385

72. Büttner, L., Thümmler, M., and Czarske, J. "Velocity measurements with structured light transmitted through a multimode optical fiber using digital optical phase conjugation," *Optics Express* Vol. 28, No. 6, 2020, pp. 8064-8075.
doi: 10.1364/OE.386047

73. Kozacki, T., Mikuła-Zdańkowska, M., Martinez-Carranza, J., and Idicula, M. S. "Single-shot digital multiplexed holography for the measurement of deep shapes," *Optics Express* Vol. 29, No. 14, 2021, pp. 21965-21977.
doi: 10.1364/OE.428419

74. Bulbul, A., and Rosen, J. "Super-resolution imaging by optical incoherent synthetic aperture with one channel at a time," *Photonics Research* Vol. 9, No. 7, 2021, pp. 1172-1181.
doi: 10.1364/PRJ.422381

75. Cheng, Z., and Wang, L. V. "Focusing light into scattering media with ultrasound-induced field perturbation," *Light: Science & Applications* Vol. 10, No. 1, 2021, p. 159.
doi: 10.1038/s41377-021-00605-7

76. Bueno, J. M., Hernández, G., Skorsetz, M., and Artal, P. "Improving Multiphoton Microscopy by Combining Spherical Aberration Patterns and Variable Axicons," *Photonics*; Vol. 8, No. 12, 2021.
doi: 10.3390/photonics8120573

77. Zhao, Z., Duan, J., and Liu, J. "Speckle reduction in holographic display with partially spatial coherent illumination," *Optics Communications* Vol. 507, 2022, p. 127604.
doi: https://doi.org/10.1016/j.optcom.2021.127604

78. Sun, X., Mu, X., Xu, C., Pang, H., Deng, Q., Zhang, K., Jiang, H., Du, J., Yin, S., and Du, C. "Dual-task convolutional neural network based on the combination of the U-Net and a diffraction propagation model for phase hologram design with suppressed speckle noise," *Optics Express* Vol. 30, No. 2, 2022, pp. 2646-2658.
doi: 10.1364/OE.440956

79. Wu, P., Zhang, D., Yuan, J., Zeng, S., Gong, H., Luo, Q., and Yang, X. "Large depth-of-field fluorescence microscopy based on deep learning supported by Fresnel incoherent correlation holography," *Optics Express* Vol. 30, No. 4, 2022, pp. 5177-5191.
doi: 10.1364/OE.451409

80. Dou, J., Dong, C., Dai, S., Mi, J., Luo, X., Di, J., Zhang, J., and Zhao, J. "High-resolution surface plasmon resonance holographic microscopy based on symmetrical excitation," *Optics and Lasers in Engineering* Vol. 153, 2022, p. 107000.
doi: https://doi.org/10.1016/j.optlaseng.2022.107000

81. Stoyanov, L., Zhang, Y., Dreischuh, A., and Paulus, G. G. "Long-range quasi-non-diffracting Gauss-Bessel beams in a few-cycle laser field," *Optics Express* Vol. 29, No. 7, 2021, pp. 10997-11008.
doi: 10.1364/OE.419486

82. Kim, H., and Lee, Y. H. "Unique measurement of the parameters of a twisted-nematic liquid-crystal display," *Applied Optics* Vol. 44, No. 9, 2005, pp. 1642-1649.
doi: 10.1364/AO.44.001642

83. Doskolovich, L. L., Soifer, V. A., Alessandretti, G., Perlo, P., and Repetto, P. "Analytical initial approximation for multiorder binary grating design," *Pure and Applied Optics: Journal of the European Optical Society Part A* Vol. 3, No. 6, 1994, p. 921.
doi: 10.1088/0963-9659/3/6/001

84. Morrison, R. L. "Symmetries that simplify the design of spot array phase gratings," *Journal of the Optical Society of America A* Vol. 9, No. 3, 1992, pp. 464-471.
doi: 10.1364/JOSAA.9.000464

85. Wyrowski, F., and Bryngdahl, O. "Iterative Fourier-transform algorithm applied to computer holography," *Journal of the Optical Society of America A* Vol. 5, No. 7, 1988, pp. 1058-1065.
doi: 10.1364/JOSAA.5.001058

86. Aghayee, S., Weikert, M., Alvarez, P., Frank, G. A., and Losert, W. "High Fidelity Spatial Light Modulator Configuration for Photo-Stimulation," *Frontiers in Physics* Vol. 9, 2021.
doi: 10.3389/fphy.2021.587112

87. Wagner, W., and Pruß, A. "The IAPWS Formulation 1995 for the Thermodynamic Properties of Ordinary Water Substance for General and Scientific Use," *Journal of Physical and Chemical Reference Data* Vol. 31, No. 2, 2002, pp. 387-535.
doi: 10.1063/1.1461829

88. "CGA Air Grade Specifications.Pdf." *Airsystems.Com*, Trace Analytics, www.airsystems.com/Reference/CGA Air Grade Specifications.pdf. Accessed 24 Apr. 2024.

89. Alexandrine, H., Marc-André, G., Karl-Alexandre, J., Pierre, T., Simon, S., Vincent, F., Philippe, L., Éric, G., Martin, C., and Fréderick, M. "Time-resolved multispectral imaging of combustion reaction," *Proc.SPIE*. Vol. 9485, 2015, p. 94851C.

90. Wang, P., Luo, X., and Li, Q. "Heat Transfer Study of the Hencken Burner Flame," *Flow, Turbulence and Combustion* Vol. 101, No. 3, 2018, pp. 795-819.
doi: 10.1007/s10494-018-9901-y

91. Ma, L., Lau, L. Y., and Ren, W. *TDLAS MEASUREMENT OF NON-UNIFORM TEMPERATURE AND SPECIES CONCENTRATION IN A LAMINAR FLAME*, 2016.

92. Lee, J., Bong, C., Yoo, J., and Bak, M. S. "Combined use of TDLAS and LIBS for reconstruction of temperature and concentration fields," *Optics Express* Vol. 28, No. 14, 2020, pp. 21121-21133.
doi: 10.1364/OE.396909

93. Lou, H. H., Chen, D., Martin, C. B., Li, X., Li, K., Vaid, H., Singh, K. D., and Gangadharan, P. "Optimal Reduction of the C1–C3 Combustion Mechanism for

the Simulation of Flaring," *Industrial & Engineering Chemistry Research* Vol. 51, No. 39, 2012, pp. 12697-12705.
doi: 10.1021/ie2027684

94. Ombrello, T., Carter, C., and Katta, V. "Burner platform for sub-atmospheric pressure flame studies," *Combustion and Flame* Vol. 159, No. 7, 2012, pp. 2363-2373.
doi: https://doi.org/10.1016/j.combustflame.2012.03.010

95. McAllister, S., Chen, J.-Y., and Fernandez-Pello, A. C. "Thermodynamics of Combustion," *Fundamentals of Combustion Processes*. Springer New York, New York, NY, 2011, pp. 15-47.

96. Erez, G., Collin, A., Parent, G., Boulet, P., Suzanne, M., and Thiry-Muller, A. "Measurements and models to characterise flame radiation from multi-scale kerosene fires," *Fire Safety Journal* Vol. 120, 2021, p. 103179.
doi: https://doi.org/10.1016/j.firesaf.2020.103179

97. Lozada-Cruz, G. "Some variants of Cauchy's mean value theorem," *International Journal of Mathematical Education in Science and Technology* Vol. 51, No. 7, 2020, pp. 1155-1163.
doi: 10.1080/0020739X.2019.1703150

98. Zehra, S., Birkök, H. G., Ahmet, E., and Ali, D. "Phase recovery from interference fringes by Hilbert transform," *Proc.SPIE*. Vol. 7443, 2009, p. 74431I.

99. Matsuki, A., Kori, H., and Kobayashi, R. "An extended Hilbert transform method for reconstructing the phase from an oscillatory signal," *Scientific Reports* Vol. 13, No. 1, 2023, p. 3535.
doi: 10.1038/s41598-023-30405-5

100. Onodera, R., Watanabe, H., and Ishii, Y. "Interferometric Phase-Measurement Using a One-Dimensional Discrete Hilbert Transform," *Optical Review* Vol. 12, No. 1, 2005, pp. 29-36.
doi: 10.1007/s10043-005-0029-7

101. Wang, S., Xue, L., Lai, J., and Li, Z. "An improved phase retrieval method based on Hilbert transform in interferometric microscopy," *Optik* Vol. 124, No. 14, 2013, pp. 1897-1901.
doi: https://doi.org/10.1016/j.ijleo.2012.05.029

102. Stoica, V., and Stephan, P. "PHASE SHIFT INTERFEROMETRY FOR ACCURATE TEMPERATURE MEASUREMENT AROUND A VAPOR BUBBLE," *Experimental Heat Transfer* Vol. 20, No. 3, 2007, pp. 261-275.

doi: 10.1080/08916150701229881

103. Jabeen, N., and Nirala, A. K. "Digital holographic interferometry for temperature measurement of oil lamp flames with different wick thicknesses," *Sustainable Energy Technologies and Assessments* Vol. 52, 2022, p. 101964.
doi: https://doi.org/10.1016/j.seta.2022.101964

104. Visser, B., Röhrbein, J., Steigmeier, P., Drinovec, L., Močnik, G., and Weingartner, E. "A single-beam photothermal interferometer for in situ measurements of aerosol light absorption," *Atmos. Meas. Tech.* Vol. 13, No. 12, 2020, pp. 7097-7111.
doi: 10.5194/amt-13-7097-2020

105. Rodriguez, L. G., Niemela, J., and Cabrera, H. "Measuring the linear optical absorption coefficient by interferometry and the thermal lensing effect: a numerical analysis," *Applied Optics* Vol. 62, No. 34, 2023, pp. 9002-9008.
doi: 10.1364/AO.500989

Appendix

Table A-1. Equipment Utilized for Imaging FLDI System

Type	Model	Quantity
Laser	Coherent Verdi G5	1
Diverging Lens	Thorlabs LC1439-A-ML	1
Linear Polarizer	Thorlabs LPVISE100-A	2
Diffractive Optical Element	HOLO/OR MS-215-Q-Y-A	1
Wollaston Prism	United Crystals (4 arcmin, 20 mm x 20 mm)	2
Focusing Lens	Thorlabs LJ1653L2	2
Plate Beam Splitter	Thorlabs BSW26R	1
Colored Glass Bandpass Filters	Thorlabs FGV9M	2
Camera	Photron FASTCAM Mini AX200	1
Neutral Density Filter	Thorlabs NE20A	1
Photodiode	Thorlabs PDA10A2	1
Oscilloscope	Rigol MSO5354	1
Impedance Adapter	ADP0150BNC	1

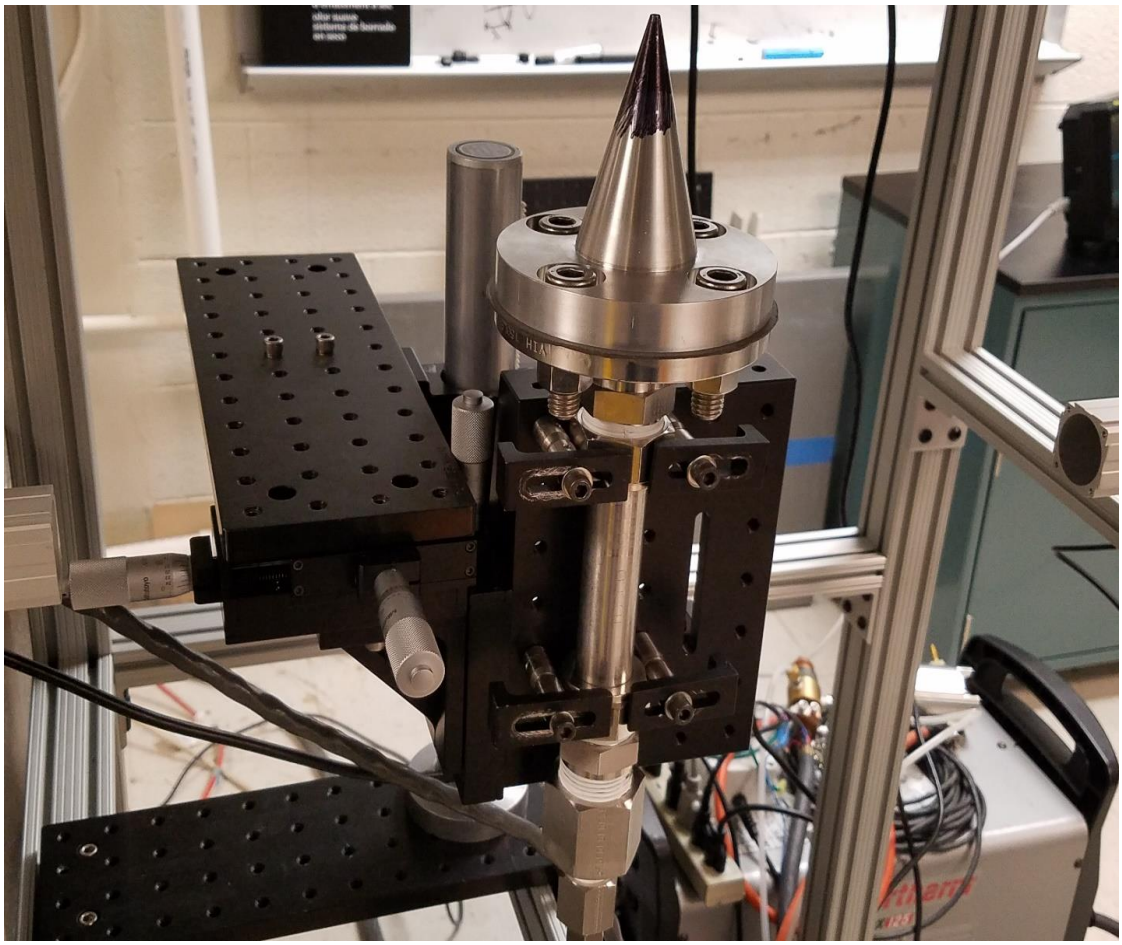

Figure A-1. Mach 1 jet nozzle assembly within test section.

Figure A-2. Mach 1 jet nozzle assembly within test section in horizontal orientation.

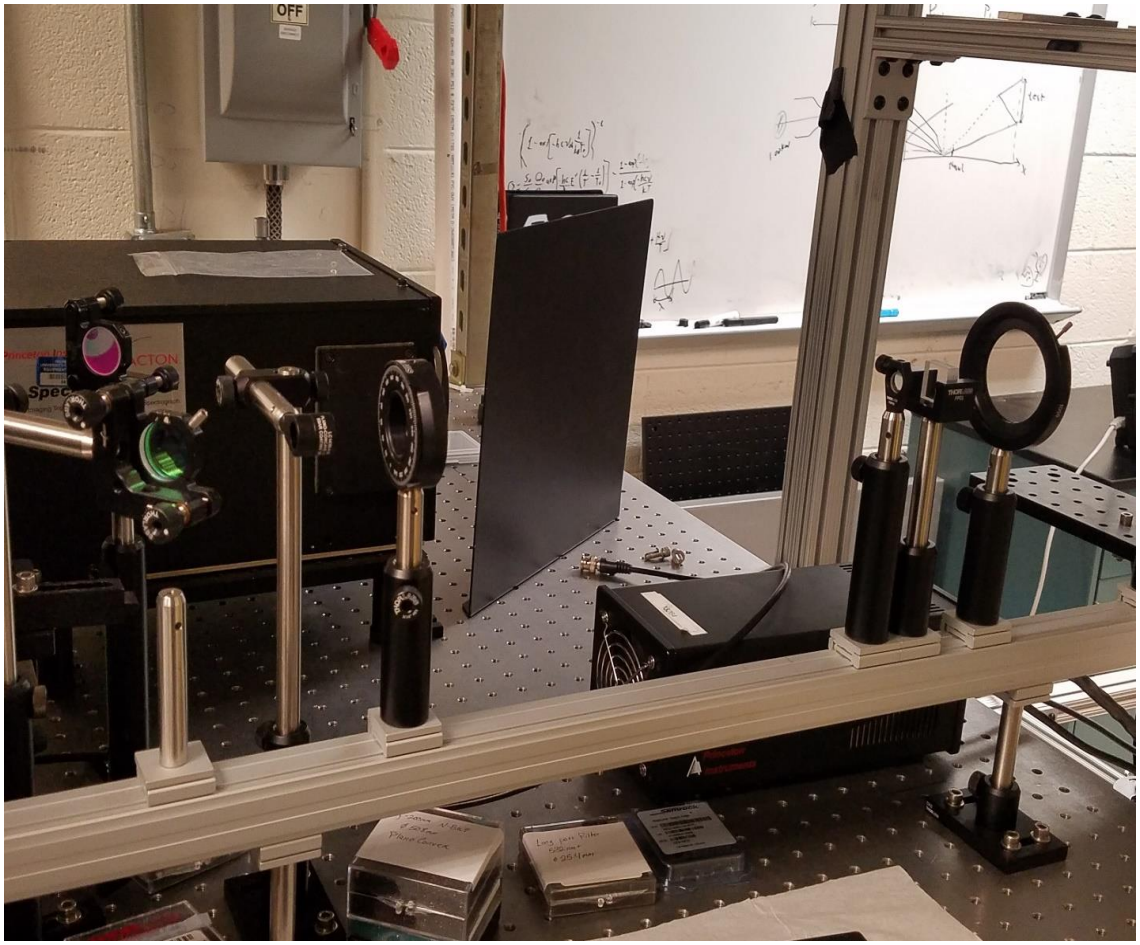

Figure A-3. Laser-side of FLDI system (excluding focusing lens).

To replicate this experiment, the positions of the optics will be outlined as determined by methodical application of the thin lens equation. The position of the diverging lens is designated as the origin of the system, with all optical positions given as some distance linearly removed from the origin point. For certain optics like the polarizers, specific positions were not noted, for these optics do not factor into the thin lens equation appreciably. The laser-side polarizer is located between the diverging lens and the diffractive optical element. The diffractive optical element is located at 340 mm, which is as close as possible to the laser-side Wollaston prism positioned at 370 mm. This is done in order to allow the laser beam to expand sufficiently to fill the optic before being diffracted and split in the beam splitter and prism. The laser-side focusing lens is then located at 570 mm. The nozzle exit is positioned to be centered in the middle of the test section of the FLDI system at 895 mm. The detector-side focusing lens is then located at 1220 mm, and the second Wollaston prism is located at 1420 mm. The detector-side polarizer is positioned between the Wollaston prism and the plate beam splitter. The plate beam splitter is located at 1580 mm, and the camera and photodiode are located at a right angle to each other, both 160 mm away from the plate beam splitter. The end of the system is depicted in **Fig. A-4**. The images for the 3x3 grid in the flow, as depicted by **Fig. A-5**, were recorded at a low sampling rate of 37.5 kHz because the sensor resolution would not have allowed for the full 3x3 grid at a higher sampling rate. However, the use of additional optics to reduce the size of the recombined beam array on the camera sensor may allow for significantly increased sampling rates in applicable experiments. As with previous arrays, **Fig. A-6** illustrates how the spectral content can be spatially determined with relative ease through the use of a camera.

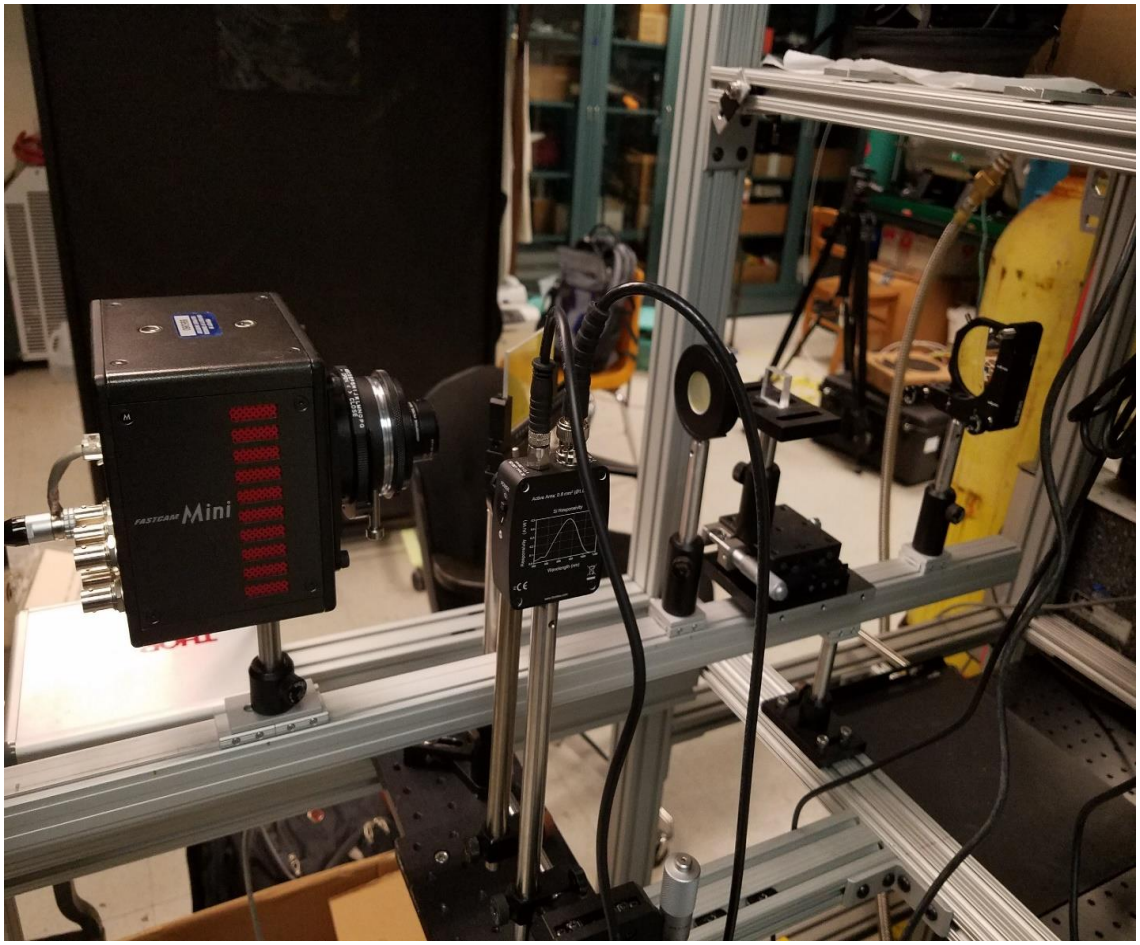

Figure A-4. Detector-side of FLDI system prior to full alignment.

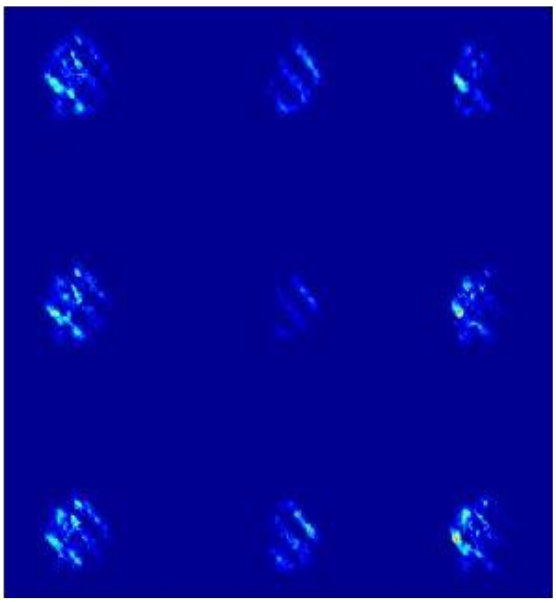

Figure A-5. 3x3 grid with nozzle perpendicular to FLDI beam pair separation direction.

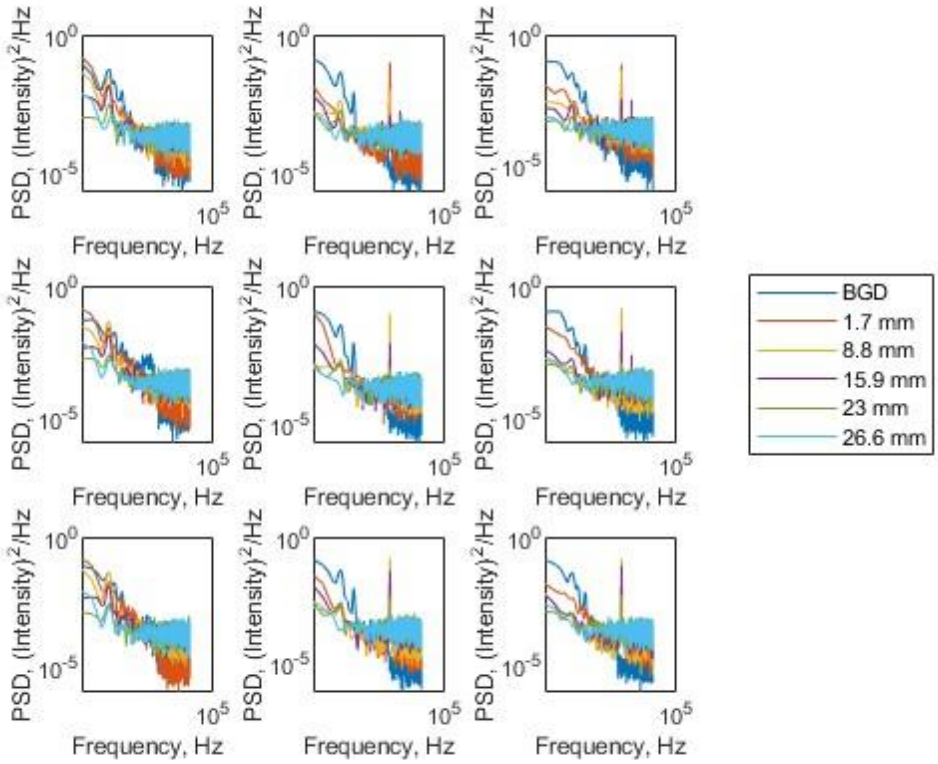

Figure A-6. Power spectral density as a function of frequency for 3x3 grid at various positions relative to nozzle exit.

For the sake of a complete overview, **Fig. A-7** portrays the full 5x5 array as seen during a background measurement, and it depicts how the intensity naturally varies among the array beam spots due to the apportionment of energy among different diffraction orders. By shifting the position of the nozzle, it was a simple matter to investigate the spectral content of the jet at 125 locations, as depicted in **Fig. A-8**. It is clear that the results of the 5x5 array are in keeping with the 3x3 array. That concludes the materials in the Appendix. See the last page for the Vita.

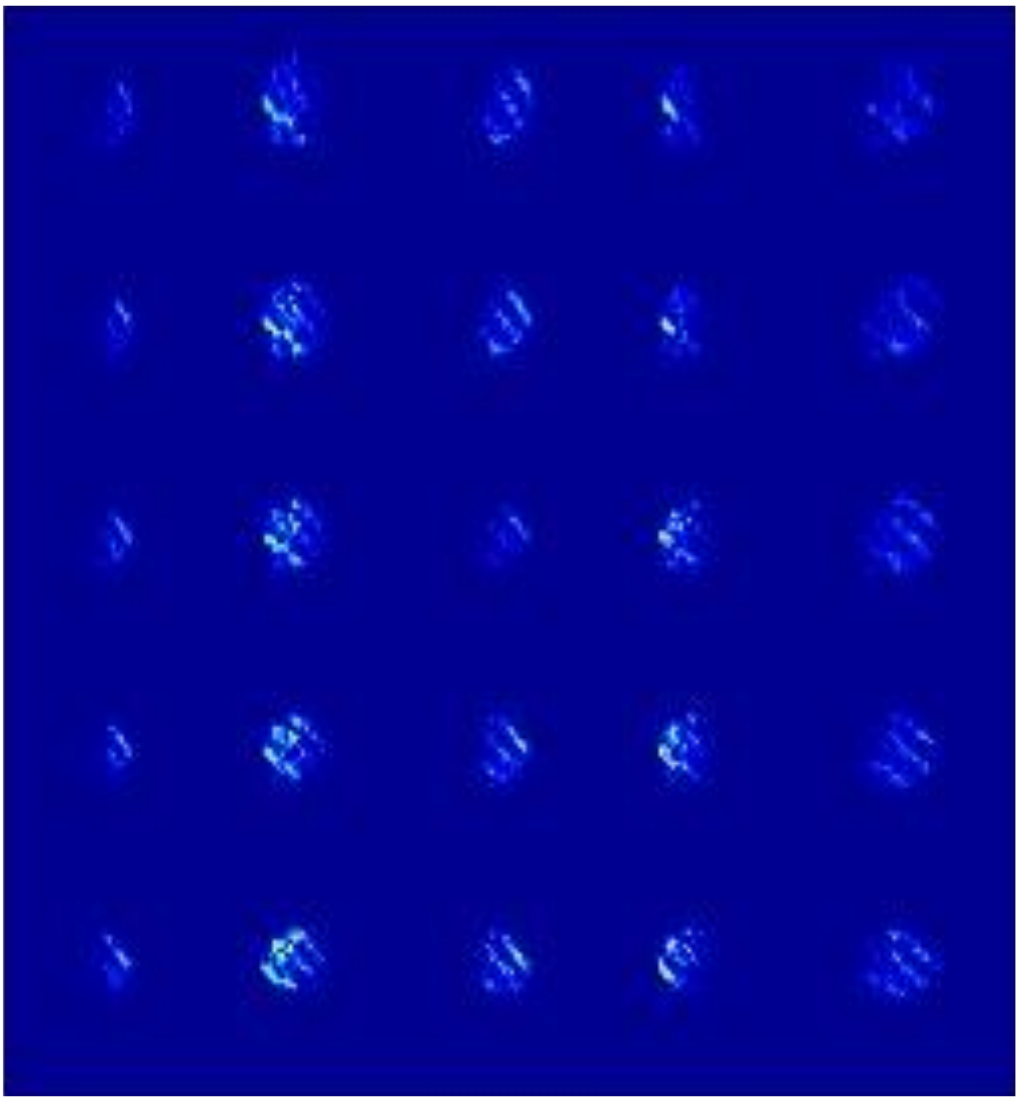

Figure A-7. 5x5 grid with nozzle perpendicular to FLDI beam pair separation direction.

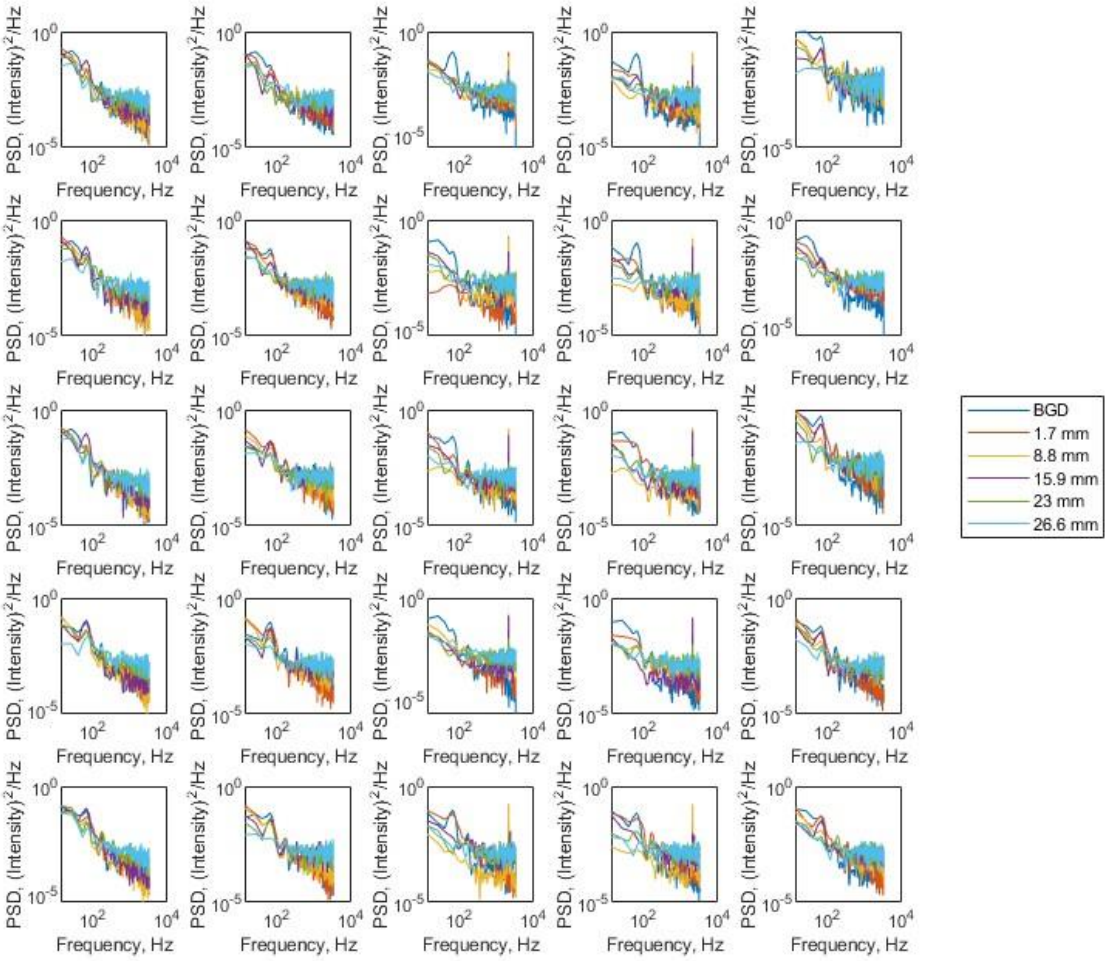

Figure A-8. Power spectral density as a function of frequency for 5x5 grid at various positions relative to nozzle exit.

Vita

Seth Richard Holladay was born in Knoxville, Tennessee. After graduating from Lenoir City High School, Seth attended University of Tennessee Knoxville where he joined the College of Engineering Honors and Chancellor's Honors programs and pursued his B.S. degree in aerospace engineering. Before completing his B.S. degree with honors in 2019, Seth enrolled in the 5-year B.S./M.S. program for aerospace engineering at the university. He researched ground source heat pump systems at Oak Ridge National Lab as a graduate research assistant during the pandemic. He completed his M.S. degree in late 2020 and enrolled in the Ph.D. program for aerospace engineering. During his time in the program, Seth was awarded the 2023 outstanding graduate student award in aerospace engineering, a John D. Tickle Fellowship in the Department of Mechanical, Aerospace & Biomedical Engineering, and a University of Tennessee Knoxville Graduate School summer fellowship.